DEVELOPMENT OF A HIGHLY BALANCED GRADIOMETER FOR FETAL MAGNETOCARDIOGRAPHY

Siarhei Uzunbajakau

Samenstelling promotiecommissie:

Prof. dr. W.H.M. Zijm	Universiteit Twente, voorzitter
Prof. dr. ir. M. Wessling	Universiteit Twente, secretaris
Prof. dr. ir. H.J.M. ter Brake	Universiteit Twente
Prof. dr. H. Rogalla	Universiteit Twente
Prof. dr. ir. C.H. Slump	Universiteit Twente
Prof. dr. ir. P.H. Veltink	Universiteit Twente
Dr. ir. B. ten Haken	Universiteit Twente
Dr. ir. A.P. Rijpma	ASML
Prof. dr. P. Seidel	Friedrich Schiller University

Acknowledgement
This research was supported by:

- Dutch Technology Foundation (STW)
- Institute for Biomedical Technology (BMTI)
- Philips Medical Systems
- Twente Medical Systems
- Thales Cryogenics

S. Uzunbajakau,
Development of a highly balanced gradiometer for fetal magnetocardiography
Proefschrift Universiteit Twente, Enschede
ISBN 978-90-365-2670-8

Printed by Uitgeverij BOX Press, Oisterwijk, The Netherlands

DEVELOPMENT OF A HIGHLY BALANCED GRADIOMETER FOR FETAL MAGNETOCARDIOGRAPHY

PROEFSCHRIFT

ter verkrijging van
de graad van doctor aan de Universiteit Twente,
op gezag van de rector magnificus,
prof.dr. W.H.M. Zijm,
volgens besluit van het College voor Promoties
in het openbaar te verdedigen
op 06 juni 2008 om 15:00 uur

door

Siarhei Uzunbajakau
geboren op 27 juli 1974
te Minsk

Dit proefschrift is goedgekeurd door de promotoren:

Prof. dr. ir. H.J.M. ter Brake
Prof. dr. H. Rogalla

Success is the ability to go from one failure to another with no loss of enthusiasm.
Sir Winston Churchill.

Contents

Chapter 1

Introduction

1.1 Fetal magnetocardiograph as a diagnostic tool

1.1.1 The origin of cardiograms

Activation of the cardiac muscle is associated with the transport of sodium (Na^+), potassium (K^+), and calcium (Ca^{++}) ions through the membrane of the cardiac cell. This ion transport gives rise to the strongest electrophysiological signals in the human body: the cardiograms (Malmivuo and Plonsey, 1995; Marieb and Hoehn, 2007).

When a cardiac cell is at rest, the intracellular and extracellular concentrations of the ions establish a potential difference of -90mV across the cell membrane (figure 1.1c). Biasing the potential difference towards more positive values increases the permeability of the membrane to sodium ions (figure 1.1d). Following the concentration gradients, the sodium ions diffuse into the intracellular space. The fast sodium influx dominates the decreasing potassium efflux. The net flux swiftly changes the potential difference across the membrane from -90mV to +30mV. This process is called depolarization. After the fast sodium channels responsible for the depolarization are closed, the permeability of the membrane to calcium ions increases allowing the calcium ions to diffuse into the cell balancing the potassium efflux. During this period, the potential difference decreases slowly forming the plateau phase. Decrease of the sodium influx and increase of the potassium efflux follows a plateau phase restoring the potential difference across the membrane to -90mV. This restoration activity is known as repolarization.

The pacemaker cells that are located in the SA-node of the heart exhibit autonomous depolarization (figure 1.1a). These cells being depolarized stimulate the cells located in the immediate proximity causing them to depolarize as well. These newly depolarized cells activate their neighboring cells and so forth. In effect, the depolarization spreads over the cardiac muscle forming a front consisting of depolarizing cells, a so called depolarization front. The transmembrane voltage behind the depolarization front is positive while the transmembrane voltage ahead of the depolarization front is negative. Thus, a double layer source is formed which can be also treated as a layer of current dipoles oriented parallel to the direction of propagation

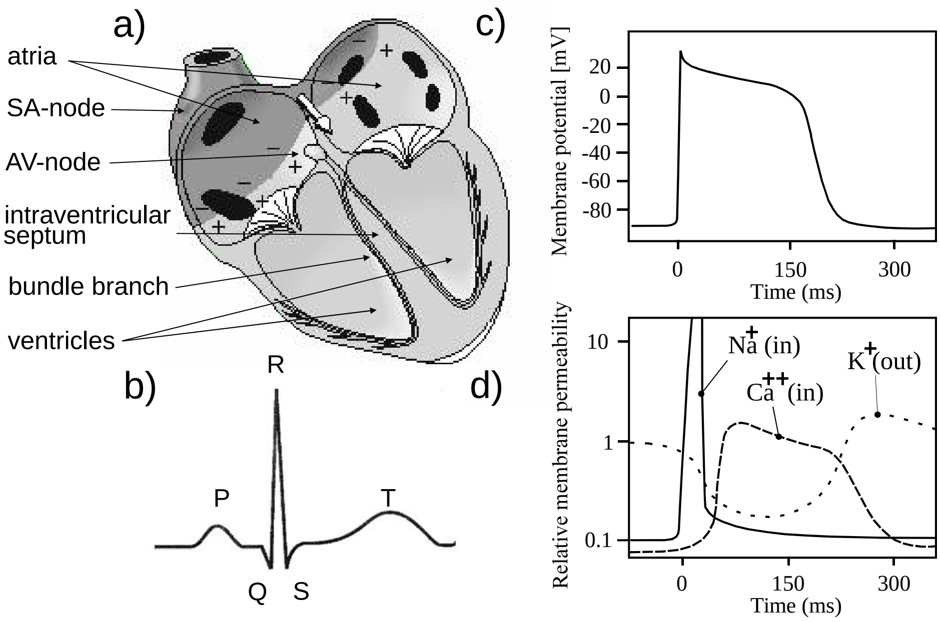

Figure 1.1. a) Cross section of the heart. Adapted from (Malmivuo and Plonsey, 1995). Pluses and minuses represent depolarization front. The arrow between the atria represents the equivalent current dipole of the depolarization front. b) A stylized plot of a segment of a cardiogram that corresponds to one heart beat. c) Cardiac action potential d) Relative membrane permeability.

of the depolarization front, or even by a single equivalent current dipole with a changing magnitude and direction (Malmivuo and Plonsey, 1995). This equivalent current dipole produces changes in the electric and magnetic fields that can be recorded. The records of the changes in the electric potential difference and in the magnetic field are called electrocardiograms (ECGs) and magnetocardiograms (MCGs), respectively. An example of such a record is shown in figure 1.1b.

Activation of a healthy heart is initiated by the depolarization of the pacemaker cells located in the SA-node. First, the depolarization front spreads over the atrial walls causing the atrial chambers to contract. The propagation of the depolarization front over the atria manifests itself by the P-wave in the cardiogram (see figure 1.1b). A time delay follows the arrival of the depolarization front at the AV-node allowing the blood to fill the ventricles. From the AV-node, depolarization advances to the interventricular septum via the bundle branches. The depolarization of the ventricles starts from the interventricular septum. The depolarization and repolarization of the ventricles correspond to the QRS-complex and T-wave, respectively. The wave that corresponds to the repolarization of the atrium overlaps with the QRS-complex. Repolarization of cardiac cells is less synchronized in time and space than depolarization. As a consequence, the T-wave in the cardiogram lasts longer and has a lower magnitude when compared to the QRS-complex.

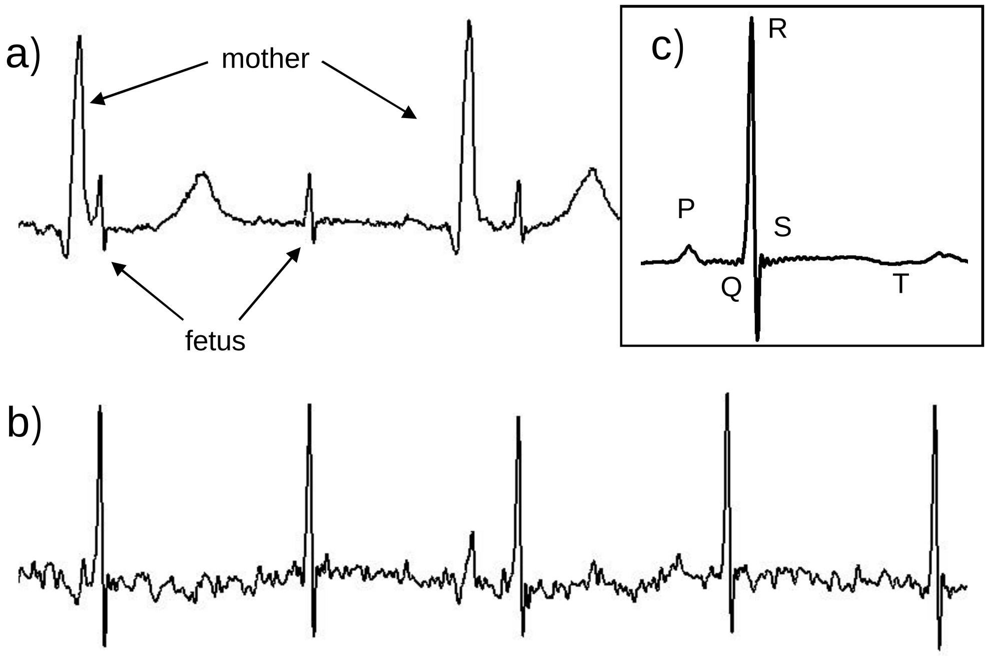

Figure 1.2. a) Example of a raw fMCG as recorded above maternal abdomen. b) The same fMCG with the maternal MCG removed. c) Averaged fMCG.

The same processes occur in the fetal heart, though several differences exist between the fetal and adult cardiograms. The fetal heart beats with a rate of approximately 150*bpm* which is twice as high as the beat rate of the adult human heart. As the fetal heart is growing during gestation, the heart rate decreases and the duration of the intracardiac intervals positively correlates with the age of gestation. The difference most relevant to the measurements of fetal magnetocardiograms is that the fetal heart produces relatively weak signals. For instance, a MCG of an adult can have a peak-to-peak magnitude as high as 100*pT* whereas for fetuses it hardly exceeds 10*pT*. The reason for such a small magnitude of the fMCGs is twofold. Firstly, the volume of the fetal heart is smaller than that of the adult. Secondly, the source current dipole which represents the depolarization front gives rise to volume currents in the surrounding conducting tissues. The magnetic fields induced by the volume currents oppose the magnetic fields induced by the primary source decreasing the magnitude of the recorded signal. In adults, the volume currents are spread all over the chest providing that the distance between the sensor and the primary source is smaller than the dimensions of the volume conductor. In the maternal abdomen, however, the currents induced by the fetal heart are mostly restricted to the fetus (Stinstra, 2001). For this reason, the distance between the sensor and the primary source is comparable or even larger than the dimensions of the volume conductor (i.e. fetus). Consequently, the volume currents in fetus compensate the magnetic field of the primary source more effectively.

1.1.2 Fetal magnetocardiography

In fetal magnetocardiography, the magnetic field produced by the fetal heart is recorded in the vicinity of the maternal abdomen. An example of such a record is shown in figure 1.2a. The record consists of the MCGs of the fetus and that of the mother. The maternal signal is removed from the record by employing signal processing techniques based on averaging of the maternal MCG (see (Stinstra, 2001) for example). Usually, the maternal ECG is recorded simultaneously with the fMCG to provide a robust trigger for the averaging of the maternal MCG. An example of a fMCG with the maternal MCG removed is shown in figure 1.2b. Customary, the fetal heart signal is averaged in order to increase the signal-to noise ratio (see figure 1.2c). The diagnosis is made by analyzing both the raw and the averaged signals.

The fetal magnetocardiography can be used for assessment of intracardiac intervals (van Leeuwen *et al.*, 2004), classification of arrhythmia (Stinstra, 2001; Menendez *et al.*, 2001; Kandori *et al.*, 2003), and diagnosis of long-QT syndrome (Hosono *et al.*, 2002). There are two main competitive techniques that are routinely used for the assessment of the fetal heart: fetal electrocardiography and fetal echocardiography (i.e. ultrasound).

The fECGs are measured via electrodes attached to the maternal abdomen. The signal-to-noise ratio of the fECGs is generally poor and hardly exceeds ten (Oostendorp and van Oosterom, 1991). Moreover, it is difficult to detect the P- and T- waves in fECGs even after averaging (Bergveld *et al.*, 1986; Brambati and Pardi, 1980). In (Peters *et al.*, 1998) it is discussed that the absences of the T-wave in the fECGs is probably due to capacitive effects in the volume conductor and that the influence of this capacitive effect is much smaller in the fMCGs.

The echocardiography monitors the mechanical contraction of the fetal heart and does not provide information on the electrophysiological processes within the heart. However, the details of the electrophysiological processes are important for an accurate classification of arrhythmia (Stinstra, 2001). This importance is further illustrated by a study case described in (Peters *et al.*, 2005). In this study case the diagnosis of atrial flatter was made by means of ultrasound. The fMCG record of the same patient is shown in figure 1.3b. A fMCG record typical for the atrial flutter is shown in figure 1.3a. The fMCG record that corresponds to the atrial flutter (figure 1.3a) shows the specific saw-tooth pattern, whereas it is absent in the fMCG shown in figure 1.3b. This observation led to a diagnosis of persistent junctional reciprocating tachycardia (PJRT). On the other hand, it is difficult to discriminate between the atrial flutter and PJRT by employing ultrasound (Peters *et al.*, 2005).

Usefulness of fetal magnetocardiography can be summarized, by stating its two main advantages that distinguish it from the competitive techniques:

- Unlike ultrasound, fMCG provides information on the electrophysiological processes in the fetal heart which is invaluable for an accurate diagnosis.

- Unlike fECG, the fMCG can provides information on P- and T- waves. The signal-to-noise ratio of fMCGs is typically better than that of the fECGs.

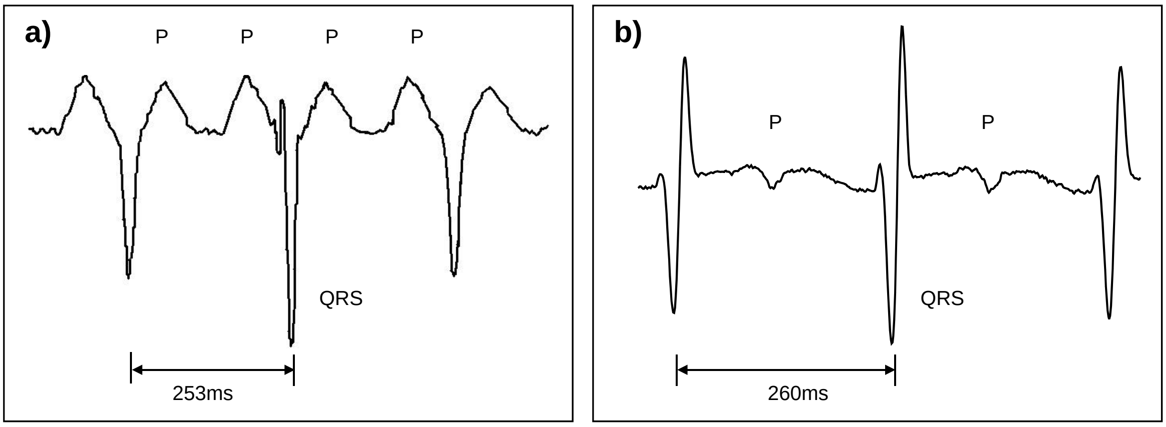

Figure 1.3. Examples of fMCGs that correspond to two different kinds of arrhythmia: a) atrial flutter, b) persistent junctional reciprocating tachycardia (PJRT).

1.2 Instrumentation for fetal magnetocardiography

1.2.1 Fetal magnetocardiograph: examples

The peak amplitude of the fMCGs approximately equals $1pT$ on average. The spectral content of the signal is typically between 1 and $100Hz$. For a successful recording of fMCGs a resolution better than $10fT/\sqrt{Hz}$ is required (ter Brake *et al.*, 2002). Magnetometers based on *S*uperconducting *QU*antum *I*nterference *D*evices (SQUIDs) are used in fetal magnetocardiography due to their extreme sensitivity to magnetic flux. To reach the superconducting state, the SQUIDs are cooled to cryogenic temperatures.

In figure 1.4a a 151-channel SQUID *A*rray for *R*eproductive *A*ssessment (SARA) designed for recording fMCGs and fetal magnetoencephalograms (fMEGs) is shown (Robinson *et al.*, 2001). The relatively large amount of measuring channels allows full coverage of the maternal abdomen. The system provides a sensitivity of $4fT/\sqrt{Hz}$. The SQUID-based gradiometers are located inside a horizontally operated dewar filled with liquid helium (4K). The dewar needs to be refilled with liquid helium once a week. The refilling requires regular supply of liquid helium and a skilled technician. Cryocoolers are used in the instrumentation for fetal magnetocardiography as an alternative to the dewars with liquid coolant. An example of a cryocooler-cooled high-Tc fetal magnetocardiograph operating below $80K$ is shown in figure 1.4b (Rijpma, 2002). This system is equipped with a single measuring channel which needs to be repositioned above the maternal abdomen in search of the location where a fMCG with a sufficient signal-to-noise ratio can be recorded.

Most research activities in the design of a fetal magnetocardiograph are related to the following three topics: SQUID design, instrumentation for cooling, and instrumentation for environmental magnetic interference suppression.

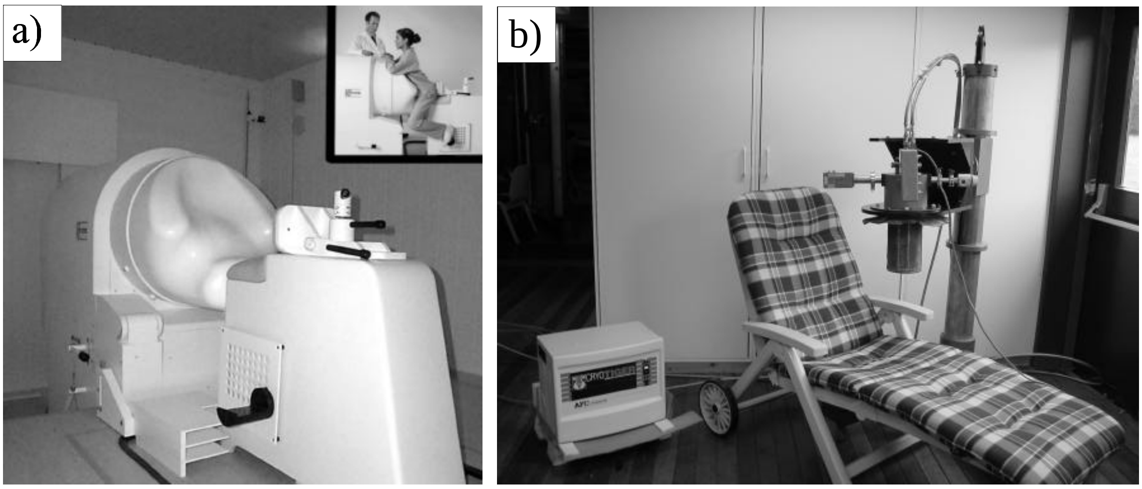

Figure 1.4. a) SQUID *A*rray for *R*eproductive *A*ssessment (SARA) by CTF systems inc. This is an 151-channel system designed for recording fMCGs and fMEGs. It is cooled by a liquid helium bath. b) A single channel cryocooler-cooled high-Tc fetal magnetocardiograph. Both figures adapted from (Rijpma et al., 2002).

1.2.2 SQUID magnetometers

Up to date, several types of SQUID magnetometers suitable for application in Biomagnitism were developed. A few examples are: dc-SQUIDs (Cantor, 1996), rf-SQUIDs (Zeng *et al.*, 1998), DROSs (Adelerhof *et al.*, 1994), and double-stage SQUIDs (Podt *et al.*, 1999). However, the low-Tc dc-SQUIDs are the only commercially available SQUIDs that can provide a sensitivity adequate for fetal magnetocardiography.

The dc-SQUID consists of a loop of superconducting material (Nb) interrupted by two Josephson junctions (see figure 1.5a). The relation between the current flowing through a Josephson junction and the voltage established across the junction is schematically depicted in figure 1.5b. The Josephson junction is resistless if the current flowing through it does not exceed the critical current. If the critical current is exceeded, a voltage is built up across the junction. Apart from the biasing current, the voltage across the junction depends on the magnetic flux enclosed by the superconducting loop of the SQUID. The flux-voltage dependence of the junction for a fixed biasing current is shown in figure 1.5c. The dc-SQUID can be regarded as a magnetic-flux-to-voltage transducer with a Φ_0-periodic transfer. The superconducting loop of the SQUID has relatively small area. In order to improve the sensitivity of the dc-SQUID to the magnetic field an external sensing coil made of the superconducting material is inductively coupled to the SQUID via an input coil that is deposited on top of the superconducting loop of the SQUID.

Typically, the dc-SQUID is operated in a flux locked loop (FLL) in order to linearize the transfer (figure 1.5d). The output voltage of the dc-SQUID is amplified, filtered, converted into magnetic flux by means of the feedback coil, and fed into the

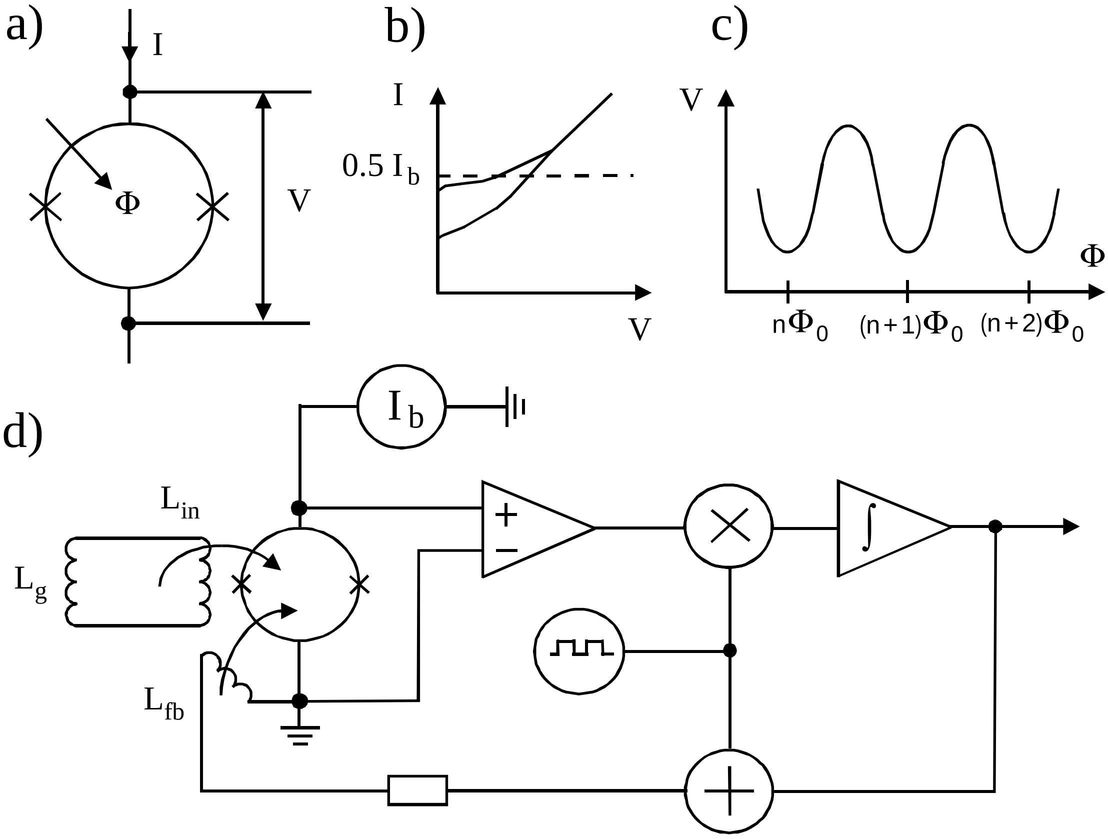

Figure 1.5. a) dc-SQUID. b) Voltage-current characteristic of a Josephson junction. c) Dependence of the voltage across a Josephson junction on the flux enclosed by the superconducting loop of the SQUID. d) Scheme of the flux-locked-loop.

superconducting loop of the SQUID. As a consequence, the changes of the net magnetic flux in the SQUID are close to zero and are restricted to a small segment of the flux-to-voltage transfer which is relatively linear. In order to avoid low-frequency 1/f noise of the first-stage amplifier the flux in the SQUID is modulated.

The output voltage noise on the FLL expressed as an equivalent magnetic flux enclosed by the superconducting loop of the SQUID reads

$$S_{\Phi}^{1/2} = \sqrt{S_{\Phi,SQUID} + \frac{1}{V_{\Phi}^{2}} S_{V,AMPL}} \tag{1.1}$$

where V_{Φ} is the flux-to-voltage transfer of the SQUID in the working point; $S_{\Phi,SQUID}$ and $S_{V,AMPL}$ are the flux noise of the SQUID and the input voltage noise of the first-stage amplifier, respectively. The input voltage noise of the state-of-the-art room-temperature amplifier approximately equals $S_{V,AMPL}^{1/2} = 1nV/\sqrt{Hz}$ (AD797 from Analog Devices, for instance). The V_{Φ} value of a dc-SQUID typically equals $100\mu V/\Phi_0$.

Thus, the contribution of the first-stage amplifier to the total system noise approximately equals $10\mu\Phi_0/\sqrt{Hz}$. This value is in the range of the flux noise of the SQUID. For this reason, a significant decrease in the flux-to-voltage transfer V_Φ increases the system noise. High-frequency magnetic fields that are coupled to the SQUID via the sensing coils or via the leads that connect the SQUID to the FLL effectively decrease the flux-to-voltage transfer. A model of this effect confirmed experimentally can be found in (Rijpma, 2002). To prevent coupling of the high-frequency interference to the SQUID, the whole setup (i.e. the sensing coil, the SQUID, and the FLL) is enclosed by a radio-frequency shield.

1.2.3 Environmental interference suppression

Environmental magnetic field

As the magnitude of the fMCGs is weak ($\sim 1pT$), almost any source of magnetic field active in the bandwidth of $1 - 100Hz$ interferes with sensitive fMCG measurements. A summary of Power Spectral Densities (PSDs) of the environmental magnetic fields and first order gradients recorded inside and outside magnetically shielded rooms in various locations is shown in figure 1.6 (Vrba and Mckay, 1998). The dashed areas in the figure represent the ranges of the records. The slope of the PSD is most likely due to magnetic objects moving in the vicinity of the measurement site. The moving magnetic objects contribute to the environmental noise indirectly by modulating the magnetic field of the earth. For instance, (Vrba, 1996) simulated car traffic. The simulations show a good fit into measured environmental magnetic field in both time and frequency domains. In (Vrba, 1996) it is concluded that the slope in the PSD can be described as $1/f^k$ with k varying between 1 and 4 depending on traffic condition. The peak at the frequency of $50Hz$ in figure 1.6 represents magnetic field induced by the power lines and by the power suppliers of the laboratory equipment. The bump between $10Hz$ and $50Hz$ represents vibration of the sensing coil in the magnetic field of the earth. For comparison, a PSD of a fMCG with a peak-to-peak magnitude of $1pT$ is shown in figure 1.6b as well. From this comparison, it follows that the environmental magnetic interference needs to be suppressed for a successful fMCG recordings. For instance, in order to achieve a resolution of $10fT/\sqrt{Hz}$ (ter Brake *et al.*, 2002) the magnetic field may need to be suppressed by a factor of 10^6 at a frequency of $1Hz$. This suppression factor equals the ratio of the upper bound of the expected uniform magnetic field in unshielded environments at $1Hz$ ($10nT/\sqrt{Hz}$) and $10fT/\sqrt{Hz}$.

Magnetic Shielding

The most straightforward method of environmental magnetic interference suppression is shielding. For many years, magnetically shielded rooms were used to isolate sensitive instrumentation for Biomagnetism from the magnetically hostile environment. An example of a magnetically shielded room is shown in figure 1.7a. Walls of the magnetically shielded room consist of a layer of aluminum and a few layers of $\mu-$metal

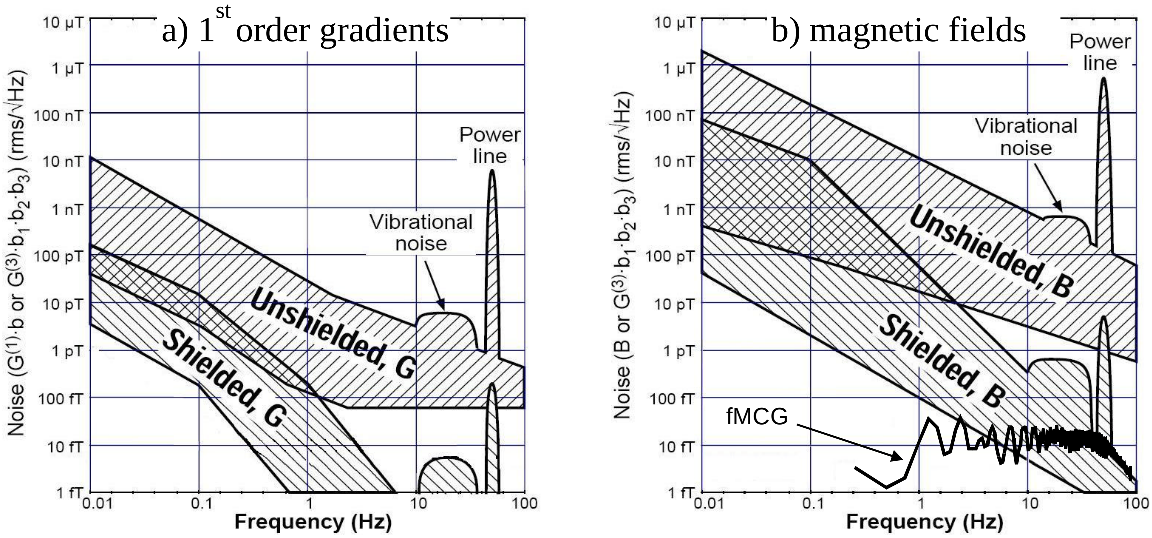

Figure 1.6. Summary of environmental noise observed in shielded and unshielded environments. a) First-order gradients of the environmental magnetic noise measured by a balanced first order gradiometer with a baseline of $0.05m$. b) Magnetic field noise and Power Spectral Density of a fMCG of $1pT$ peak-to-peak.

(Bork *et al.*, 2000; Cohen *et al.*, 2002). The aluminum and $\mu-$metal layers provide different kinds of shieling. External magnetic fields induce eddy currents in the aluminum layer. The magnetic field produced by eddy currents opposes the external magnetic field decreasing its magnitude. According to the Faraday law the magnitude of the eddy currents and thus the effectiveness of the shielding is proportional to the frequency of the applied magnetic field. For this reason, the eddy-current shielding has almost no effect at lower frequencies. This lack of shielding at lower frequencies is compensated by the layers of $\mu-$metal. $\mu-$metal is a soft ferromagnetic material which does not retain significant magnetization after the external magnetic field is removed. A sheet of $\mu-$metal can be regarded as a collection of microscopic magnetic dipoles that tend to align themselves parallel to the applied magnetic field. Outside the sheet, the net magnetic field of these dipoles opposes the applied magnetic field decreasing its magnitude. The shielding effectiveness of the $\mu-$metal is constant at the lower frequencies. In a typical shielded room, the $\mu-$metal shielding is effective at frequencies below $0.1Hz$ whereas the eddy current shielding is effective above $0.1Hz$. Magnetically shielded rooms made of aluminum and μ-metal are capable of establishing a shielding factor of $2.4 \cdot 10^5$ at the frequencies above $1Hz$ (Cohen *et al.*, 2002). Two shielded rooms located one inside the other can provide a shielding factor of 10^6 at $1Hz$ (Bork *et al.*, 2000). This is the highest shielding factor at room temperatures achieved at the moment (see figure 1.7b).

Magnetically shielded rooms are often equipped with a set of magnetic field coils for active compensation of the residual magnetic fields inside the room at lower frequencies (ter Brake *et al.*, 1991a; Bork *et al.*, 2000). That is, the magnetic field is

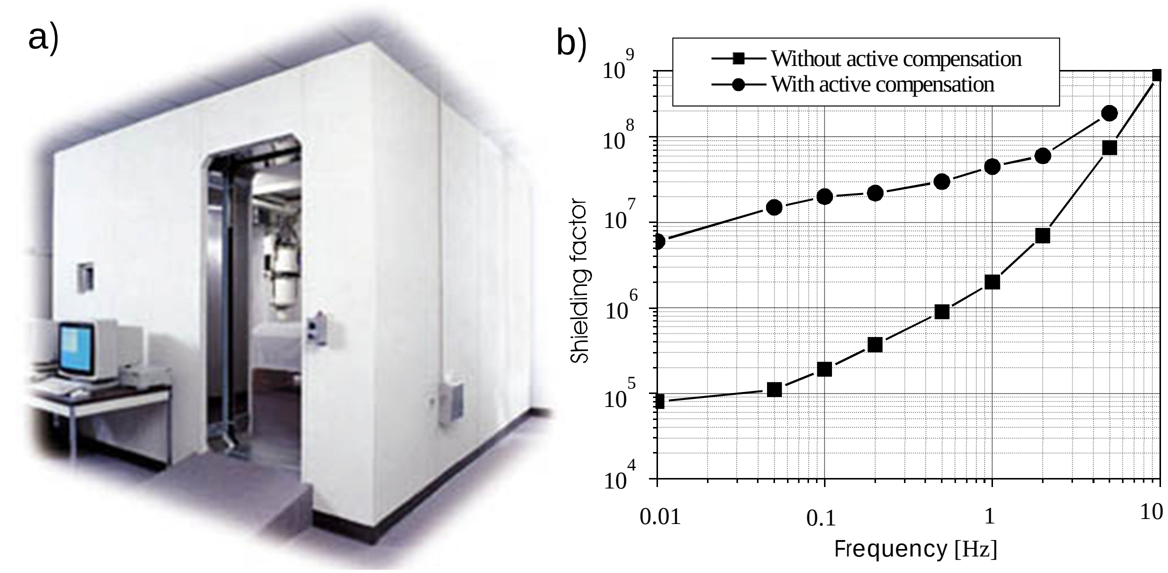

Figure 1.7. a) Example of a magnetically shielded room. Adapted from www.eretec.com. b) Shielding factors of the magnetically shielded room installed in Berlin. These are the highest shielding factors at room temperatures achieved at the moment. Adapted from (Bork et al., 2000)

monitored inside a magnetically shielded room by a magnetic field sensor. The signal of the sensor is fed into the coils such that the total magnetic field in the magnetically shielded room is reduced. To use this compensation scheme effectively, the reference sensor inside the shielded room should be as sensitive as the sensor used in the actual Biomagnetic measurements (ter Brake *et al.*, 1993). An additional shielding factor of $40dB$ at $1Hz$ due to the application of active shielding was reported (ter Brake *et al.*, 1993).

A more high-tech approach to the construction of a magnetically shielded room is described in (Kato *et al.*, 2002). In (Kato *et al.*, 2002) active shielding panels are used instead of traditional combination of aluminum and $\mu-$metal layers. Each active panel consists of a square coil with a magnetic field sensor located in the center of the coil. The signal of the sensor is fed into the coil such that the normal component of the magnetic field in the center of the panel is canceled. The boundary of the volume to be shielded is paved with the active panels. One may expect that the magnetic field inside the volume equals zero as the normal component of the magnetic field at the boundary is nullified by the active panels. A magnetically shielded room constructed from the active panels has obvious advantages in manufacturing, transportation, and installation. However, only a shielding factor of 17 has been realized at the moment (Kato *et al.*, 2004).

Gradiometry

Although magnetically shielded rooms offer a shielding factor sufficient for Biomagnetic applications there is an obvious disadvantage: a hight cost of manufacturing and installation. Furthermore, due to its relatively large weight a shielded room is typically installed at the ground level of a building. Ones a shielded room is installed, the fMCG measurements need to be carried out inside it. In other words, the shielded room leads to inflexibility in the choice of the location of the fMCG measurements site. For these reasons, there is a constant search for alternative techniques for environmental interference suppression. Gradiometry is often considered as an alternative to shielding.

In figure 1.8a, a so-called first-order axial gradiometer is shown. The gradiometer is wound from superconducting (niobium) wire . The ends of the wire are connected to the input coil of the SQUID such that the gradiometer and the input coil of the SQUID form a closed superconducting loop (see L_g and L_{in} in figure 1.5d). The magnetic field produced by a nearby source (i.e. fetal heart) has a relatively large gradient in the vicinity of the gradiometer. Thus, the resulting magnetic fluxes through the two turns of the gradiometer have different magnitudes. Environmental noise sources that are located relatively far away from the gradiometer produce a magnetic field that is relatively homogeneous in the vicinity of the gradiometer. Consequently, the magnetic noise fluxes that penetrate the two turns are almost equal in magnitude. Since the turns are wound in opposite directions, the current induced in the coils by the noise source is canceled whereas the current induced by the source of useful signal (i.e. fetal heart) retains a significant magnitude. The subtraction of the output signals of two first-order gradiometers produces a second-order gradiometer. An example of such a second-order axial gradiometer is shown in (figure 1.8b). In turn, the subtraction of the output signals of two second-order gradiometers results in the formation of the signal of a third-order gradiometer figure 1.8c. In general, the higher the order of the gradiometer the stronger the effect of environmental interference suppression. However, in practice gradiometers up to third order are used. The first three gradiometers in figure 1.8 are referred to as hardware gradiometers as the subtraction of the signals of the corresponding lower order gradiometer is implemented in the hardware of the gradiometers. As an alternative, the signals of the lower order gradiometers can be readout separately and subtracted electronically or in the software. In this case, the gradiometer is referred to as a synthetic gradiometer. An example of a synthetic gradiometer is shown in figure 1.8d. All gradiometers shown in figure 1.8 are sensitive to the longitudinal gradients of the magnetic fields as all individual coils of the gradiometers are coaxial. Alternatively, a group of coplanar coils can be arranged to create sensitivity to the transversal gradients of the magnetic field (so-called planar gradiometers). A more detailed description of higher-order gradiometer formation can be found in (Vrba, 1997; Vrba and Robinson, 2002).

Ideally, a gradiometer of order n is insensitive to magnetic field gradients of an order less than n. However, in practice it is difficult to manufacture a gradiometer

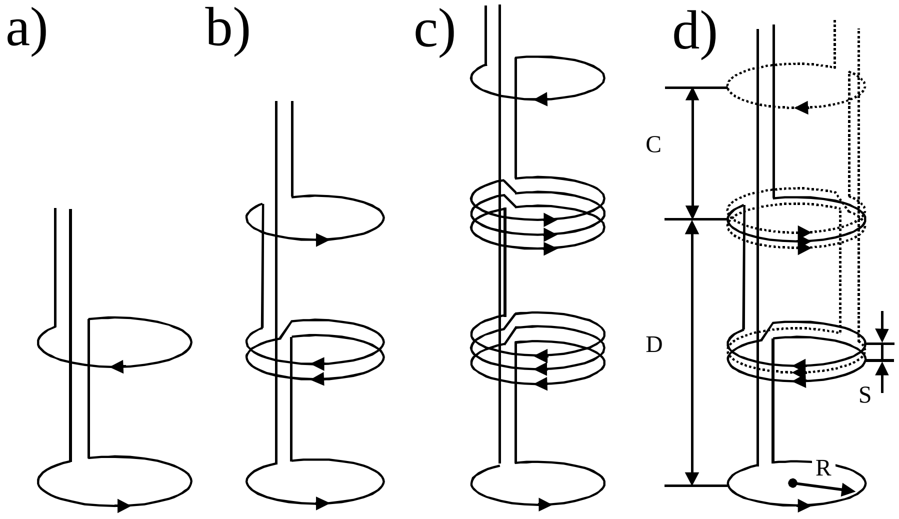

Figure 1.8. Examples of gradiometer formation. a) First-order axial gradiometer made of two turns of superconducting wire wound in opposite directions. b) Second-order gradiometer made of two first-order gradiometers displaced relative to each other. The turns of the gradiometer are wound such that the signals of the two first-order gradiometers are subtracted. c) Third-order gradiometer made of two second-order gradiometers. d) Third-order gradiometer composed of two second-order gradiometers, where the signals of the two second-order gradiometers are read out separately and subtracted from each other in software.

such that its sensitivity to lower order gradients is eliminated completely. Manufacturing tolerances lead to errors such as differences between the radii of the individual turns or errors in their orientations and positions. These errors create a sensitivity of the gradiometer to lower order gradients. Apart from that, conducting and superconducting parts of the measuring setup (such as radio-frequency interference shields and SQUID modules, respectively) disturb the applied magnetic field, thus creating a sensitivity of the measuring setup to lower order gradients. This residual sensitivity of a gradiometer to lower order gradients is referred to as imbalance (ter Brake *et al.*, 1989). Imbalance reduces the ability of a gradiometer to suppress environmental interference. Typically, imbalance is compensated mechanically (Hesterman, 1976b; Hesterman, 1976a; Rorden, 1976; Overweg and Walter-Peters, 1978), electronically (ter Brake *et al.*, 1989), or using a combination of the two approaches (Vrba and McCubbin, 1983).

In mechanical balancing, a system of superconducting tabs is located in the proximity of gradiometer coils. The superconducting tabs disturb the magnetic field locally altering the magnetic flux enclosed by the coils. The position and orientation of the tabs are adjusted such, that the sensitivity of the gradiometer to the uniform magnetic field is reduced. Mechanical balancing is frequency-independent and cannot be used for a compensation of the eddy-currents effect. A relative sensitivity to the residual magnetic field of 10^{-6} can be achieved by application of mechanical balancing (Barbanera *et al.*, 1981).

In electronic balancing, a system of reference magnetometers is included in the measuring setup along with the main high-order gradiometer intended for the Biomagnetic measurements. The signals of the reference gradiometers are mixed with the signal of the main higher order gradiometer in proportions that reduce the sensitivity of the whole setup to the uniform magnetic field. Compensation of the eddy current effect can be implemented by filtering the reference signals. Residual imbalance of 10^{-5} was reported as a result of applying electronic balancing (ter Brake *et al.*, 1989; Vrba, 1996).

Both balancing methods involve minimization of the response of the measuring system to the test magnetic fields. Different types of sources of the test magnetic fields are discussed in the literature. The earth magnetic field (Vrba *et al.*, 1982), (Jaworski and Crum, 1980) can be used for this purpose as well as magnetic fields produced by Helmholtz coils (ter Brake *et al.*, 1989), three-square-coils set (Rijpma, 2002), a system of coaxial circular coils (Primin *et al.*, 2002), and a rotating magnetic dipole (Vrba, 1996; Vrba and McCubbin, 1983). The environmental magnetic noise can serve as a test field as well. For instance in (Wltgens and Koch, 2000; Broussov *et al.*, 2003) signals of reference sensors are mixed with a signal of a primary sensor via multiplicative coefficients calculated based on observations of the environmental noise. That is, the environmental noise is recorded prior the actual Biomagnetic measurements by all references and by the primary sensor. Subsequently, the multiplicative mixing coefficients are calculated by fitting the reference signals in the signal of the main sensor by means of linear regression. The linear regression can be performed in both, time and frequency domains.

1.3 Objectives and layout of the thesis

Fetal magnetocardiograms are recorded in a few research centers in the world equipped with shielded rooms. The necessity of the magnetically shielded room and the necessity of the constant supply of liquid helium hinder the daily use of fetal magnetocardiography in hospitals. The $4K$ FHARMON (Dutch acronym for Foetale HARt MONitor) project aims at the construction of a relatively inexpensive low-T_c fetal magnetocardiograph with a few measuring channels. The three main requirements for the FHARMON fetal magnetocardiograph are:

- The intrinsic noise of the system has to be of order of $10fT/\sqrt{Hz}$.
- The system has to be cryocooler-cooled. As only low-T_c SQUIDs technology can provide the adequate sensitivity, the system needs to be cooled to about $4K$.
- The system has to be able to suppress the environmental magnetic interference beyond the level of intrinsic sensitivity without the application of a magnetically shielded room.

Research within the FHARMON project is conducted along two lines: a magnetically silent $4K$ cryocooler and environmental interference suppression without the application of a magnetically shielded room. The objective of the work presented in this

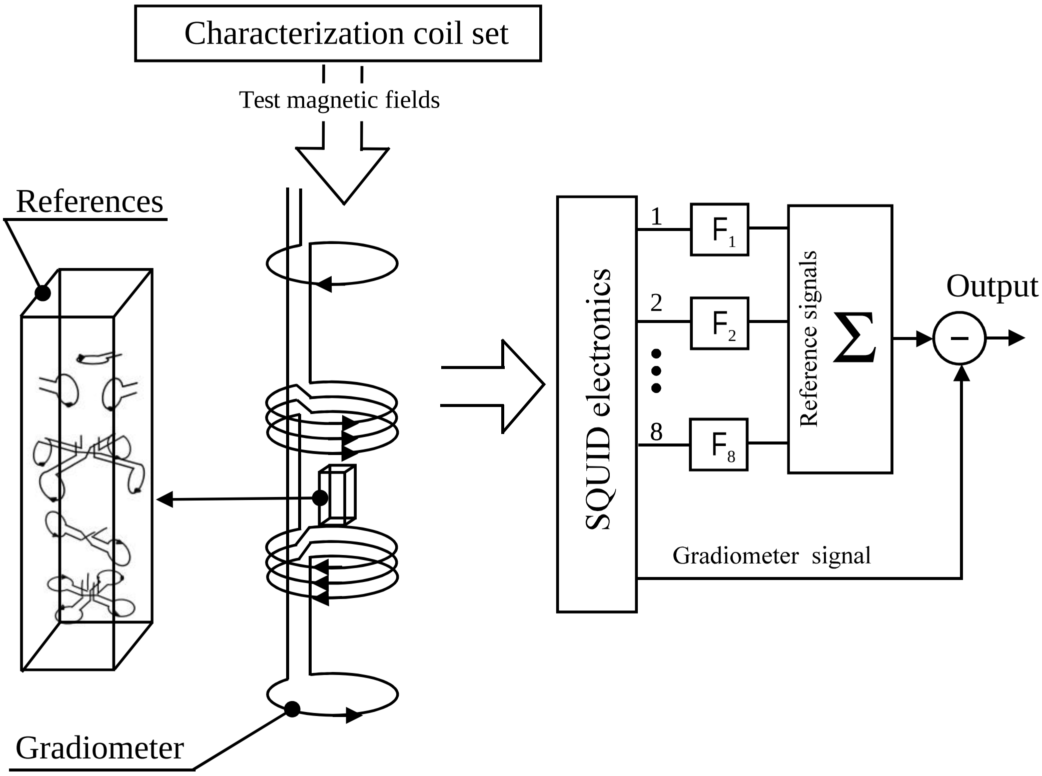

Figure 1.9. Schematic illustration of the gradiometer balancing experiment. Boxes $F_1 ... F_8$ denote filters.

thesis is to design a highly balanced gradiometer for the FHARMON system that would enable fMCG measurements in unshielded environment.

The FHARMON system utilizes a highly balanced third-order synthetic gradiometer as an alternative to the magnetically shielded room. The gradiometer is schematically depicted in figure 1.8d. The gradiometer can adapt to the level of environmental noise. That is, the signal of the lower second-order gradiometer is used in relatively low-noise environments whereas the signal of the synthetic third-order gradiometer is used in noisy environments. This adaptation allows to improve the signal-to-noise ratio in the low-noise environments due to better coupling of the magnetic flux to the SQUID. In order to reach the required level of environmental interference suppression, the gradiometer is electronically balanced. The gradiometer balancing procedure is schematically depicted in figure 1.9. A system of reference magnetometers and first-order gradiometers is introduced into the system for the purpose of electronic balancing. The signals of the two second-order gradiometers and the reference signals are read out separately and mixed in the software. A characterization coil set is used to generate the test magnetic fields that correspond to the uniform magnetic fields in three orthogonal directions and five first-order linearly-independent gradients. The gains of the reference channels are adjusted such, that the response of the system is nullified for all applied test magnetic fields.

The third-order gradiometer of the FHARMON system has a number of geometrical parameters (these are denoted R,S,D,C in figure 1.8d) that can be optimized for the maximal signal-to-noise ratio of the recorded fMCG. The optimization of these geometrical parameters is discussed in chapter 2. The quality of the gradiometer balancing depends on the homogeneity of the test magnetic fields applied to the gradiometer during the balancing procedure. The required homogeneity of the test magnetic fields (and thus the complexity of the characterization coil set) is a function of initial (i.e before balancing) and required (i.e after balancing) imbalance coefficients. The imbalance coefficients are defined in chapter 3. The expected initial imbalance coefficients are estimated in chapter 3 as well. The design of the characterization coil set is discussed in chapter 4 after a short consideration of the main requirements. The mechanical construction of the characterization coil set and gradiometer balancing experiments are discussed in chapter 5. The gradiometer is enclosed by a conducting radio frequency interference shield as well as by a thermal isolation. The thermal magnetic noise generated by these shields decreases the sensitivity of the system. The eddy currents induced by this shields are coupled to the gradiometer inducing frequency dependent imbalance. Methods of estimation of the influence of these effects on the system performance are needed. Such methods were developed in (Rijpma, 2002). In chapter 6 these methods are confirmed experimentally.

Chapter 2

Gradiometer optimization

2.1 Introduction

In this chapter, the optimization of the gradiometer is discussed. The gradiometer is shown schematically in figure 2.1a. This is a schematic representation of the gradiometer depicted in figure 1.8d. It consists of two second-order gradiometers. The signals of the two second-order gradiometers are read out separately and subtracted in the computer software. The order of the gradiometer can be adapted to the environmental noise level. That is, the second-order gradiometer can be used in low-noise environments whereas the third-order gradiometer can be used in relatively noisy environments.

There are four parameters of the gradiometer that have to be optimized (see figure 2.1a): the radius of the sensing coils (R), the length of the second-order gradiometer (D), the separation between the two inner turns of the second-order gradiometer (S) and the separation between the two second-order gradiometers (C). The optimal geometry of the gradiometer, i.e., the one that maximizes the SNR, depends on the level of environmental interference as well as on the position of the signal source in relation to the gradiometer. Different values of the signal and interference related parameters require gradiometers of different geometries. The geometry of the gradiometer is optimized to provide the maximum of the mean SNR averaged for all combinations of the parameters.

The magnetic noise that arises from the conducting parts of the measuring setup decreases the SNR. In the optimization, the maximum level of the magnetic noise that allows recording fMCG signals of all relevant magnitudes with a sufficient SNR is deduced.

The second-order gradiometers that are shown in figure 2.1 consist of six sections. Each section comprises one turn of superconducting wire. Gradiometers that have several turns in each section are frequently used in the instrumentation for Biomagnetism. An example of such a multiturn gradiometer is shown in figure 2.1b. In this chapter, the usefulness of multiturn gradiometers is investigated as well.

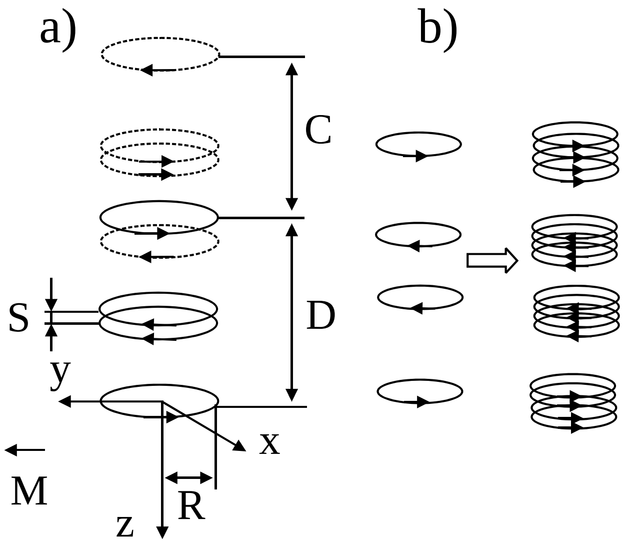

Figure 2.1. a) The third-order gradiometer to be optimized. The gradiometer consists of two second-order gradiometers (solid and dashed lines). The second-order gradiometer (solid lines) will be used in low noise environments while the third-order gradiometer will be used in noisy environments. A magnetic dipole (M) is used to model the magnetic field generated by the fetal heart (see text). b) An illustration of the formation of a symmetric multiturn second-order gradiometer.

2.2 Optimization method and assumptions

First, the measuring system, the signal source and the environmental interference are discussed (sections from 2.2.1 to 2.2.3). Then, in section 2.2.4, the equation that was used to evaluate the SNR is given. In that section, the assumed values of the variables that were used to calculate the SNR are summarized in table 2.1. The optimization procedure is discussed in section 2.2.6, after the introduction of a performance function in section 2.2.5. Finally, in section 2.2.7, the method that was used to investigate the usefulness of the multiturn gradiometers is discussed.

2.2.1 Measuring system

The standard layout of a SQUID measuring system is depicted in figure 2.2. The magnetic flux Φ_g through the gradiometer with inductance L_g induces a current in the superconducting closed circuit L_g, L_{tw}, L_{in}. The current flowing in the input inductance L_{in} produces a magnetic flux Φ_{SQUID} in the SQUID. The flux transfer efficiency equals

$$K_\Phi = \frac{\Phi_{SQUID}}{\Phi_g} = \frac{M_{in}}{L_{in} + L_g + L_{tw}} \tag{2.1}$$

where M_{in} is the mutual inductance between the input coil and the SQUID and L_{tw} is the self inductance of the twisted wires that interconnect the coils of the gradiometer and connect them to the SQUID. The whole setup is enclosed by several layers of aluminum-coated Mylar film (superinsulation) as well as a radio-frequency interference (RFI) shield. The RFI shield is typically made of a single layer of a conducting material such as aluminum paint, aluminum foil or copper meshing. Both, the superinsulation and the RFI shield comprise conductive components and produce

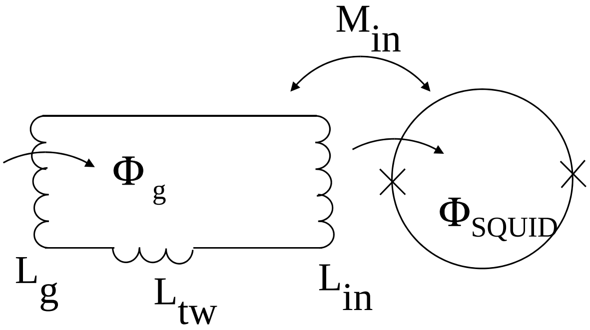

Figure 2.2. The standard layout of a SQUID measuring system.

magnetic noise. The shielding by the RFI shield improves with increasing thickness and conductivity of the material that is used in the shield. In practice, it is desirable to have a shielding effect as large as possible. However, the magnetic noise due to the shield increases with the thickness and the conductivity of the material as well. A similar trade-off holds for the superinsulation. Therefore, the maximum level of the magnetic noise due to the shield that allows realizing an adequate SNR needs to be investigated. In the optimization, this magnetic noise B_s is varied between 0 and $10fT/\sqrt{Hz}$, which is the worst sensitivity level that is acceptable in fetal magnetocardiography (ter Brake *et al.*, 2002). The geometry of the gradiometer is optimized for all assumed values of B_s. Then, B_s is chosen such, that the SNR is acceptable. The intrinsic sensitivity of the measuring setup is determined by two noise sources: the magnetic field noise of the RFI shield plus the superinsulation (B_s) and the magnetic flux noise of the SQUID plus readout electronics (Φ_s). In the FHARMON project demonstrator, the commercially available SQUIDs type CSblue of Supracon (www.supracon.com) are used. The parameters of the SQUIDs are

$$\Phi_s = 7.2\frac{\mu\Phi_0}{\sqrt{Hz}}; L_{in} = 320nH; M_{in} = 10nH \tag{2.2}$$

The self inductance of the gradiometer is evaluated using expressions that are available in (ter Brake, 1986). The self inductance of the twisted wires (L_{tw}) is evaluated using the following expression (Cantor, 1996):

$$L_{tw} = 0.5l \tag{2.3}$$

where l is the length of the twisted wires in millimeters and L_{tw} is the resulting inductance in nH.

2.2.2 Signal source

The magnetic field due to the fetal heart plus the field due to the volume currents can be modeled by an equivalent magnetic dipole (Stinstra, 2001). The position of the dipole in relation to the gradiometer is shown in figure 2.1a. The gradiometer is invariant to the rotation around the $z-$ axis. Consequently, the coordinate system is chosen such that the $x-$ component of the displacement vector equals zero. The $x-$ component of the equivalent magnetic dipole does not contribute to the $z-$ component of the magnetic field and is omitted from the consideration. The results presented in (Stinstra, 2001) suggest that the angle between the equivalent magnetic dipole and the $xy-$ plane is at most 40^o where the $xy-$ plane is tangential to the maternal abdominal surface. Calculations show that a rotation of the magnetic dipole out of the $xy-$ plane by 40^o does not affect the optimization results significantly. Therefore, the $z-$ component of the equivalent magnetic dipole is neglected as well.

The net flux through the gradiometer due to the equivalent magnetic dipole is evaluated by integrating numerically the following equation:

$$\Phi_D = \left| \sum_{m=1}^{N} s_m \frac{\mu_0}{4\pi} \int_0^{2\pi} \frac{R \cdot M \cdot (z-z_m) \cdot \sin\beta \cdot d\beta}{[(R\cos\beta)^2 + (y - R\sin\beta)^2 + (z-z_m)^2]^{\frac{3}{2}}} \right| \tag{2.4}$$

where z_m stands for the z- coordinate of the m-th turn of the gradiometer and $s_m = 1$ if the m-th turn of the gradiometer is wound clockwise; $s_m = -1$ if the turn is wound counterclockwise; N is the number of turns in the gradiometer and β is the parameter of the parameterization of a single turn. The depth of the dipole is assumed to be equal to $z = 0.05$, 0.1 and 0.15 meters. These correspond to the minimum, the medium and the maximum depths expected for the equivalent magnetic dipole. The $y-$ coordinate of the dipole is chosen such that the net magnetic flux through the gradiometer is maximized. The minimal expected value of the magnitude of the equivalent magnetic dipole

$$M = 7nA \cdot m^2 \tag{2.5}$$

is estimated based on data presented in (Kandori *et al.*, 1999).

2.2.3 Environmental interference

The frequency content of the fMCG signal is assumed to be between $1Hz$ and $100Hz$. The maximal expected magnitudes of Power Spectral Density (PSD) at the frequency of $1Hz$ of the second- and third- order gradients of the interfering environmental magnetic field are estimated from the collection of PSDs of the zero- and first- order gradients presented in (Vrba and Mckay, 1998). In order to make this estimation, it was assumed that the magnitude of the interfering magnetic fields is proportional to the inverse cube of the distance. Based on the estimated magnitudes and assuming a worst-case frequency dependence of the PSD to be proportional to $1/f$, the maximal Root Mean Square (RMS) values of the second- and third- order gradients of the interfering magnetic field are determined as:

$$G^{(2)}_{MAX} = 0.53 \cdot 10^{-10} T \cdot m^{-2} \tag{2.6}$$

$$G^{(3)}_{MAX} = 0.11 \cdot 10^{-11} T \cdot m^{-3} \tag{2.7}$$

An environmental noise parameter ξ is introduced such that the actual RMS value of a gradient of the interfering magnetic field that is considered is:

$$G_{ENV}^{(n)} = G_{MAX}^{(n)} \cdot \xi \tag{2.8}$$

where n is the order of the gradient. The parameter ξ is varied between 0 and 1. The second- and third- order gradiometers are assumed to be sensitive to the second- and third- order gradients of the interfering magnetic field only. That is, the gradiometers are assumed to be perfectly balanced and the higher-order gradients of the interfering magnetic field are neglected. The net flux through the gradiometer due to the environmental interference are evaluated as:

$$\Phi_{ENV}^{(n)} = G_{ENV}^{(n)} \cdot b^{(n)} \tag{2.9}$$

where $b^{(n)}$ is the sensitivity of the gradiometer to the corresponding gradient. Neglecting the spatial variations of the interfering magnetic field in the transversal directions, these sensitivities can be evaluated as:

$$b^{(2)} = 0.5 \cdot \pi R^2 \cdot (D^2 - S^2) \tag{2.10}$$

$$b^{(3)} = 3 \cdot C \cdot b^{(2)} \tag{2.11}$$

where R,D,S and C are the geometrical parameters described by figure 2.1a.

Apart from the intentional sensitivities given in (2.10) and (2.11), a practical gradiometer has parasitic sensitivities (so called imbalances) to lower order gradients of the interfering magnetic field (Vrba, 1996). However, it is assumed that the second- and third- order gradiometers are manufactured and balanced sufficiently well to be in their intrinsic regimes (Vrba, 1996). In that case, the noise component of the signal is defined either by the intrinsic noise of the measuring system or by the second- or third- order gradients of the interfering magnetic field. The field imbalance that is required to keep the gradiometers designed in the subsequent sections in their intrinsic regimes is of order of 10^{-6}. The required first-order gradient imbalance is of the order of $10^{-3} - 10^{-4}$. From (Vrba, 1996) it was concluded that it is feasible to realize these imbalances using electronic balancing. Consequently, imbalance contributions are neglected in the optimization procedure.

2.2.4 Signal-to-noise ratio

The SNR of the fMCGs is expressed as

$$SNR = 20 \log \frac{\Phi_D}{\sqrt{\left(\Phi_{ENV}^{(n)}\right)^2 + \triangle f (\pi R^2 B_s)^2 + (n-1) \triangle f \frac{(\Phi_s)^2}{K_\Phi^2}}} \tag{2.12}$$

where $\triangle f = 100 Hz$ is the bandwidth of the fetal heart signal. The numerator in the last equation equals the amplitude of the fetal heart signal expressed as the net

Table 2.1. Summary of the assumed variables that are used to calculate the SNR

Variable	Description	Value
L_{in}	Input self inductance of SQUID $[nH]$	320
M_{in}	Input mutual inductance of SQUID $[nH]$	10
l	Length of the twisted wires [mm]	300
Φ_s	Equivalent flux noise of SQUID $[\mu\Phi_0/\sqrt{Hz}]$	7.2
B_s	Field noise of the radiation shield $[fT/\sqrt{Hz}]$	$0...10^{\star}$
z	Depth of the equivalent dipole $[mm]$	$50:50:150^{*}$
M	Magnitude of the equivalent magnetic dipole $[nA \cdot m^2]$	7
$G_{ENV}^{(2)}$	Second-order gradient of the env. interference $[T \cdot m^{-2}]$	$0.53 \cdot 10^{-10} \times\xi$
$G_{ENV}^{(3)}$	Third-order gradient of the env. interference $[T \cdot m^{-3}]$	$0.11 \cdot 10^{-11} \times\xi$
ξ	Noise parameter	$0...1^{\star}$
R	Radius of the gradiometer $[mm]$	$5:2.5:200^{*}$
D	Length of the second-order gradiometers $[mm]$	$20:10:300^{*}$
S	Separ. between the inner coils of the second-order gradiometers	$(1:5.16:99) \times 10^{-2} \times D^{*}$
C	Separ. between the two second-order gradiometers $[mm]$	$10:10:300^{*}$
m	the number of turns in each coil of the second-order gradiometer	$2:1:5*$
$\triangle z$	the separation between the turns of the second-order gradiometer $[mm]$	$1...20^{\star}$

the following notations are used: $*$ min:step:max; $\star$ min...max.

magnetic flux through the gradiometer. The denominator equals the RMS value of the interfering noise expressed as the net magnetic flux through the gradiometer as well. The three terms in the denominator represent the RMS values of the environmental noise, the magnetic noise of the RFI shield plus the superinsulation and the noise of SQUID plus readout electronics. In order to determine the required SNR, a noiseless fMCG signal is mixed in different proportions with white noise that represented the noise of the measuring system. Based on the resultant mixtures of the fMCG signal and noise, it is concluded that a SNR of $15dB$ is required in order to make the fetal heart beats discernible in the fMCG recordings (see section 2.3.1).

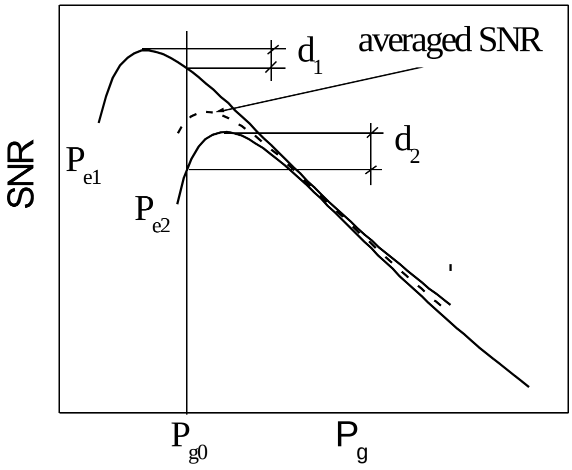

Figure 2.3. A stylized plot that illustrates the optimization concept. The two solid curves correspond to gradiometers that operate in two different environments that are described by parameters P_{e1} and P_{e2}. If the parameter of the gradiometer is chosen to be equal to P_{g0}, the SNRs will deviate from their maxima by d_1 and d_2, respectively. The optimization aims at the maximization of the averaged SNR.

2.2.5 Optimization performance function

The SNR given in (2.12) can be viewed as a function of seven independent variables

$$SNR = SNR(D, R, S, C, B_s, z, \xi) \tag{2.13}$$

These independent variables can be divided in two groups. The first group comprises the geometrical parameters of the gradiometer (D, R, S, C) that have to be optimized. The second group comprises the parameters of the environment in which the gradiometer is operated (B_s, z, ξ). The parameters z and ξ are independent of the optimization procedure. The parameter B_s is determined by optimizing the geometry of the gradiometer for all assumed values of B_s and choosing B_s such, that the SNR is acceptable.

The performance function is introduced by means of a simplified example in which the SNR is assumed to be a function of one geometrical parameter of the gradiometer(P_g) and one parameter of the environment (P_e)

$$SNR = SNR(P_g, P_e) \tag{2.14}$$

For instance, the parameter P_g could represent the radius of the gradiometer (R) and the parameter P_e could represent the depth of the equivalent magnetic dipole (z). In figure 2.3, schematic curves of the SNR versus the parameter of the gradiometer are shown. The two solid curves represent the SNR of the gradiometers that operate in different environments that are described by $P_e = P_{e1}$ and $P_e = P_{e2}$. If the parameter of the gradiometer is chosen to be P_{g0} then the actual SNR is d_1 lower than the maximal obtainable in the case $P_e = P_{e1}$ and d_2 below the maximal SNR in the case $P_e = P_{e2}$. The optimization of P_g aims at a maximum of the averaged SNR indicated in figure 2.3. Therefore, the performance function can be expressed as

$$J(P_g) = \frac{1}{2}\left(SNR(P_g, P_{e1}) + SNR(P_g, P_{e2})\right) \tag{2.15}$$

The performance function given by the last equation differs from the actual performance function used in the optimization in the number of the parameters considered.

2.2.6 Optimization procedure

The optimization consists of two steps. In the first step, the optimal geometrical parameters of the second-order gradiometer are derived. Equation (2.12) is evaluated using the set of values of variables listed in table 2.1. Consequently, for each combination (i) of the environmental conditions the following function of three variables is derived:

$$SNR_i = SNR_i(D, R, S) \tag{2.16}$$

The mean SNR (similar to (2.15)) averaged for different combinations is evaluated as

$$J^{(2)}(D, R, S) = \frac{1}{N} \sum_{i=1}^{N} SNR_i(D, R, S) \tag{2.17}$$

where N is the number of combinations of the environmental parameters. The arguments of the maximum of the last equation are considered as the geometrical parameters of the optimal second-order gradiometer.

The third-order gradiometer consists of two identical second-order gradiometers that are optimized as discussed above. In the second step of the optimization, the axial separation (C) between the two second-order gradiometers is derived following the same procedure that is used for the optimization of the second-order gradiometer with the difference that the performance function has only one independent variable

$$J^{(3)}(C) = \frac{1}{N} \sum_{i=1}^{N} SNR_i(C) \tag{2.18}$$

2.2.7 Number of turns

The number of turns of the gradiometer coils has a two-fold effect on the signal transferred to the SQUID. Firstly, it increases the net magnetic flux through the gradiometer which roughly scales with the number of turns. Secondly, it decreases the flux transfer efficiency which is given by (2.1) because the self inductance of the gradiometer L_g increases with the number of turns as well. The inductance of the gradiometer increases more rapidly with the number of turns than the net magnetic flux through the gradiometer does. Therefore, the signal transferred to the SQUID can be increased by increasing the number of turns only if the self inductance of the SQUID input coil is sufficiently large compared to that of the gradiometer.

A one-turn and a corresponding four-turn second-order gradiometers are shown in figure 2.1b as an example. The usefulness of the m-turn gradiometers is investigated by comparing the magnetic flux transferred to the SQUID in the case of a one-turn gradiometer with that of an m-turn gradiometer

$$Q = 20 \log \left(\frac{\Phi_m}{L_m + L_{in} + L_{tw}} \frac{L_1 + L_{in} + L_{tw}}{\Phi_1} \right) \tag{2.19}$$

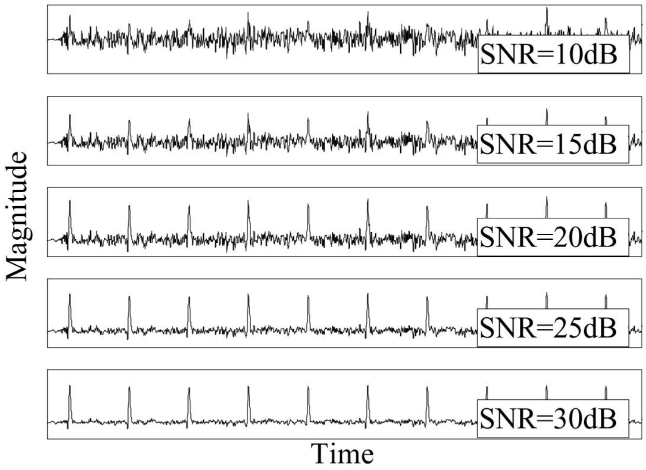

Figure 2.4. A noiseless fMCG signal mixed in different proportions with white noise. This figure is used for the qualitative evaluation of the SNR. It was concluded that a SNR of $15dB$ is sufficient to make the fetal heart beats discernible in fMCG recordings.

where L_1 and L_m are the self inductances of the one-turn and the corresponding m-turn gradiometers and Φ_1 and Φ_m the net magnetic fluxes, respectively. Increasing the number of turns increases the magnetic flux coupled to the SQUID only if the parameter Q given by the last equation is greater than zero.

2.3 Results

2.3.1 Signal-to-noise ratio

The fMCG signal mixed with white noise in different proportions is shown in figure 2.4. From these plots, it is concluded that the SNR of the fetal magnetocardiogram has to be in the range $10 - 15dB$ in order to make the fetal heart beats discernible in the recordings. This would allow the averaging of the fetal heart beats with the subsequent determination of the intracardiac intervals (Stinstra, 2001). In the case of the third-order gradiometer, the contribution of the SQUIDs to the noise power of the measuring system is twice as large as in the case of second-order gradiometer. Assuming that the third-order gradiometer rejects all environmental interferences, the difference in the SNR between the second-order gradiometer under condition $\xi = 0$ and the third-order gradiometer for all values of ξ is less than $3dB$. Thus, the SNR of the second-order gradiometer in a noise-free environment ($\xi = 0$) could be considered as a 'SNR characteristic' of both second- and third- order gradiometers. In what follows, the gradiometer is considered to be designed sufficiently well if the SNR of the weakest fMCG signal measured by the second- order gradiometer in the noise-free environment is equal to $15dB$. The weakest fMCG signal considered corresponds to the smallest magnitude of the equivalent magnetic dipole of $7nA \cdot m^2$ and the largest depth of the dipole of $0.15m$.

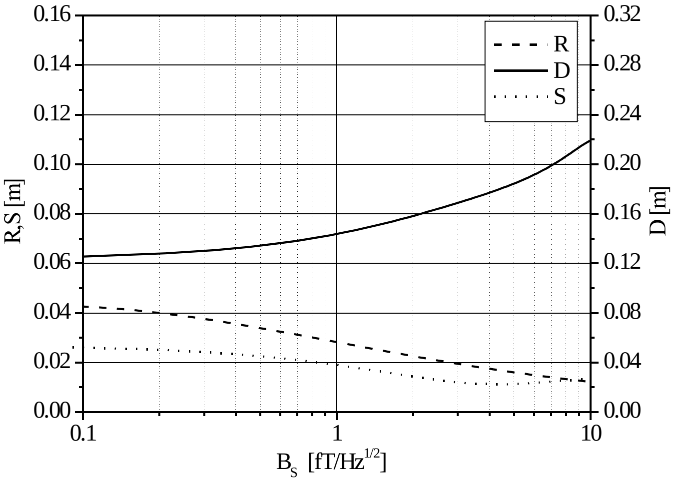

Figure 2.5. The optimal length (D), the radius (R) and the separation between the inner coils (S) versus magnetic noise B_s. The environmental noise parameter is assumed to be in between $\xi = 10^{-4}$ and 10^{-1}. Other parameters are assumed to have values that are listed in table 2.1.

2.3.2 Optimization of the second-order gradiometer

In figure 2.5, the radius, the length and the separation between the inner turns of the single-turn second-order gradiometers that are optimal for $\xi = 10^{-4} - 10^{-1}$ and $z = 0.05, 0.1, 0.15m$ are shown as a function of B_s. The parameter ξ is varied with a unitary step in the exponent. The lower limit of the parameter $\xi = 10^{-4}$ is chosen such, that the contribution of the environmental interference to the SNR can be neglected. The curves that are presented in figure 2.5 are the results of polynomial fits of the calculated data. These fits are made to smoothen quantization errors due to the finite step in the grid of values of independent variables for which (2.12) is evaluated. In the absence of the magnetic noise of the RFI shield and the superinsulation ($B_s = 0fT/\sqrt{Hz}$; not shown in figure 2.5), the optimal gradiometer has the largest radius $R = 0.045m$ and the shortest length $D = 0.12m$. The increase of the magnetic noise B_s leads to an increase of the gradiometer length and a decrease of its radius.

In figure 2.6, the SNR, calculated for the gradiometers of the optimal dimensions

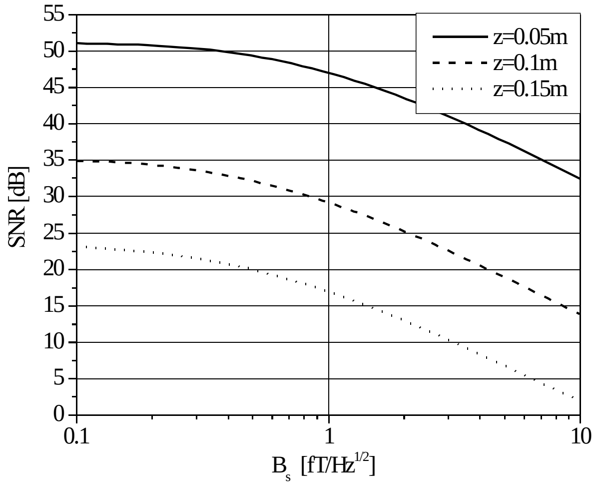

Figure 2.6. The SNR calculated for the second-order gradiometers of the optimal dimensions that are shown in figure 2.5. The environmental noise parameter is assumed to be equal to $\xi = 0$. The magnitude of the equivalent dipole is assumed to be equal to the minimal expected value.

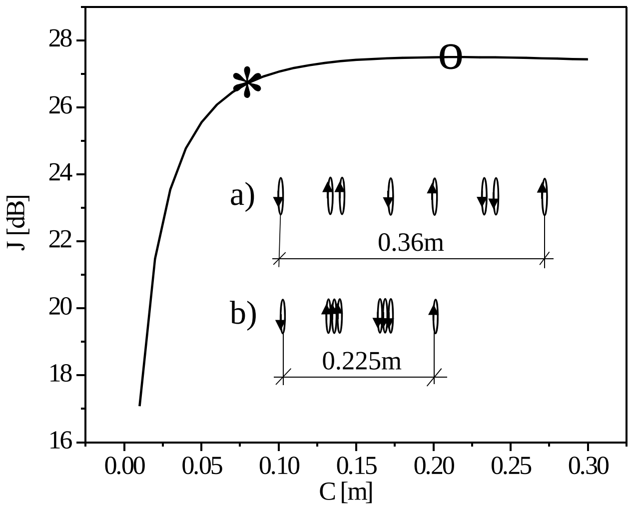

Figure 2.7. The performance function of the optimization of the third-order gradiometer ((2.18) in the text). The maximum of the performance function (indicated by the circle) corresponds to the separation between the second-order gradiometers of $C = 0.21m$. The decrease of the separation to a value of $0.075m$ (indicated by the asterisk) leads to a decrease of the performance function by $0.8dB$. The third-order gradiometers that correspond to the separations of $C = 0.21m$ and $C = 0.075m$ are shown in insets a and b respectively.

that are presented in figure 2.5, is shown. The SNR was calculated assuming a noise-free environment ($\xi = 0$). From figure 2.6, it follows that, if the magnetic noise due to the RFI shield and the superinsulation equals $1.5fT/\sqrt{Hz}$, the recording of the weakest fMCG signal will have a SNR of $15dB$ which is sufficient for the detection of the fetal heart beats. The geometrical parameters of the corresponding gradiometer can be deduced from figure 2.5 as $R = 0.025m, D = 0.15m, S = 0.016m$. This gradiometer in combination with a maximum shield noise B_s of $1.5fT/\sqrt{Hz}$ provides an adequate performance of the gradiometer. A better performance in terms of SNR can only be obtained if B_s can be reduced to a lower level. Then the geometry of the gradiometer would change as indicated in figure 2.5.

2.3.3 Optimization of the third-order gradiometer

The performance function (2.18) for the optimization of the third-order gradiometer is shown in figure 2.7. For the noise parameter (ξ) twenty points logarithmically spaced between 0.1 and 1 are taken. The shield noise and the geometrical parameters of the two second-order gradiometers are assumed to be equal to the optimal ones discussed above. The maximum of the performance function is designated in figure 2.7 by the circle. The maximum corresponds to a separation between the second-order gradiometers of $0.21m$. However, a decrease of the separation from $0.21m$ to $0.075m$ (indicated in figure 2.7 by an asterisk) leads to a small decrease of the performance function from $27.5dB$ to $26.7dB$. The two third-order gradiometers that correspond to the separations of $0.21m$ and $0.075m$ are shown in figure 2.7 as well. The decrease of the separation between the two second-order gradiometers leads to a decrease of the total length of the third-order gradiometer of 37% without significant change of the performance. Therefore, a separation of $C = 0.075m$ is chosen. The SNRs of the second- and third- order gradiometers are shown in figure 2.8 as a function of

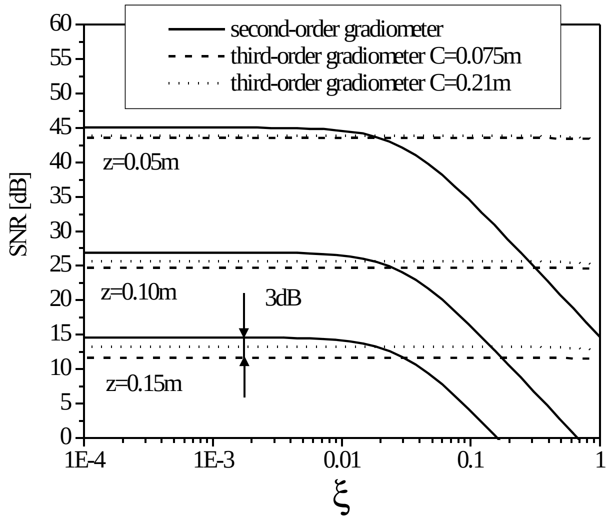

Figure 2.8. The SNR curves calculated for the second- and third- order gradiometers assuming $B_s = 1.5fT/\sqrt{Hz}$ and the minimal magnitude of the equivalent magnetic dipole.

the environmental noise parameter. From the figure, it follows that the second-order gradiometer provides an improvement of the SNR up to $3dB$ over the third-order gradiometer in the low-noise environments. The point where the SNR curves of the second- and third- order gradiometers intersect depends on the depth of the source and is around $\xi = 0.02$. The second-order gradiometer will be used in environments that correspond to ξ less than the above mentioned point. The third-order gradiometer will be used otherwise.

2.3.4 Number of turns

The optimal geometries of the one-turn second-order gradiometers are shown in figure 2.5 as a function of the magnetic noise of the RFI shield plus the superinsulation (B_s). The possibility to increase the magnetic flux transferred to the SQUID by increasing the number of turns of the coils of the optimal second-order gradiometers

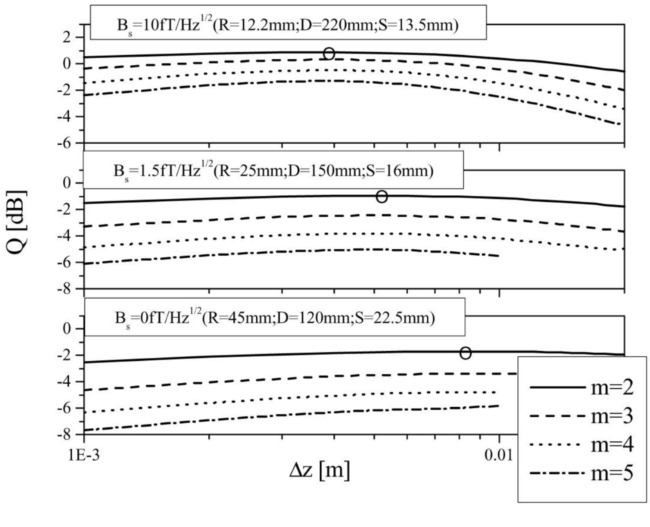

Figure 2.9. The increase of the magnetic flux coupled to the SQUID (2.19) due to increase of the number of turns of the gradiometer (m) as a function of the separation between the turns ($\triangle z$) with source depth $z = 0.05m$. The three plots correspond to three different geometries of the initial one-turn second-order gradiometer (see figure 2.5).

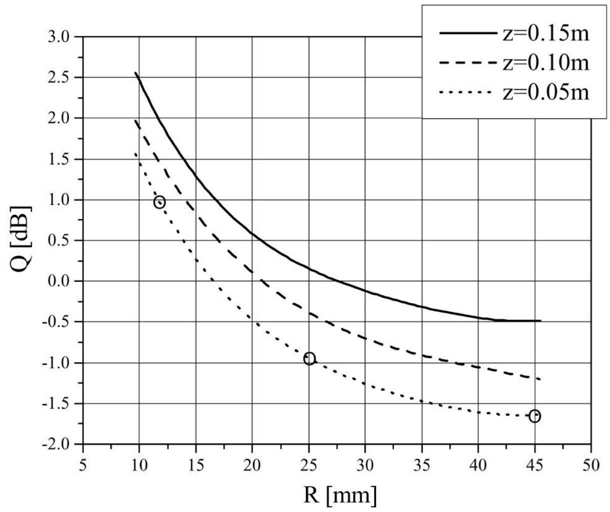

Figure 2.10. The maximum possible increase of the magnetic flux coupled to the SQUID due to increase of the number of turns of the gradiometer. The circles in this figure correspond to the circles in the figure 2.9.

is investigated by evaluating (2.19) for different optimal gradiometer geometries that are given in figure 2.5. The number of turns in each coil (m), the separation between the turns ($\triangle z$) and the depth of the equivalent magnetic dipole (z) are varied as indicated in table 2.1. The parameter Q calculated for $z = 0.05m$ and $B_s = 0fT/\sqrt{Hz}$, $B_s = 1.5fT/\sqrt{Hz}$, $B_s = 10fT/\sqrt{Hz}$ is shown in figure 2.9. The maximal values of the parameter Q for the three gradiometer geometries are indicated in figure 2.9 by circles. The maximal values of the parameter Q for other gradiometer geometries of figure 2.5 are shown in figure 2.10 as a function of the gradiometer radius. From this figure, it follows that the increase of the number of turns only makes sense if the radius of the gradiometer is less than about $20mm$. This corresponds to a magnetic shield noise $B_s > 3fT/\sqrt{Hz}$ in figure 2.5 or minimal SNR $< 10dB$ in figure 2.6. Consequently, it is concluded that the self inductance of the optimal gradiometer geometry that is discussed in the previous sections is too large to increase the magnetic flux transferred to the SQUID by increasing the number of turns ($R = 0.025m, D = 0.15m, S = 0.016m$).

2.4 Conclusion

A third-order gradiometer that consists of two identical symmetric second-order gradiometers was optimized for application in unshielded environments. A performance function was defined in which the average SNR is determined over a range of environmental noise conditions and distances to the signal source. This function was maximized in order to find the optimal gradiometer design. The optimized gradiometer is shown in figure 2.7a. The geometrical parameters of the gradiometer are $R = 0.025m$, $D = 0.15m$, $S = 0.016m$, $C = 0.21m$. It was found that the separation between the second-order gradiometers (C) can be decreased without significant change in the SNR. The maximal magnetic noise due to the radiofrequency interference shield and the superinsulation that allows recording of the fMCG signals of the minimal magnitude with the sufficient SNR of $15dB$ was found to be equal to $1.5fT/\sqrt{Hz}$. The benefit of increasing the number of turns was investigated as well. The self inductance of the optimized gradiometer is too large for this increase to be advantageous.

Chapter 3

Estimation of gradiometer imbalance

3.1 Introduction

In the previous chapter, the optimization of the gradiometer of the FHARMON system is discussed. Ideally, the gradiometer is insensitive to the magnetic field gradients of order less than two (three) if operated in the second (third) order gradiometer regime. However, in practice it is difficult to manufacture a gradiometer such, that its sensitivity to lower-order gradients is eliminated completely. Manufacturing tolerances lead to errors such as differences between the radii of the individual turns or errors in their orientations and positions. These errors create a sensitivity of the gradiometer to lower-order gradients. Apart from that, conducting and superconducting parts of the measuring setup (such as radio-frequency-interference shields and SQUID modules, respectively) disturb the applied magnetic field, thus creating a sensitivity of the measuring setup to lower-order gradients. This residual sensitivity of a gradiometer to lower-order gradients is referred to as imbalance (ter Brake *et al.*, 1989). Imbalance reduces the ability of a gradiometer to suppress environmental interference.

In the FHARMON demonstrator system, the imbalance is compensated by balancing the gradiometer electronically in a characterization coil set. As discussed in chapter 4, the required homogeneity of the magnetic fields and gradients produced by the characterization coils depends on the initial imbalance of the gradiometer. Here, by initial imbalance the imbalance of the unbalanced gradiometer is meant. Thus, it is necessary to evaluate the initial imbalance of the gradiometer. In this chapter, methods for evaluating the initial imbalance of an arbitrary gradiometer by means of computer simulations are discussed. The methods are applied to the evaluation of the initial imbalance of the second- and third- order gradiometers of the FHARMON system.

First, in section 3.2.1 the relevant parts of the FHARMON system are described. Next, in section 3.2.2 the definition of imbalance coefficients is given and their main properties are discussed. Methods for evaluating the imbalance coefficients due to mechanical imperfections, conducting radio-frequency-interference shields and superconducting SQUID modules are discussed in sections 3.2.3, 3.2.4 and 3.2.5, respectively.

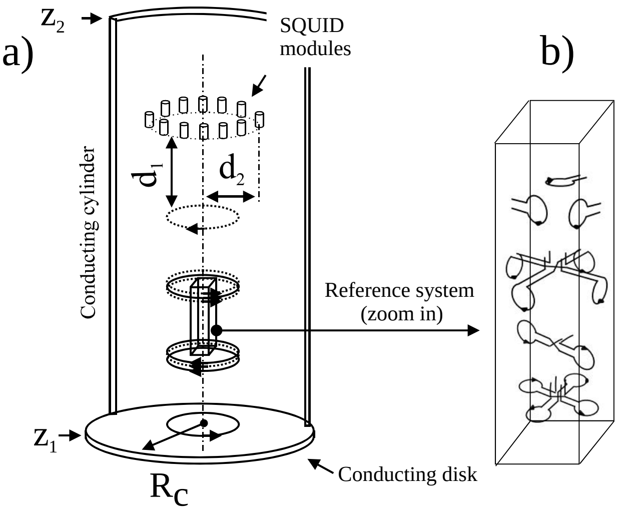

Figure 3.1. A schematic drawing of the FHARMON gradiometer. a) Relative positions of the gradiometer, reference system, superconducting SQUID modules and the radio-frequency-interference shield. b) Gradiometers and magnetometers of the reference system.

The imbalance coefficients resulting from the respective causes for the FHARMON system are reported in sections 3.3.1, 3.3.2 and 3.3.3.

3.2 Method of imbalance estimation

3.2.1 Measuring system

The parts of the FHARMON system relevant to the current discussion are shown in figure 3.1. The twisted wires that interconnect the individual turns of a gradiometer and connect them to the SQUID are omitted. It was estimated that the imbalance induced by properly twisted wires can be neglected. Therefore it is assumed that the gradiometer consists of the sensing turns only. In reality, however, irregularly spaced openings in the twisted wires can appear inducing a significant imbalance. If the geometry of the openings is known, the imbalance can be calculated as discussed in the following sections.

As discussed above, the gradiometer imbalance is compensated by means of electronic balancing. For this purpose, a system of reference channels is included. Its location is shown in figure 3.1a. The reference channels are used to measure the three components of the magnetic field as well as five linearly independent first-order gradients. The magnetometers and gradiometers of the reference system are shown in figure 3.1b. The two second-order gradiometers and the gradiometers and magnetometers of the reference system are connected to ten superconducting SQUID modules. Two more SQUID modules are kept as spares. The location of the SQUID modules relative to the gradiometer is shown in figure 3.1a. The whole setup is enclosed by a thin conducting shield (e.g. a layer of silver paint on the outer surface of the cryovessel).

3.2.2 Definition of imbalance coefficients

Imbalance of a gradiometer is characterized quantitatively by imbalance coefficients that are defined in this section. For convenience, two notations of the spatial coordinates are used: a_1, a_2, a_3 and x, y, z. The unitary vectors are denoted as $\widehat{x}, \widehat{y}, \widehat{z}$. The following notation of magnetic field gradients is used in order to define imbalance coefficients:

$$g^{(n)}_{k_0 k_1 \ldots k_n} = \frac{1}{n!} \left(\frac{\partial^{(n)} B_{k_0}(a_1, a_2, a_3)}{\partial a_{k_1} \ldots \partial a_{k_n}} \right)_{a_1=a_2=a_3=0} \tag{3.1}$$

where B_{k_0} is a component of magnetic field and k_i are the indexes which have a value of either 1, 2 or 3. For instance, $\frac{1}{6} \frac{\partial^{(3)} B_x}{\partial y \partial y \partial z}|_{x=y=z=0}$ is denoted as $g^{(3)}_{1223}$.

Using this notation, the expansion of the $k_0 - th$ component of magnetic field in a Taylor series is expressed as

$$B_{k_0}(a_1, a_2, a_3) = g^{(0)}_{k_0} + \sum \left(g^{(n)}_{k_0 \ldots k_n} \prod_{j=1}^{n} a_{k_j} \right) \tag{3.2}$$

The summation in the last equation is performed over all gradients. However, a gradient tensor of order n has only $2n + 3$ linearly independent components. This is due to the following reasons. Firstly, a magnetic field is curl- and divergence- free. Secondly, the sequence of the differentiation in (3.1) is not important. Consequently, the following rules can be applied to establish a linear dependence between gradients:

- Two gradients are equal if their indexes are related by permutation.
- If the index of a gradient comprises a pair of 3, the gradient can be split as

$$g^{(n)}_{33\ldots} = -\left(g^{(n)}_{22\ldots} + g^{(n)}_{11\ldots} \right) \tag{3.3}$$

Application of these rules to the full set of gradients results in the following (non-unique) set of zero-, first- and second- order linearly independent gradients:

$$g^{(0)}_{1}; g^{(0)}_{2}; g^{(0)}_{3}; \tag{3.4}$$

$$g^{(1)}_{11}; g^{(1)}_{21}; g^{(1)}_{31}; g^{(1)}_{22}; g^{(1)}_{32}; \tag{3.5}$$

$$g^{(2)}_{111}; g^{(2)}_{211}; g^{(2)}_{311}; g^{(2)}_{221}; g^{(2)}_{321}; g^{(2)}_{222}; g^{(2)}_{322}. \tag{3.6}$$

By using the two rules, the expansion of a component of magnetic field given in (3.2) can be expressed in terms of linearly independent gradients only. For instance, the zero- and first- order terms of this expansion read

$$B_x \widehat{x} = \left(g^{(0)}_{1} + g^{(1)}_{11} x + g^{(1)}_{21} y + g^{(1)}_{31} z + \ldots \right) \widehat{x} \tag{3.7}$$

$$B_y\widehat{y} = \left(g_2^{(0)} + g_{21}^{(1)}x + g_{22}^{(1)}y + g_{32}^{(1)}z + ...\right)\widehat{y} \tag{3.8}$$

$$B_z\widehat{z} = \left(g_3^{(0)} + g_{31}^{(1)}x + g_{32}^{(1)}y - (g_{11}^{(1)} + g_{22}^{(1)})z + ...\right)\widehat{z} \tag{3.9}$$

Next, imbalance coefficients are defined as the sensitivity of the gradiometer to terms of this expansion that comprise the same gradients. For example, the gradient $g_{21}^{(1)}$ is included in (3.7) in the term $g_{21}^{(1)}y\widehat{x}$ and in (3.8) in the term $g_{21}^{(1)}x\widehat{y}$. Thus, the sensitivity of the gradiometer to a magnetic field of the form

$$\overrightarrow{B} = g_{21}^{(1)}(y\widehat{x} + x\widehat{y}) \tag{3.10}$$

is characterized by the imbalance coefficient

$$C_{21}^{(1)} = \frac{1}{g_{21}^{(1)}}\frac{1}{A}\int\int_S g_{21}^{(1)}(y\widehat{x} + x\widehat{y}) \cdot \overrightarrow{dS} \tag{3.11}$$

where A is the sensing area of a single gradiometer turn and S is the total sensing area of the gradiometer. Analogously, the definition of imbalance coefficients in general terms is given by the following equation:

$$C_{k_0...k_n}^{(n)} = \frac{1}{g_{k_0...k_n}^{(n)}}\frac{1}{A}\int\int_S \overrightarrow{B}_t \cdot \overrightarrow{dS} \tag{3.12}$$

The field $\overrightarrow{B}_t$ is referred to as test magnetic field. The zero-, first- and second- order imbalances and the corresponding test magnetic fields are listed in table 3.1. The zero-order imbalance coefficients are dimensionless and imbalance coefficients of order n have the dimension m^n. Using the definition of imbalance coefficients given in (3.12), the net magnetic flux through a gradiometer can be expressed as

$$\Phi = A\sum C_{k_0...k_n}^{(n)}g_{k_0...k_n}^{(n)} \tag{3.13}$$

Thus, a gradiometer is insensitive to a linearly independent gradient $g_{k_0...k_n}^{(n)}$ if it is constructed such that $C_{k_0...k_n}^{(n)} = 0$.

The definition of imbalance coefficients (3.12) is directly applicable to imbalance caused by mechanical imperfections. However, application to imbalance due to conducting and superconducting parts of the measuring setup requires the test magnetic field (B_t) to be replaced by the total magnetic field.

It can be shown that imbalance coefficients of an order higher than zero depend on the displacement of the gradiometer from the origin of the expansion of the test magnetic field in a Taylor series if the imbalance coefficients of the lower orders are not equal to zero. Apart from that, the balancing of a lower-order imbalance changes the higher-order imbalance coefficients as the sensing area of the reference and the sensing area of the imperfection that causes the imbalance form a small higher-order

Table 3.1. Imbalance coefficients and the corresponding test magnetic fields

Nr.	Imbalance coeff.	Test magnetic field
1	$C_1^{(0)}$	$g_1^{(0)}\widehat{x}$
2	$C_2^{(0)}$	$g_2^{(0)}\widehat{y}$
3	$C_3^{(0)}$	$g_3^{(0)}\widehat{z}$
4	$C_{11}^{(1)}$	$g_{11}^{(1)}\,(x\widehat{x} - z\widehat{z})$
5	$C_{21}^{(1)}$	$g_{21}^{(1)}\,(y\widehat{x} + x\widehat{y})$
6	$C_{31}^{(1)}$	$g_{31}^{(1)}\,(z\widehat{x} + x\widehat{z})$
7	$C_{22}^{(1)}$	$g_{22}^{(1)}\,(y\widehat{y} - z\widehat{z})$
8	$C_{32}^{(1)}$	$g_{32}^{(1)}\,(z\widehat{y} + y\widehat{z})$
9	$C_{111}^{(2)}$	$g_{111}^{(2)}\,((x^2 - z^2)\widehat{x} - 2xz\widehat{z})$
10	$C_{211}^{(2)}$	$g_{211}^{(2)}\,(2xy\widehat{x} + (x^2 - z^2)\widehat{y} - 2yz\widehat{z})$
11	$C_{311}^{(2)}$	$g_{311}^{(2)}\,(2xz\widehat{x} + (x^2 - z^2)\widehat{z})$
12	$C_{221}^{(2)}$	$g_{221}^{(2)}\,((y^2 - z^2)\widehat{x} + 2xy\widehat{y} - 2xz\widehat{z})$
13	$C_{321}^{(2)}$	$g_{321}^{(2)}\,(2yz\widehat{x} + 2xz\widehat{y} + 2xy\widehat{z})$
14	$C_{222}^{(2)}$	$g_{222}^{(2)}\,((y^2 - z^2)\widehat{y} - 2yz\widehat{z})$
15	$C_{322}^{(2)}$	$g_{322}^{(2)}\,(2yz\widehat{y} + (y^2 - z^2)\widehat{z})$

gradiometer. For those reasons, the strict definition of the imbalance coefficients requires the following addition to (3.12):

$$C_{k_0 \dots k_m}^{(m)} = 0; m < n. \tag{3.14}$$

In other words, the lower-order imbalance coefficients have to be balanced before calculating (or measuring) the higher-order imbalance coefficients. However, in practice one can choose the origin of the expansion of the magnetic field in the Taylor series close to both the center of the gradiometer and the center of the reference system. In this case, the condition given in the last equation can be neglected if the dimensions of the reference system are sufficiently small. In the FHARMON system (figure 3.1a), the influence of the lower-order reference channels on the higher- order imbalance coefficients can be neglected.

3.2.3 Imbalance due to geometrical imperfections of the gradiometer

The dependence of the imbalance coefficients on geometrical imperfections of a gradiometer is assessed by means of Monte Carlo simulations. During each iteration of the Monte Carlo simulations the radius, the position, and the orientation of each turn of the gradiometer is randomly modified according to the following expressions:

$$R_j' = R_j + \delta_{R_j} \tag{3.15}$$

$$a'_{i,j} = a_{i,j} + \delta_{a_{i,j}} \tag{3.16}$$

$$\beta'_j = sin^{-1}\left(\frac{\delta_{\beta_j}}{R}\right) \tag{3.17}$$

$$\gamma'_j = sin^{-1}\left(\frac{\delta_{\gamma_j}}{R}\right) \tag{3.18}$$

where R_j and R'_j are the initial and the modified radii of the j-th turn; $a_{i,j}$ and $a'_{i,j}$ are the initial and the modified i-th coordinate of the center of the j-th turn; β'_j is the angle on which the j-th turn is rotated around the x-axis; γ'_j is the angle on which the j-th turn is rotated around the y-axis; $\delta_{a_{i,j}}$, δ_{R_j}, δ_{β_j} and δ_{γ_j} are normally distributed random variables with the same standard deviation. The latter is varied from 10^{-6} to $10^{-3}m$. In the following sections, this standard deviation multiplied by a factor of 2 will be referred to as the manufacturing error (ϵ). Hence, the probability that a random variable δ falls into the interval $[-\epsilon, \epsilon]$ equals 95%. In each iteration of the Monte Carlo simulation, the imbalance coefficients of the randomly modified gradiometer are calculated using (3.12). The maximum expected value of an imbalance coefficient ($C^{(n)}_{k_0 \ldots k_n}$) is chosen such, that 95% of all outcomes of the Monte Carlo simulation falls into the interval $[-C^{(n)}_{k_0 \ldots k_n}, C^{(n)}_{k_0 \ldots k_n}]$.

3.2.4 Imbalance induced by the radiofrequency-interference shield

The radiofrequency-interference shield is modelled as cylindrical and disk-shaped conductors that are electrically isolated from each other (figure 3.1a). First, the eddy-currents induced in the conducting parts by the test magnetic fields (see table 3.1) are calculated. Next, the imbalance coefficients are evaluated using (3.12) and the Biot-Savart law.

The conductors under consideration are electrically thin. Hence, the frequency of the magnetic fields and the conductivity and geometry of the conductors allow us to neglect capacitive and inductive effects. The test magnetic field is assumed to be in the following form:

$$\overrightarrow{B}_t = \overrightarrow{B}_0(x, y, z)e^{j\omega t} \tag{3.19}$$

Thus, the eddy-currents induced in a conducting material of conductivity σ by the applied test magnetic field (B_t) can be described by

$$\nabla \times \overrightarrow{J}(x, y, z) = -k\overrightarrow{B}_0(x, y, z) \tag{3.20}$$

where $\overrightarrow{J}$ is the magnitude of the eddy currents and $k = j\omega\sigma$. The variation of the eddy currents in the direction perpendicular to the surface of the conducting material is neglected as the conductor is assumed to be thin. Consequently, the eddy currents in the disk shaped conductor can be induced only by the z-component of the test magnetic field. The eddy-currents in the cylindrical conductor can be induced only by the z- and r- components. The eddy-currents are derived from a scalar function U as

$$\overrightarrow{J} = \nabla \times (U \cdot \widehat{n}) \tag{3.21}$$

where $\widehat{n}$ is the vector normal to the surface of the conductor. The zero-divergence condition ($\nabla \cdot \overrightarrow{J} = 0$) holds for any choice of U. Equation (3.21) is rewritten as

$$J_\phi(r,\phi) = -\frac{\partial U_1(r,\phi)}{\partial r}; \;\; J_r(r,\phi) = \frac{1}{r}\frac{\partial U_1(r,\phi)}{\partial \phi} \tag{3.22}$$

and

$$J_\phi(\phi,z) = \frac{\partial U_2(\phi,z)}{\partial z}; \;\; J_z(\phi,z) = -\frac{1}{R_c}\frac{\partial U_2(\phi,z)}{\partial \phi} \tag{3.23}$$

for the disk-shaped and the cylindrical conductors, respectively. Combination of (3.20), (3.22) and (3.23) yields

- In the case of a disk-shaped conductor in the presence of a z-component of the test magnetic field

  $$r^2\frac{\partial^2}{\partial r^2}U_1(r,\phi) + \frac{\partial^2}{\partial \phi^2}U_1(r,\phi) + r\frac{\partial}{\partial r}U_1(r,\phi) = kr^2B_z(r,\phi) \tag{3.24}$$

  with boundary condition

  $$J_r(R_c,\phi) = \frac{1}{R_c}\frac{\partial}{\partial \phi}U_1(R_c,\phi) = 0 \tag{3.25}$$

- In the case of a cylindrical conductor in the presence of $r-$ and $z-$ components of the test magnetic field

  $$\frac{1}{R_c^2}\frac{\partial^2}{\partial \phi^2}U_2(\phi,z) + \frac{\partial^2}{\partial z^2}U_2(\phi,z) = kB_r(\phi,z) \tag{3.26}$$

  $$\int_0^{2\pi}\frac{\partial}{\partial z}U_2(\phi,z)d\phi = \frac{-k}{R_c}\int_0^{2\pi}\int_0^{R_c} rB_z d\phi dr \tag{3.27}$$

  with boundary conditions

  $$J_z(\phi,z_1) = -\frac{1}{R_c}\frac{\partial}{\partial \phi}U_2(\phi,z_1) = 0; \tag{3.28}$$

  $$J_z(\phi,z_2) = -\frac{1}{R_c}\frac{\partial}{\partial \phi}U_2(\phi,z_2) = 0; \tag{3.29}$$

where z_1 and z_2 are the z-coordinates of the boundaries of the cylindrical conductor (see figure 3.1a). Note, that the function $U_2(z, \phi)$ has to satisfy (3.26)-(3.29) simultaneously. Equations (3.24)-(3.29) are solved analytically for all test magnetic fields that are listed in table 3.1. The approach that is used to find the analytical solutions is described in (Uzunbajakau *et al.*, 2006).

Next, imbalance coefficients (3.12) are evaluated by calculating the net magnetic flux through the gradiometer. The imbalance coefficients are evaluated at the maximum frequency of interest (100Hz (ter Brake *et al.*, 2002)). The geometrical parameters of the radiofrequency-interference shield are assumed to be equal to that of the FHARMON system: the radii of the disk-shaped and the cylindrical conductors equal $68mm$; the length of the cylindrical conductor equals $850mm$. The distance between the lowermost turn of the gradiometer and the disk-shaped conductor equals $12mm$. The selected conductivity-thickness product of the conducting material equals $180S$. In that case, the thermal noise produced by the shield equals $10fT/\sqrt{Hz}$. This noise level is considered to be the maximum acceptable one for fetal magnetocardiography (ter Brake *et al.*, 2002).

3.2.5 Imbalance induced by the superconducting SQUID modules

Since the region outside the superconducting SQUID modules is current free, the curl of the magnetic field equals zero. Consequently, the magnetic field can be expressed as a gradient of a scalar magnetic potential

$$\overrightarrow{B} = -\nabla\phi_m \tag{3.30}$$

As the divergence of the magnetic field equals zero as well, the scalar magnetic potential can be described by the Laplace equation

$$\nabla^2\phi_m = 0 \tag{3.31}$$

On the surface (Ω) of the SQUID module, the derivative of the scalar magnetic potential in the direction normal to the surface of the SQUIDs module $(\overrightarrow{n})$ vanishes due to the Meissner effect

$$\Omega : \overrightarrow{n} \cdot \nabla\phi_m = 0 \tag{3.32}$$

At infinity, the effect of the module vanishes and the total magnetic field equals the test magnetic field $(\overrightarrow{B}_t)$

$$\infty : -\nabla\phi_m = \overrightarrow{B}_t \tag{3.33}$$

The same set of equations ((3.30)-(3.33)) describes the velocity field of an incompressible unbounded fluid in the vicinity of a rigid obstacle. This problem is solved analytically in (Kochin *et al.*, 1964) for a disk-shaped rigid obstacle. In (Overweg and Walter-Peters, 1978) the same solution is used for evaluation of the distortion of the

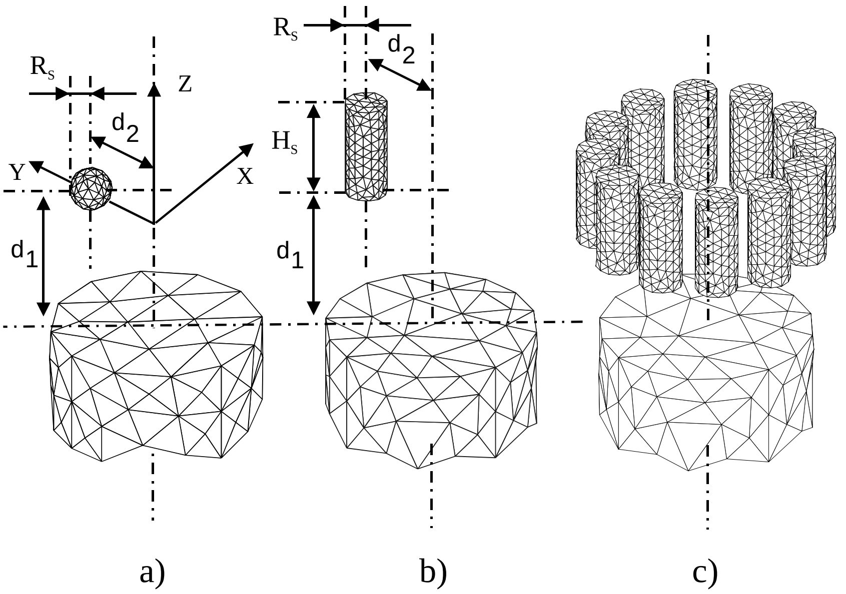

Figure 3.2. Boundaries of the mesh structures that are used in FEM calculations. The truncated cylinder with a relatively large radius in the bottom space of the figure represents the volume occupied by the gradiometer. a) Case study that was used to assess the accuracy of the FEM based on analytical expressions. b) The mesh structure that was used to calculate the imbalance induced by a single SQUID module. c) The mesh structure that was used to calculate the imbalance induced by twelve SQUID modules.

magnetic flux through a circular coil due to a disk-shaped superconductor. In (ter Brake *et al.*, 1991b) a similar approach is used to evaluate imbalance $C_3^{(0)}$

$$\begin{aligned} C_3^{(0)} &= \alpha^3 \cdot \tfrac{2}{\pi} \cdot \left(1 - \tfrac{1+\rho^2}{3}\right)\left(1+\rho^2\right)^{-5/2} \times \\ &\quad (1 - (1+\beta^2)^{-3}) \\ &\quad \alpha = \tfrac{a}{z}; \rho = \tfrac{r}{z}; \beta = \tfrac{b}{z} \end{aligned} \tag{3.34}$$

where z and r are the displacements of the superconducting disk from the top turn of the gradiometer in the axial and the lateral directions; a and b are the radii of the superconducting disk and the gradiometer, respectively. Here, the imbalance coefficients induced by a single SQUID module as well as those induced by the twelve SQUID modules of the FHARMON system (figure 3.2c) are evaluated. The dimensions of the SQUID modules and their displacement from the axis of symmetry of the gradiometer are: $R_s = 5mm$, $H_s = 24mm$, $d_2 = 25.25mm$ (see figure 3.2b). The displacement of the SQUID module from the closest turn of the gradiometer (d_1) is varied from $25mm$ to $225mm$. The total magnetic potential ϕ_m can be viewed as a sum of two potentials

$$\phi_m = \phi_t + \phi_d \tag{3.35}$$

The first potential ϕ_t represents the (applied) test magnetic field. The second potential ϕ_d represents the distortion field caused by the presence of a SQUID module.

Simulations show that the precision of the evaluation of the imbalance coefficients improves significantly, if the potential ϕ_t is subtracted from (3.31)-(3.33) yielding

$$\nabla^2 \phi_d = 0 \tag{3.36}$$

$$\Omega : \overrightarrow{n} \cdot \nabla \phi_d = \overrightarrow{n} \cdot \overrightarrow{B}_t \tag{3.37}$$

$$\infty : -\nabla \phi_d = 0 \tag{3.38}$$

Potential ϕ_d is evaluated by solving (3.36)-(3.38) using FEMLAB software package. The net magnetic flux through the gradiometer is calculated integrating numerically the magnetic field over the sensing surface of the gradiometer. Subsequently, the imbalance coefficients are evaluated using (3.12).

3.3 Results

3.3.1 Imbalance due to geometrical imperfections of the gradiometer

The maximum expected imbalance coefficients of the third-order gradiometer (figure 3.1a) due to geometrical imperfections are shown in figure 3.3 as a function of the manufacturing error. The calculated maximum expected zero- and first- order imbalance coefficients of the second-order gradiometer are almost equal to the corresponding imbalance coefficients of the third-order gradiometer and are not shown. The imbalance coefficients are grouped pairwise in figure 3.3 as the corresponding test magnetic fields are related by rotation around the $z-$ axis and the gradiometer is invariant to such a rotation. In order to induce an imbalance $C_{21}^{(1)}$ in an axial second- (or third-) order gradiometer, it is necessary to tilt at least two turns of the gradiometer such that a sensitivity to the $y-$ component of the magnetic field is created and to displace the turns in opposite directions along the $x-$ axis such that a baseline is formed. The baseline of the ”parasitic gradiometer” that corresponds to the imbalance $C_{21}^{(1)}$ is of the order of the manufacturing error. On the other hand, the baselines of the ”parasitic gradiometers” that correspond to the other first-order imbalance coefficients can be as large as the length of the gradiometer. For this reason, the imbalance $C_{21}^{(1)}$ is smaller than the other first-order imbalance coefficients. The same holds for the second-order imbalance $C_{321}^{(2)}$. Consequently, the reference channels that correspond to the imbalance coefficients $C_{21}^{(1)}$ and $C_{321}^{(2)}$ can be omitted from the measuring system.

By assuming that the maximum manufacturing error equals $0.1mm$, it is concluded from figure 3.3 that the maximum expected initial zero-, first- and second- order imbalance coefficients equal $2 \cdot 10^{-2}$, $1 \cdot 10^{-3}m$ and $1 \cdot 10^{-4}m^2$, respectively.

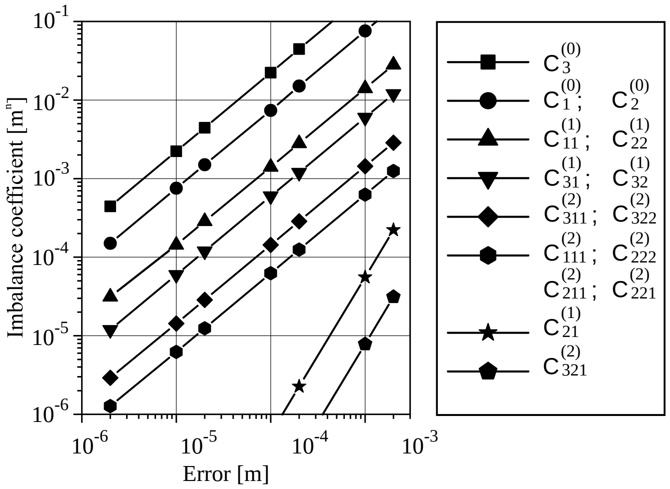

Figure 3.3. The maximum expected initial imbalance coefficients of the third-order gradiometer (figure 3.1a) due to geometrical imperfections as a function of the manufacturing error.

3.3.2 Imbalance induced by eddy currents

The eddy currents that are induced in the disk-shaped and cylindrical conductors by the magnetic fields that are listed in table 3.1, are calculated analytically as described in section 3.2.4. The eddy currents induced by magnetic fields $g_3^{(0)}\widehat{z}$ and $g_{321}^{(2)}\left(2yz\widehat{x}+2xz\widehat{y}+2xy\widehat{z}\right)$ (rows 3 and 13 in table 3.1) are shown in figure 3.4 as an example. All calculated eddy currents can be split in two groups. The first group comprises eddy currents that flow in concentric circular pathes (an example is shown in figure 3.4a). The second group comprises the rest of the eddy currents. The eddy currents that form the first group induce non-zero magnetic flux through the gradiometers. In opposite, the eddy currents of the second group induce zero net magnetic flux through the gradiometers. For instance, the eddy currents shown in figure 3.4b have several regions where currents are flowing in opposite directions producing zero net magnetic flux through a horizontal coaxial circular coil.

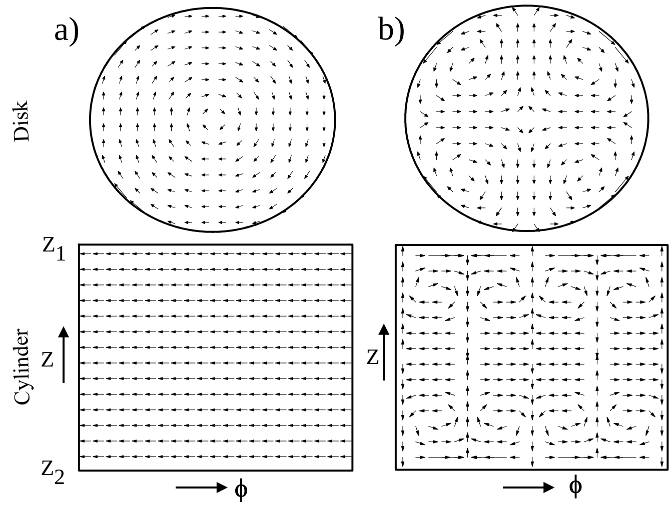

Figure 3.4. Examples of calculated eddy currents in the disk-shaped and cylindrical conductors. a) The applied test magnetic field is assumed to be in the form $g_3^{(0)}\widehat{z}$. b) The applied test magnetic field is assumed to be in the form $g_{231}^{(2)}\left(2yz\widehat{x}+2xz\widehat{y}+2xy\widehat{z}\right)$.

Table 3.2. Imbalances induced by eddy currents in the gradiometers at the frequency of $100Hz$

-	2^{nd} order grad.		3^{rd} order grad.	
Imbalance	disk	cyl	disk	cyl
$C_3^{(0)}$, $[-]$	$1 \cdot 10^{-3}$	$1 \cdot 10^{-3}$	$1 \cdot 10^{-3}$	$1 \cdot 10^{-3}$
$C_{11}^{(1)}$,$C_{22}^{(1)}$, $[m]$	$1 \cdot 10^{-4}$	$2 \cdot 10^{-4}$	$1 \cdot 10^{-4}$	$1 \cdot 10^{-4}$
$C_{311}^{(2)}$,$C_{223}^{(2)}$, $[m^2]$	-	-	$2 \cdot 10^{-5}$	$3 \cdot 10^{-5}$

The (non-zero) imbalance coefficients calculated for the second- and third- order gradiometers are summarized in table 3.2. As expected, the imbalance coefficients of those test magnetic fields that are related by a rotation around the $z-$ axis are equal because the gradiometer, the disk-shaped and the cylindrical conductors are invariant to this rotation. The imbalance coefficients $C_{21}^{(1)}$ and $C_{321}^{(2)}$ equal zero.

From table 3.2 it follows that the maximum expected values of the imbalance coefficients induced by the eddy currents in the gradiometers equal $2 \cdot 10^{-3}$, $2 \cdot 10^{-4}m$ and $5 \cdot 10^{-5}m^2$ for the zero-, first- and second- order imbalance, respectively.

3.3.3 Imbalances induced by the superconducting SQUID modules

In order to assess the accuracy of the FEM, the imbalance coefficients $C_1^{(0)}$, $C_2^{(0)}$ and $C_3^{(0)}$ of the third-order gradiometer due to a spherically shaped superconductor (figure 3.2a) are evaluated using both the FEM and analytical expressions for the magnetic field that are available in (Kochin *et al.*, 1964). The radius of the sphere is assumed to be equal to that of cylindrical SQUID module ($R_S = 5mm$). The results are presented in figure 3.5. The imbalance $C_1^{(0)}$ equals zero as the spherical superconductor is located on the $y-$ axis. The imbalance $C_1^{(0)}$ calculated using the FEM (see figure 3.5) reflects the magnitude of the numerical errors. From figure 3.5 it follows that the parameters of the FEM are adjusted well enough to calculate

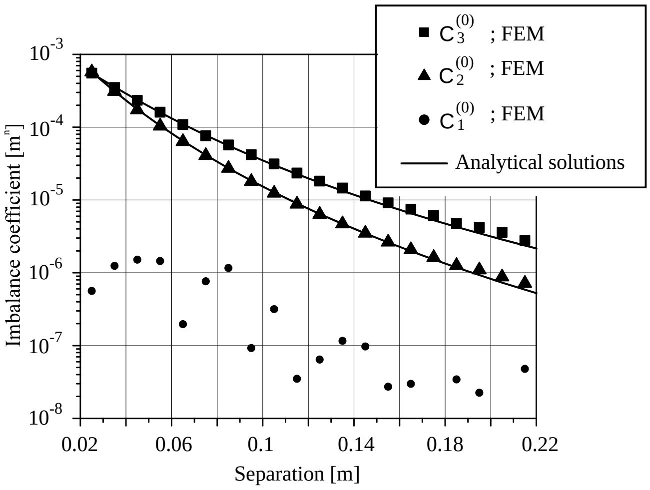

Figure 3.5. Imbalances of the symmetric third-order gradiometer due to a spherically-shaped superconductor (figure 3.2a) versus the separation between the top turn of the gradiometer and the superconductor. The solutions obtained using FEM as well as solutions obtained using the analytical expression for the scalar magnetic potential are shown.

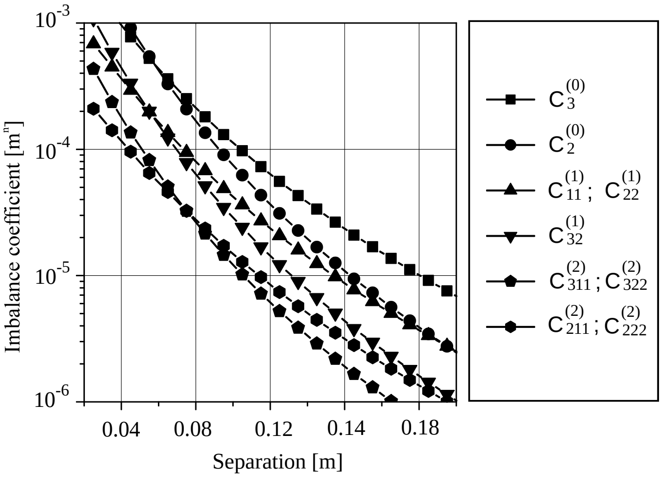

Figure 3.6. Imbalances of the symmetric third-order gradiometer due to a single cylindrically shaped SQUID module (figure 3.2b). Only non-zero imbalance coefficients are shown.

imbalance coefficients as small as 10^{-6} with adequate precision. Similar results are obtained for the second-order gradiometer.

The imbalance coefficients of the third-order gradiometer induced by a single cylindrical SQUID module are shown in figure 3.6. Similar to the case of the spherical superconductor, only the imbalance coefficients corresponding to test magnetic fields that have significant $y-$ or $z-$ components in the volume occupied by the SQUID module have a significant magnitude. The imbalance coefficients that have magnitudes of the order of the numerical errors of the FEM ($< 10^{-6}$, see figure 3.5) are not shown in figure 3.6.

The imbalance coefficients of the third-order gradiometer induced by twelve cylindrical SQUID modules (figure 3.2) are shown in figure 3.7. The separation between the top turn of the gradiometer and the twelve SQUID modules equals $0.201m$ in the FHARMON demonstrator. From figure 3.7, it follows that the expected zero-, first- and second- order imbalance coefficients induced by the SQUID modules of the FHARMON demonstrator equal 10^{-4}, $5 \cdot 10^{-5}m$ and $2 \cdot 10^{-5}m^2$, respectively.

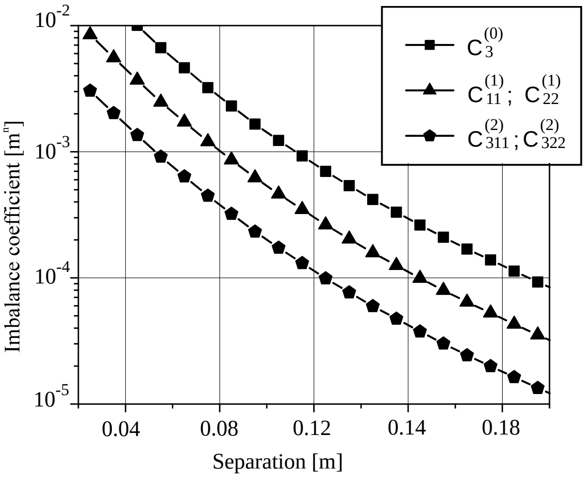

Figure 3.7. Imbalances of the symmetric third-order gradiometer due to twelve cylindrically shaped SQUID modules (figure 3.2c). Only non-zero imbalance coefficients are shown.

3.4 Conclusion

Methods are presented to evaluate imbalance coefficients of arbitrary shaped gradiometers due to (i) imperfections in geometry of the gradiometer, (ii) eddy currents induced in the radiofrequency interference shield, and (iii) the screening effect in the superconducting SQUID modules. The methods are applied to estimate the maximum expected imbalance coefficients of second- and third- order axial gradiometers of the FHARMON measuring system. Assuming a manufacturing accuracy of $0.1mm$ it was calculated that the maximum expected values of zero-, first- and second- order imbalance coefficients due to mechanical imperfections equal $2 \cdot 10^{-2}$, $10^{-3}m$ and $10^{-4}m^2$, respectively. The five largest imbalances are: $C_1^{(0)}, C_2^{(0)}, C_3^{(0)}, C_{11}^{(1)}, C_{22}^{(1)}$ (see figure 3.3). The imbalance coefficients induced by eddy currents equal $2 \cdot 10^{-3}$, $2 \cdot 10^{-4}m$, $5 \cdot 10^{-5}m^2$ and by screening currents 10^{-4}, $5 \cdot 10^{-5}m$, $2 \cdot 10^{-5}m^2$. It was concluded that mechanical imperfections are the main source of imbalance. Furthermore, it is found that the imbalance coefficients $C_{21}^{(1)}$ and $C_{321}^{(2)}$ are negligible in the axial symmetric second- and third- order gradiometers. Consequently, the corresponding reference channels can be omitted from the measuring system.

Chapter 4

Design of the characterization coil set

4.1 Introduction

As discussed in chapter 3, eight test magnetic fields are required for the balancing of the gradiometer designed in chapter 2. These test magnetic fields are listed in the first eight rows of table 3.1. In this chapter, the design of a characterization coil set that can produce the eight test magnetic fields is discussed. The coil set can establish a field uniformity of $25ppm$ in a volume occupied by the gradiometer, provided the construction is realized with $0.1mm$ accuracy.

The characterization coil set can be built using two types of magnetic-field and gradient coils (Turner, 1993): coils with discrete windings and coils with distributed windings (see figure 4.1). The well-known Helmholtz coil set is an example of a coil set with discrete windings (figure 4.1a). The two field-producing coils that form the Helmholtz set are located parallel to each other and have circular shape. The currents in the two coils flow in the same direction. This arrangement of currents eliminates all odd-order derivatives of the magnetic field in the center of the coil set. The separation between the coils and the radii of the coils are chosen such that the second-order derivatives of the magnetic field also vanish. Consequently, the homogeneity of the magnetic field in axial direction improves. This approach to coil design can be generalized: firstly, the directions of the currents in the coils are defined to produce the desired magnetic field profile, and secondly, the geometry parameters of the coils are chosen such, that particular terms of the series expansion of the magnetic field are eliminated homogenizing the magnetic field profile. This general approach is used to design square coil sets for generating uniform magnetic fields (Merritt *et al.*, 1993; Rubens, 1945), a Maxwell coil set for generating first-order longitudinal gradients, trapezoidal coils for generating first-order transversal gradients (Bangert and Mansfield, 1982), and shim coils for generating various magnetic-field gradients (Anderson, 1961).

A number of techniques for designing distributed-winding coils has been reported in literature (Morrone, 1998), (Fisher *et al.*, 1997), (Turner, 1986). The majority of these techniques consists of two steps. In the first step, a continuous current

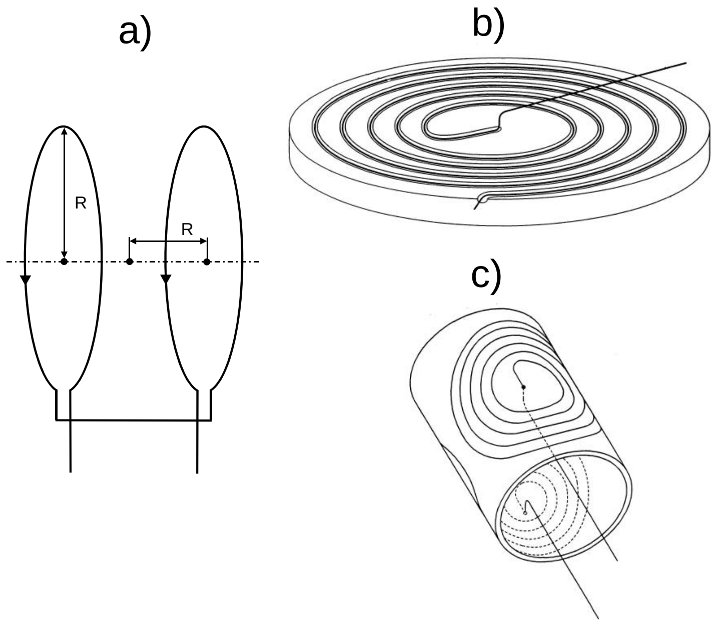

Figure 4.1. a) An example of coils with discrete windings: the Helmholtz coil set. b,c) Examples of distributed windings coils. A distributed winding coil approximates a two dimensional current density. The current density is designed to generate a specific profile of magnetic field.

density is computed to generate the required magnetic-field profile. Similar to discrete-winding coils, the current density is designed to zero particular terms of a series expansion of the magnetic field shaping its profile (Morrone, 1998). In the target field approach (Turner, 1986), the continuous current density is found by calculating a spatial Fourier Transform of the specific magnetic-field profile. In the second step, the continuous current density is approximated by a set of distributed windings connected in series. As an alternative to this two-step design procedure, the distributed windings can be assumed to have a predetermined shape and their geometrical parameters and positions can be calculated using a genetic optimization procedure (Fisher *et al.*, 1997).

A sketch of the coil set is given in figure 4.2. The distributed winding coils are made by etching square printed circuit boards (PCBs) that have outer dimensions of $0.5m \times 0.5m$. The PCBs are positioned in layers around the origin. Each layer comprises four or eight PCB coils. Each set of two layers that are located equidistantly from the origin is used to produce one or two magnetic fields. The construction requires 64 PCB coils that share eight different etching patterns. On average, one magnetic field profile requires eight PCBs. Both, the width of the coil set as well as its length are $1.5m$ (see figure 4.2). These dimensions are limited by the maximal size of PCBs readily available from PCB manufacturers. The height of the coil set measures $2m$ and is limited by the height of the ceiling in the laboratory.

In this chapter, the basis vectors are denoted as $\widehat{e_1}$, $\widehat{e_2}$, and $\widehat{e_3}$. The corresponding coordinates will be indicated as a_1, a_2, and a_3, respectively.

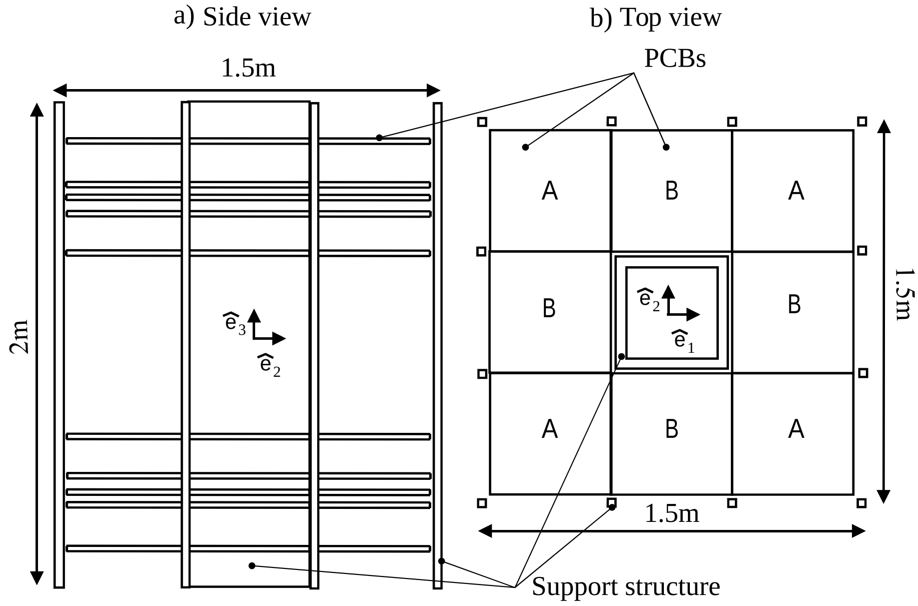

Figure 4.2. Schematic drawing of the characterization coil set. Distributed-winding coils are made by etching square printed circuit boards (PCBs). The PCBs are organized around the origin in ten layers. Pairs of layers that are located symmetrically in relation to the origin are used to produce one or two magnetic-field profiles. The locations of the PCBs within a layer are labeled by A and B (see top view).

4.2 Requirements for the coil set

4.2.1 Required homogeneity of test magnetic fields

Inhomogeneity of the test magnetic fields causes errors in measured imbalance coefficients affecting the outcome of the balancing procedure. In this subsection, the homogeneity that is required to balance the FHARMON system gradiometer is estimated. In chapter 3 it was concluded that mechanical imperfections are the main source of imbalance. In this section, it is presumed that the gradiometer is only affected by the imbalances due to mechanical imperfections of the gradiometer. The possible eddy and screening current effects are neglected. For the purpose of this investigation the inhomogeneity of B_0 in a volume V is defined as

$$H^{(n)} \equiv \max \left| \frac{B_r - B_i}{B_r} \right| \tag{4.1}$$

where B_r and B_i are the values of B_0 measured at the location of the corresponding reference channels and the $i-th$ point in the volume V, respectively. In order to measure an imbalance coefficient accurately, the maximum allowed inhomogeneity has to satisfy the following condition:

$$H^{(n)} \leq \frac{C_Q^{(n)}}{C_I^{(n)}} \tag{4.2}$$

where $C_I^{(n)}$ and $C_Q^{(n)}$ are the initial and required imbalance coefficients (that is, before and after balancing, respectively). The required imbalance coefficients of the third-order gradiometer $C_Q^{(0)} = 5 \cdot 10^{-7}$, $C_Q^{(1)} = 6 \cdot 10^{-6} m$ are calculated using equations presented in (Vrba, 1996) and assuming a system noise of $1 fT \cdot Hz^{-1/2}$. The maximum expected initial imbalance coefficients due to imperfections in the geometry of the third-order gradiometer are evaluated in chapter 3 as $C_I^{(0)} = 2 \cdot 10^{-2}$, $C_I^{(1)} = 1 \cdot 10^{-3} m$. Consequently, the inhomogeneity limits are expressed as

$$H^{(0)} \leq 2.5 \cdot 10^{-5}; H^{(1)} \leq 6 \cdot 10^{-3} \tag{4.3}$$

where $H^{(0)}$ and $H^{(1)}$ are the inhomogeneities of the uniform magnetic fields and the first- order gradients, respectively.

A gradiometer is sensitive to higher-order gradients of the magnetic field. For the sake of simplicity, it is assumed that a third-order gradiometer is only sensitive to the third- order gradient. Therefore when detecting the $n-th$ order imbalance (with $n = 0$ or $n = 1$), the signal due to the third-order gradient should be smaller than the $n-th$ order imbalance signal

$$g^{(n)} C_Q^{(n)} \geq g^{(3)} C^{(3)} \tag{4.4}$$

where g denotes the magnetic-field gradient. However, the last requirement can be relaxed if the signal due to the ideal gradiometer can be predicted by measuring third-order longitudinal gradient of the test magnetic field. That is, the deviation of the measured signal from the calculated one can be used for imbalance evaluation.

4.2.2 Required coil factor

The term coil factor is defined as the magnitude of a magnetic field or a gradient per unit of current in the coil set. As discussed in the following sections, the homogeneity of the test magnetic fields is increased by cancelling higher-order spatial gradients. This cancellation is achieved by arranging the turns of the coils such, that different fractions of the coil carry currents in opposite directions. This, however, decreases the coil factor. For this reason, a trade-off has to be made between the homogeneity and the coil factor. Thus, it is necessary to estimate the minimal allowed coil factor since in that case maximum uniformity of test magnetic fields is achieved. Assuming the intrinsic noise of the measuring system of $1 fT \cdot Hz^{-1/2}$, a detection time of $120 sec$ and a desired signal-to-noise ratio of 10 minimum allowed coil factors are estimated as $0.1 \frac{\mu T}{A}$ and $0.1 \frac{\mu T}{A \cdot m}$ for zero- and first- order gradients, respectively. In the design, an additional factor of 10 in these coil factors is assumed as a margin of safety.

Table 4.1. Possible symmetrical arrangements of the current density.

	$J_1(a_1)^*$	$J_1(a_2)^*$	$J_1(a_3)$, $J_2(a_3)$	non-zero linearly independent gradients
1	E	O	E	$g_3^{(0)}$, $g_{311}^{(2)}$, $g_{322}^{(2)}$
2	O	O	E	$g_{32}^{(1)}$, $g_{3211}^{(3)}$, $g_{3222}^{(3)}$
3	E	E	E	$g_{31}^{(1)}$, $g_{3111}^{(3)}$, $g_{3221}^{(3)}$
4	O	E	E	$g_{321}^{(2)}$
5	E	O	O	$g_{11}^{(1)}$, $g_{22}^{(1)}$, $g_{1111}^{(3)}$, $g_{2211}^{(3)}$, $g_{2222}^{(3)}$
6	O	O	O	$g_2^{(0)}$, $g_{211}^{(0)}$, $g_{222}^{(0)}$
7	E	E	O	$g_1^{(0)}$, $g_{111}^{(0)}$, $g_{221}^{(0)}$
8	O	E	O	$g_{21}^{(1)}$, $g_{2111}^{(3)}$, $g_{2221}^{(3)}$

* symmetry of J_2 is opposite to that of J_1
E:even; O: odd.

4.3 Design

4.3.1 Symmetry of current density

A vector field is considered to be symmetric if all its components have even ($f(x) = f(-x)$) or odd ($f(x) = -f(-x)$) symmetry with respect to all spatial coordinates. All required magnetic fields are symmetric. Presumably, the current densities that produce symmetric magnetic fields have to be symmetric as well. In this section, the possible symmetric configurations of current density and the corresponding magnetic-field profiles are discussed.

The source current density that produces one of the test magnetic fields is assumed to be confined to two parallel planes that are located perpendicular to the a_3- axis at equal distances from the origin. The current density has two components J_1 and J_2 in the a_1 and a_2 directions, respectively. Each component is a function of the three spatial coordinates a_1, a_2, a_3 which can be either even or odd with respect to a spatial coordinate. Because, the charge has to be conserved in each plane ($\overrightarrow{\nabla} \cdot \overrightarrow{J} = 0$) the following holds:

$$\frac{\partial J_1}{\partial a_1} = -\frac{\partial J_2}{\partial a_2} \tag{4.5}$$

According to the last equation, the two components of the current density need to have opposite symmetries with respect to coordinates a_1 and a_2. This reduces the number of possible ways to configure the current density symmetrically around the origin to eight. The possible symmetric configurations of the current density are numbered as shown in table 4.1. In the table, the even and odd symmetries are denoted by "E" and "O", respectively.

The magnetic field $\overrightarrow{B}$ produced by the current density $\overrightarrow{J}$ is described by the Biot-Savart law

$$\overrightarrow{B}(\overrightarrow{r}) = \frac{\mu_0}{4\pi}\int \frac{\overrightarrow{J}(\overrightarrow{r}') \times (\overrightarrow{r} - \overrightarrow{r}')}{|\overrightarrow{r} - \overrightarrow{r}'|^3} dV' \tag{4.6}$$

where $\overrightarrow{r} = (a_1, a_2, a_3)$ gives the point in space where the magnetic field is calculated; $\overrightarrow{r}' = (a'_1, a'_2, a'_3)$ gives the coordinates of the source-current density; V' denotes the volume occupied by the source-current density. By substituting (4.6) in (3.1) the magnetic field gradients are expressed in the following form:

$$g^{(n)}_{k_0 \ldots k_n} = \int\int J_1 P^{(n)}_{k_0 \ldots k_n} da'_1 da'_2 + \int\int J_2 T^{(n)}_{k_0 \ldots k_n} da'_1 da'_2 \tag{4.7}$$

where $J_1 P^{(n)}_{k_0 \ldots k_n}$ and $J_2 T^{(n)}_{k_0 \ldots k_n}$ are symmetric functions. Note, that information on the symmetry of the current density with respect to the a_3- coordinate is embedded in the functions $P^{(n)}_{k_0 \ldots k_n}$ and $T^{(n)}_{k_0 \ldots k_n}$. Integration of an odd function over a symmetric interval yields zero. The type of symmetry (either even or odd) of the functions under the integrals in the last equation is analyzed by a computer for the eight possible symmetries of the current density and linearly independent gradients of order $n \leq 10$. Table 4.1 lists the non-zero linearly independent gradients of order $n \leq 3$. From these results the following conclusions are drawn:

1) All required test magnetic fields (see the first eight columns in table 3.1) can be generated by the planar configuration of the current density. The uniform magnetic fields in the three orthogonal directions can be produced by configuring the current density as indicated in rows $1, 6$ and 7 of table 4.1. Similarly, the transversal first-order gradients can be produced by configuring the current density as indicated in rows $2, 3$ and 8 of table 4.1. The symmetry number 5 can be used to generate the longitudinal gradients. However, all coils for generating longitudinal gradients in the form given in the first and seventh columns of table 3.1 that were possible to design have a relatively low homogeneity. Instead, coils are configured to generate the following linear combinations of longitudinal first-order gradients:

$$\begin{aligned} \overrightarrow{B}^{(1)}_{11} - \overrightarrow{B}^{(1)}_{22} &= B_0\left(a_1\hat{e}_1 - a_2\hat{e}_2\right) \\ \overrightarrow{B}^{(1)}_{11} + \overrightarrow{B}^{(1)}_{22} &= B_0\left(a_1\hat{e}_1 + a_2\hat{e}_2 - 2a_3\hat{e}_3\right); \end{aligned} \tag{4.8}$$

2) The majority of the interfering higher-order gradients is cancelled by symmetric configurations of the current density around the origin. In order to homogenize the test magnetic fields even further, the higher-order gradients have to be cancelled by designing a specific pattern of the current density in a single octant. There is no need to consider the current density in all eight octants as these are determined by symmetry. The higher-order gradients that need to be cancelled ($n \geq 2$) are linear combinations of the non-zero linear independent gradients (see the fifth column of the table 4.1 for the non-zero linearly independent gradients of order $n \leq 3$).

3) All symmetric configurations of the current density do not produce longitudinal higher-order gradients, save for configurations number 1 and 5. Thus, in most cases,

longitudinal higher-order gradients appear due to asymmetry of current density. Thus, the validity of condition given in (4.4) is defined by misalignment of the PCB coils and evaluated by Monte Carlo simulations.
4) It is beneficial to design etching patterns of the PCBs such, that the current density pattern in each layer does not change after 90^o rotation around the a_3- axis. This is an obvious choice for symmetries number $2, 3, 6, 7$ as it allows to reduce the amount of PCBs in positions A (see figure 4.2) by a factor of 2. In the case of the symmetry number 5 it is a necessary choice as the magnitudes of the gradients $g_{11}^{(1)}$ and $g_{22}^{(1)}$ have to be equal (see (4.8)). In the case of the symmetries number 1, 5 and 8 this choice reduces the amount of the linearly independent gradients to be considered. For instance, in the case of symmetry nr. 1 the interfering gradients $g_{311}^{(2)}$ and $g_{322}^{(2)}$ are equal in magnitude (as their indexes are related by swapping 1 and 2) if the current density is invariant to the rotation. Thus, all second-order gradients in symmetry number 1 can be described by a single gradient $g_{311}^{(2)}$ which reduces the computational burden. Moreover, the J_1 and J_2 components of the current density contribute equally to the gradient $g_{311}^{(2)}$ if the current density pattern does not change after the rotation.
If symmetry holds, any pattern of current density on the surface of the PCB can be used to generate the required test magnetic fields. For instance, two layers containing sixteen identical coils can be used to generate all eight required test magnetic fields. However, the homogeneities of these magnetic fields will not satisfy the requirements discussed in section 4.2.1. In order to meet the homogeneity requirements the total set is split into five independent coil sets that are dedicated to one or two test magnetic fields. As discussed in section 4.3.3, the current densities on the surfaces of the PCBs are optimized in order to increase the homogeneity.

4.3.2 Configurations of the PCBs

The PCB coils can be located: (*i*) in position A, (*ii*) in position B, or (*iii*) in both positions A and B (see figure 4.2). First, the coils for these three configurations are designed using the procedure discussed in the following sections. Second, the configurations that provide magnetic fields with sufficient homogeneities and coil factors with a minimal amount of PCBs are selected. The resultant configurations are discussed below:
1) The first coil set produces the uniform magnetic field in the a_3- direction. A single layer of this coil set is shown in figure 4.3a. The currents in the PCBs of the second layer of this coil set flow in the same direction.
2) The second coil set produces a transversal gradient of the form $a_1\hat{e}_2 + a_2\hat{e}_1$. A single layer of this coil set is shown in figure 4.3b. The currents in the PCBs of the second layer of this coil set flow in opposite direction.
3) The third coil set can produce uniform magnetic fields in the a_1- and a_2- directions. A single layer of this coil set consists of eight PCBs of which six are used to generate a uniform magnetic field in the a_1- direction (figure 4.3c) and six for the uniform magnetic field in the a_2- direction (figure 4.3d). In both cases, the PCBs in position A are the same. Currents in the PCBs of the second layer of this coil set

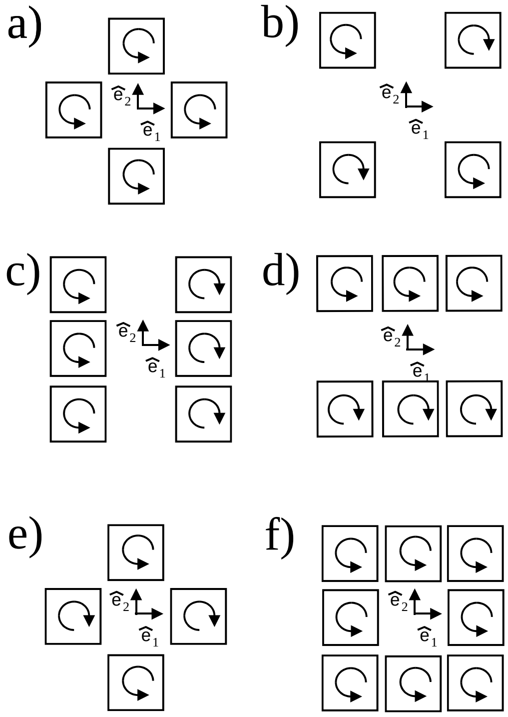

Figure 4.3. Configurations of PCBs that are used to generate the test magnetic-field profiles: a) $B_0\hat{e}_3$; b) $B_0\,(a_1\hat{e}_2 + a_2\hat{e}_1)$ c) $B_0\hat{e}_1$ or $B_0\,(a_3\hat{e}_1 + a_1\hat{e}_3)$(depends on the direction of the current flow in the corresponding layer), d) $B_0\hat{e}_2$ or $B_0\,(a_3\hat{e}_2 + a_2\hat{e}_3)$; e) $B_0\,(a_1\hat{e}_1 - a_2\hat{e}_2)$, f) $B_0\,(a_1\hat{e}_1 + a_2\hat{e}_2 - 2a_3\hat{e}_3;)$. Arrows on the PCBs represent the direction of current flow. Only the PCB coils in the upper half-space are shown. The arrangement of the PCB coils in the lower half-space is the same. The direction of the current flow in the PCB coils in the lower half-space is the same or opposite to that of the PBC coils in the upper half-space.

flow in opposite directions.

4) The fourth coil set produces transversal gradients of the form $a_3\hat{e_1} + a_1\hat{e_3}$ and $a_3\hat{e_2} + a_2\hat{e_3}$. The configurations of the PCBs in one layer are the same as that of the third coil set (figure 4.3c and d), but placed in a different axial position. The currents in both layers of the fourth coil set flow in the same direction.

5) The fifth coil set produces longitudinal gradients of the form $a_1\hat{e}_1 - a_2\hat{e}_2$ and $a_1\hat{e}_1 + a_2\hat{e}_2 - 2a_3\hat{e}_3$. The configurations of the PCBs and the current flows are shown in figure 4.3e and f, respectively. The same PCBs in positions B are used in both configurations. The currents in the PCBs of the second layer of this coil set flow in directions opposite to those shown in figure 4.3e and f.

4.3.3 Current density on a single PCB

The current density on a single PCB is assumed to curl around a "curl point" with coordinates $[C_1, C_2]$ following rectangular pathes (figure 4.4). The curl point is located on the line L which is an axis of symmetry and has different orientation on the PCBs in positions A and B (see figure 4.2). The exact location of the curl point on the line L is subject to optimization. The lines that interconnect the curl point and the corners of a PCB divide the PCB into four regions. The regions are labelled by digits from 1 to 4. Each region is divided into 25 strips that are parallel to the boundaries of the PCB. The current density is assumed to be homogeneous within each strip but its

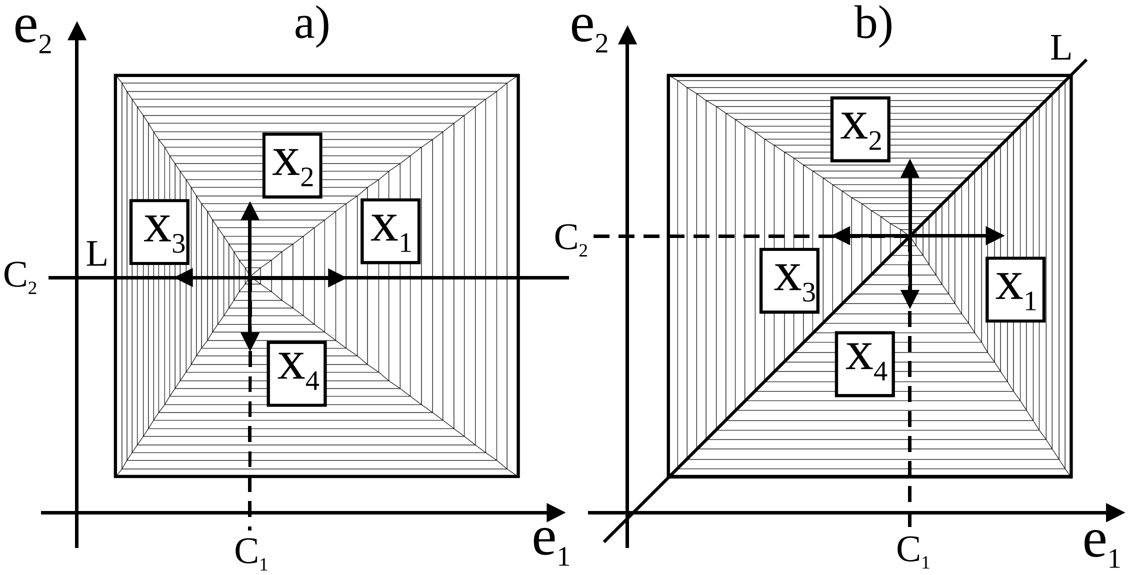

Figure 4.4. The surface of each PCB is partitioned in 100 strips. The current in each strip flows in the direction parallel to the edges of the PCB. All currents in the PCBs curl around a point with coordinates (C_1, C_2). a) A PCB to be installed in position B. b) A PCB to be installed in position A. The point (C_1, C_2) is restricted to the axis of symmetry (line L) in both cases. Digits 1 to 4 number the triangular-shaped regions of the PCB.

magnitude varies from strip to strip. The current density must be continuous across the borders of the regions.

The current density in the first region is described by $J_1(x_1)$ where x_1 is the coordinate axis that ranges from zero at the curl point to the maximum value at the boundary of the PCB. When the current density $J_1(x_1)$ is known, the current densities in other regions can be calculated as

$$J_i(x_i) = A_i \cdot J_1 \left(k_i \cdot x_i\right) \tag{4.9}$$

where A_i and k_i are scaling factors that can be deduced from the position of the curl point (see figure 4.4); $i = 2, 3, 4$ indexes the regions. Thus, the task of specifying a two-dimensional current density is reduced to specifying a single one-dimensional scalar function $J_1(x_1)$.

Next, the optimization procedure for the four-PCBs configurations (e.g. figure 4.3a) is discussed. The optimization of the eight-PBCs configurations (e.g. figure 4.3c and d) is similar. An equation for the magnetic field produced by the trapezoidal strip carrying a uniform current density is available in (Pissanetzky and Xiang, 1990). By differentiating this equation, expressions for non-zero linearly independent gradients are obtained. These expressions are evaluated numerically to find the magnitudes of an ith linearly independent gradient produced by the jth strip carrying a unitary current density in the first $(f_{i,j})$ and the third $(t_{i,j})$ regions, respectively. For symmetry reasons discussed in section 4.3.1 the strips that carry current in directions parallel to the a_1-direction in the second and fourth regions are excluded from the calculation. Only the fractions of the strips that are located in the first octant are considered. The linearly independent gradients produced by the fraction of PCBs that are located in the first octant are expressed as

$$\overrightarrow{g} = \mathbf{M} \cdot \overrightarrow{j} \tag{4.10}$$

where $\overrightarrow{g}$ is a vector composed of linearly independent gradients; $\overrightarrow{j}$ is a vector composed of magnitudes of the current densities in individual strips in the first region; $\mathbf{M}$ is a matrix with entries $m_{i,j} = f_{i,j} + A_3 \cdot t_{i,j}$. The current densities in the strips of the first region are found by applying the pseudoinverse $\mathbf{M}^+$

$$\overrightarrow{j} = \mathbf{M}^+ \overrightarrow{g}_d \tag{4.11}$$

where $\overrightarrow{g}_d$ is a vector which reflects a desired gradient composition of the magnetic field. The element of the vector $\overrightarrow{g}_d$ which corresponds to the target magnetic field (gradient) equals one. The other elements equal zero. The system of linear equations (4.10) is underdetermined. Thus, the solution (4.11) obtained by means of the pseudoinverse stands for the minimum-norm solution, which in general provides the maximum coil factor for a desired gradient composition of the magnetic field (i.e. minimal current magnitude for the same field strength). By varying the specific gradients represented in (4.10) and (4.11), a trade-off is made between coil factor and inhomogeneity.

The optimal location of the curl point and the separation between the layers are found by varying these two parameters independently within geometrically acceptable limits. The solutions that provide the best homogeneity (inhomogeneity typically of the order of 10^{-5}) for the sufficient coil factor of $1\frac{\mu T}{A}$ and $1\frac{\mu T}{A \cdot m}$ are selected. The inhomogeneity is calculated within a cylindrical volume that can contain the third-order gradiometer of the FHARMON system. The radius and the height of the cylindrical volume measure 25mm and 225mm, respectively.

4.3.4 Approximation of the current density by discrete windings

The two-dimensional current density in the design is defined by a single one-dimensional scalar function $J_1(x_1)$. Thus, it is sufficient to define coordinates of discrete windings in the first region along the x_1-axis. The coordinates of the windings along the x_i-axis in other regions are calculated by employing the scaling coefficients k_i (see (4.9)). First, a so-called stream function is calculated in the first region as

$$U_1(x_1) = \int J_1(x)dx. \tag{4.12}$$

Second, a grid with uniformly distributed nodes on the U_1-axis is defined (see figure 4.5). The projection of the grid on the x_1-axis (dashed lines in figure 4.5) via the $U_1(x_1)$ curve defines the coordinates of the discrete windings. The offset of the grid in relation to the x_1-axis is adjusted to find the best fit of the magnetic field produced by

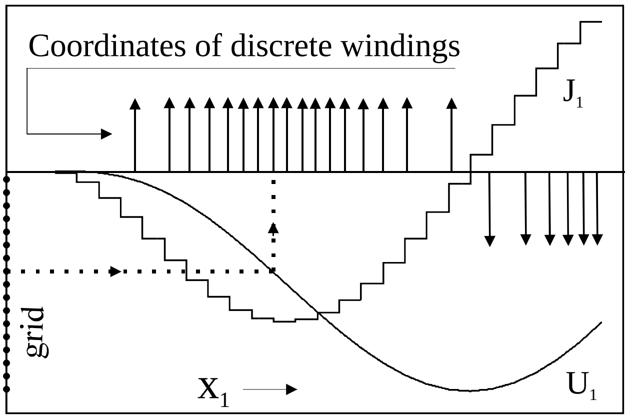

Figure 4.5. Approximation of a current density J_1 by discrete windings. Integration of J_1 results in U_1. A grid with equally distributed nodes is projected on the x_1-axis via the U_1 curve. The projections indicated by the arrows shows the coordinates of the discrete windings.

the distributed winding coils to that produced by the corresponding two-dimensional current density.

An example of the PCB etching pattern is shown in figure 4.6. The PCBs with this etching pattern are to be installed in position B of the coil set that produces uniform magnetic fields in the a_1 and a_2 directions. The distributed windings are combined in four clusters. The direction of the current in neighboring clusters is opposite. The crossing line links individual windings. Each PCB is etched on both sides. The etching patterns on the two sides are related by mirroring (see figures 4.6 b,c). A feed-through connects the two individual coils on the two sides of the PCB in series such that the coils carry currents in the same direction. The currents in the lines that interconnect the individual windings on the two layers of the PCB flow in opposite directions. The width of the copper strips and the minimal separation between the strips equal $200\mu m$. The main parameters of the coil set are presented in table 4.2. The inhomogeneity in table 4.2 is calculated employing (4.1).

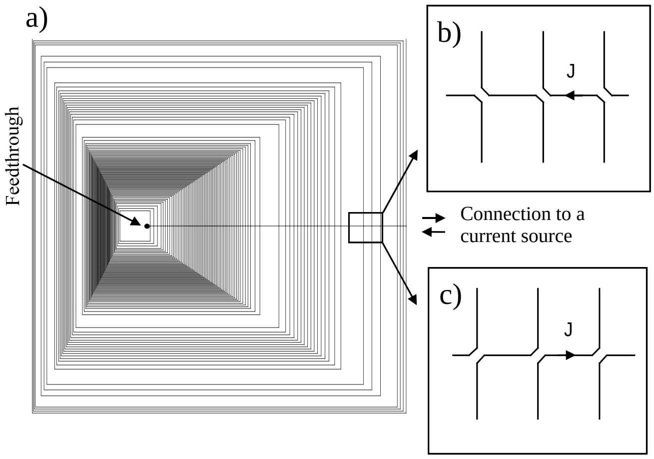

Figure 4.6. a) An example of an etching pattern of a PCB. The crossing line interconnects the individual windings. The two sides of the PCB have etching patterns that are related by mirroring. b) Detailed view of the interconnections between the individual windings on the top surface of the PCB. c) Detailed view of the interconnections between the individual windings on the bottom surface of the PCB.

Table 4.2. The main parameters of the characterization coil set. Manufacturing errors are neglected.

Field	Separation $[m]$	Coil factor $[\mu T/A]$, $[\mu T/(A \cdot m)]$	Inhomogeneity
$\overrightarrow{B}_1^{(0)}$, $\overrightarrow{B}_2^{(0)}$	1.08	2.6	$4.1 \cdot 10^{-6}$
$\overrightarrow{B}_3^{(0)}$	1.682	2.8	$4 \cdot 10^{-6}$
$\overrightarrow{B}_{21}^{(1)}$	1.24	2.3	$7.9 \cdot 10^{-6}$
$\overrightarrow{B}_{31}^{(1)}$, $\overrightarrow{B}_{32}^{(1)}$	1.32	1.4	$1.1 \cdot 10^{-5}$
$\overrightarrow{B}_{11}^{(1)} - \overrightarrow{B}_{22}^{(1)}$	0.756	1.6	$4 \cdot 10^{-5}$
$\overrightarrow{B}_{11}^{(1)} + \overrightarrow{B}_{22}^{(1)}$	0.756	1.6	$1.9 \cdot 10^{-5}$

4.4 Effect of misalignment of the setup

In this section, the dependence of the homogeneity of the test magnetic fields on the misalignment of the PCB coils is assessed by means of Monte Carlo simulations. A model of the coil set is made where each PCB is represented by its etching pattern. To simplify the computation, the copper strips that form the PCB etching patterns are modelled by infinitely-thin line conductors. An equation for the magnetic field produced by an infinitely-thin finite-length line conductor is available in (Ditterich and Eggert, 2001). In each run of the Monte Carlo simulations the position $\overrightarrow{a}_j$ of the jth PCB is modified according to

$$\overrightarrow{a}_j = (\overrightarrow{a}_j)_0 + \overrightarrow{\delta}_j \tag{4.13}$$

where $(\overrightarrow{a}_j)_0$ is the design value of the position and the components of $\overrightarrow{\delta}_j$ are zero-mean normally distributed random variables. The standard deviation of the components of $\overrightarrow{\delta}_j$ varies between $10\mu m$ and $1000\mu m$. In what follows, the standard deviation of these components is referred to as the manufacturing tolerance or simply the tolerance.

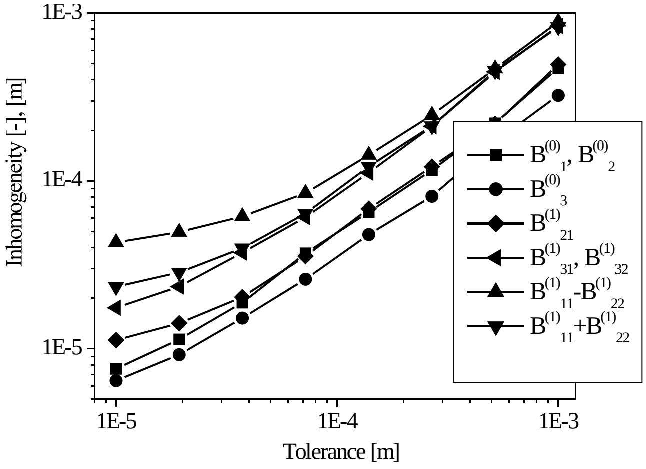

Figure 4.7. Expected inhomogeneity of the test magnetic fields produced by the coil set as a function of tolerance. The required inhomogeneity is given in (4.3). The symbols represent the calculated values; the lines are linear interpolations.

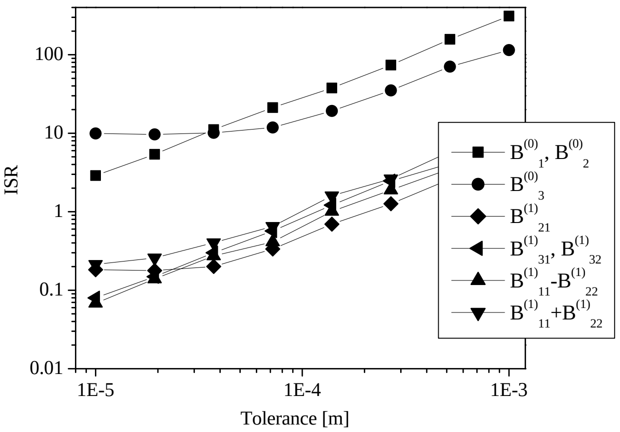

Figure 4.8. Expected interference-to-signal ratio (ISR). The interference is the net magnetic flux through the ideal third-order gradiometer; signal is the magnetic flux due to required (minimal) imbalance coefficient. The values of ISR less than one are considered to be acceptable.

In the simulations related to the evaluation of the inhomogeneity requirements (4.3), the gradiometer is represented by a set of 120 points on the surface of the cylinder with a height of $225mm$ and a radius of $0.025m$. The inhomogeneity on the surface of the cylinder is calculated by employing (4.1). Here, the parameter B_r in (4.1) is interpreted as the magnitude of the magnetic field or gradient in the origin. The inhomogeneity inside the cylinder is expected to be less than that on the boundary of the cylinder as the magnetic fields and the first order gradients are harmonic functions. Subsequently, the values of inhomogeneity on the surface of the cylinder that correspond to different runs of the Monte Carlo simulations are averaged. The result is shown in figure 4.7 as a function of the tolerance. From figure 4.7 it follows that the coil set produces first- order gradients with an inhomogeneity that is better than required $6 \cdot 10^{-3}$ (see(4.3)) even if the coil set is assembled with a tolerance of 1mm. However, in order to achieve the required inhomogeneity of the uniform magnetic fields (i.e. $2.5 \cdot 10^{-5}$), a tolerance better than $0.1mm$ is necessary.

The condition given in (4.4) is assessed by calculating an interference-to-signal ratio (ISR). The net magnetic flux through the third- order ideal gradiometer is interpreted as interference. The magnetic flux due to the required (minimal, after balancing) imbalance coefficient is interpreted as signal. Values of the ISR that are less than one are considered to be acceptable. The averaged ISR calculated for the third- order gradiometer are shown in figure 4.8. From figure 4.8 one can conclude that the tolerance of $0.1mm$ is sufficient for the first- order gradients. However, in the case of the uniform magnetic fields, the ISR is expected to be $10-20$ times higher than acceptable even if the coil set is assembled with a tolerance of $0.1mm$. Consequently, the corresponding magnetic flux imbalance coefficients can be balanced to the level of $5 \cdot 10^{-6} - 10^{-5}$. However, as discussed in section 4.2.1 the imbalance coefficients can be reduced to the required level of $5 \cdot 10^{-7}$ if the net magnetic flux through the ideal gradiometer is predicted with a relative error of $5\% - 10\%$ by measuring the spatial distributions of the uniform magnetic fields.

4.5 Conclusion

A compact set of planar coils for generating high-uniformity zero- and first- order gradients is designed. The coil set is composed of 64 distributed windings coils that are manufactured by etching printed circuit boards (PCBs) with outer dimensions of $0.5m \times 0.5m$. The outer dimensions of the coil set are $1.5m \times 1.5m \times 2m$. Assembled without manufacturing errors, the coil set generates zero- and first- order gradients with inhomogeneity of order of 10^{-5} in a cylindrical volume with a radius of $25mm$ and height of $225mm$. The results of Monte Carlo simulations suggest that the coil set needs to be assembled with a tolerance of $0.1mm$.

Optimization of the homogeneity of the test magnetic fields is performed by cancelling the higher-order interfering gradients of magnetic fields. The cancellation is achieved by configuring the PCB coils such that different fractions of the coils carry currents in opposite directions. An obvious drawback of this approach is a relatively low (though still sufficient) coil factor of the coil set. Alternative approaches to increase the homogeneity of the test magnetic fields would require an increase of the dimensions of the coil set or an increase of the amount of coils (see (Merritt *et al.*, 1993) for an example of such an approach).

Chapter 5

Gradiometer balancing

5.1 Introduction

This chapter describes the experiments that aim at balancing of the third-order gradiometer of the FHARMON system by means of the characterization coil set. The designs of the gradiometer and the characterization coil set are described in chapters 2 and 4, respectively. The outcome of the gradiometer balancing is a set of filters in the reference channels (denoted as $F_1 ... F_8$ in figure 1.9) which ensures a zero response of the gradiometer to all applied test magnetic fields.

The simulations described in chapter 3 suggest that the five largest expected imbalance coefficients of the FHARMON system gradiometer are: $C_1^{(0)}, C_2^{(0)}, C_3^{(0)}, C_{11}^{(1)}, C_{22}^{(1)}$ (see figure 3.3). For this reason, the characterization coil set was equipped with the three layers of PCB coils to enable five test magnetic fields that correspond to the five largest expected imbalance coefficients: $B_0\widehat{x}$, $B_0\widehat{y}$, $B_0\widehat{z}$, $B_0\left(x\hat{x} - y\hat{y}\right)$, $B_0\left(x\hat{x} + y\hat{y} - 2z\hat{z}\right)$. Accordingly, the gradiometer of the FHARMON system was equipped with five corresponding reference channels: $B_x, B_y, B_z, dBx/dx, dBy/dy$.

The accuracy of the gradiometer balancing appeared to be limited by two main factors:

- Inhomogeneity of the test magnetic fields,
- Drift of the flux-to-voltage transfers of the setup.

The requirements for the homogeneity of the test magnetic fields are discussed in chapter 4. The results of the Monte Carlo simulations suggest that the characterization coil set needs to be assembled with a tolerance of $0.1mm$ in order to achieve adequate homogeneity of the test magnetic fields. For this reason, special attention has been paid to the accuracy of the positioning of the PCB coils during design and manufacturing of the coil support. The mechanical construction of the characterization coil set is discussed in section 5.2. In order to assess the accuracy with which the characterization coil set was implemented, the homogeneities of the three uniform test magnetic fields generated by the coil set were measured by means of a fluxgate magnetometer. The construction of the fluxgate-magnetometer based setup and the

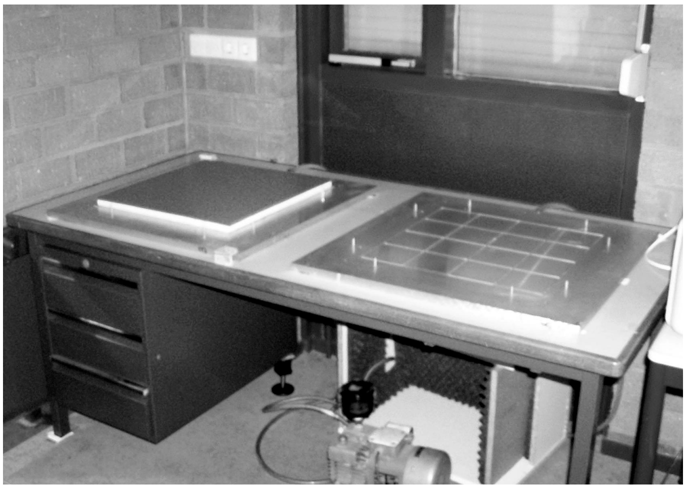

Figure 5.1. Apparatus for PCB coils reinforcement. The grooves on the aluminum plate are connected to an air pump. A PCB coil is sucked against the aluminium plate. A piece of foam material is glued between the coil and a dummy PCB. The coil remains sucked against the aluminum plate until the glue is hardened. Two aluminum plates were used simultaneously to speed up the gluing process.

homogeneity measurements are described in section 5.3. Measurements of the initial imbalance coefficients as well as the gradiometer balancing experiments are described in section 5.4.

The drift of the flux-to-voltage transfer of the SQUID-based setup deteriorates the accuracy of balancing. In general, the flux-to-voltage transfer of the setup can have a significant drift within the timeframe of the balancing experiment. In the balancing experiments discussed in this chapter, the drift of the flux-to-voltage transfer of the setup was monitored in situ during the balancing experiments. The measured drift, which is the major limit of the accuracy of the balancing procedure is discussed in section 5.4 as well.

5.2 Mechanical construction of the coil set

5.2.1 PCB coils

The PCB coils were reinforced by foam material in order to prevent them from bending. The apparatus that was used for the reinforcement is shown in figure 5.1. The apparatus consists of two main parts: an aluminum plate and an air pump. The grooves on the surface of the aluminum plate are connected to the air pump. A PCB coil is sucked against the aluminum plate and thus takes the flatness of the aluminum plate. A piece of foam material is glued between the coil and a dummy PCB. The main function of the dummy PCB is to compensate deformations of the coil due to changes in the ambient humidity. The coil remains sucked against the aluminum plate until glue is hardened. Two aluminum plates were used simultaneously to speed up the gluing process.

5.2.2 Coil support

The characterization coil set is shown in figure 5.2. The coil support consists of a massive central pillar in the center of the construction and twelve columns on the

Figure 5.2. Characterization coil set and cryostat containing the gradiometer. During gradiometer balancing the cryostat is slid into the central pillar of the characterization coil set.

periphery. The PCB coils are laying on the working facets of blocks that are firmly attached to the central pillar and to the columns. In order to achieve a high precision of distances between the PCB coils, the working facets have been processed by a single run of a milling machine with the blocks being firmly attached to the elements of the coil support. Each corner of the central pillar and the columns are equipped with thread mechanisms. The thread mechanisms provide a facility to adjust the vertical position of each individual corner of the central pillar and the vertical positions of the columns. The relative vertical position of the adjacent elements of the supporting structure is controlled by employing a bubble level and an iron bar as shown in figure 5.3. The spread of the elevations of the adjacent elements of the supporting structure was measured to be within $0.15mm$. The lateral displacements of the PCB coils in a single layer relatively to each other are restricted by clipping the coils together. The relative lateral displacements of the individual layers of coils is regulated by employing a bubble level in a similar way as shown in figure 5.3. The cryostat with the gradiometer is supported by rails (see figure 5.2). The rails do not load the support structure of the coil set. During the balancing experiment the cryostat is located inside the central pillar. To slide the cryostat into the central pillar, the PCB coils on the way of the cryostat into the central pillar are temporarilly removed.

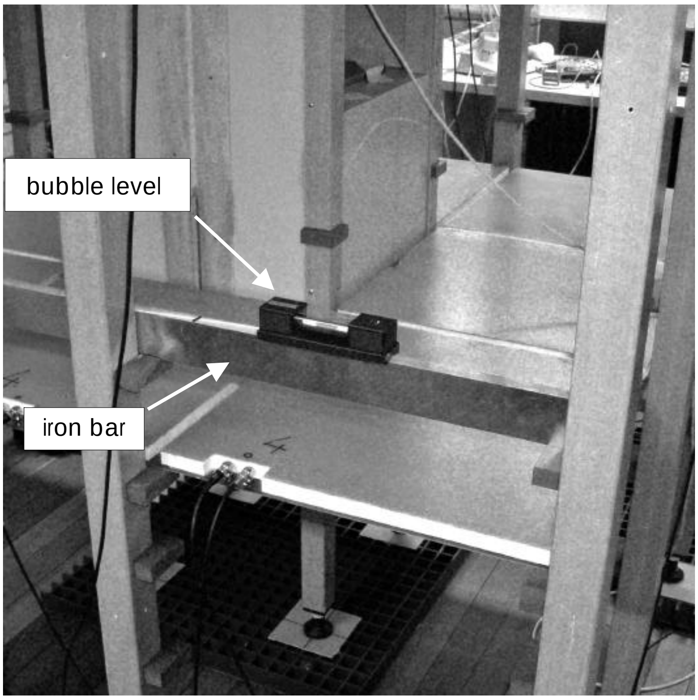

Figure 5.3. Iron bar and bubble level that were used to adjust the height of individual elements of the coil support.

5.3 Characterization of the test magnetic fields produced by the coil set

5.3.1 Setup based on a fluxgate magnetometer

A setup based on a fluxgate magnetometer was constructed in order to assess the homogeneity of the test magnetic fields produced by the coil set. The setup provides a facility to measure three orthogonal components of the magnetic field at points distributed along the vertical axis above and below the center of the coil set. As the magnetic field measurements at the successive spatial points are separated in time by several minutes that are needed for signal averaging and repositioning of the fluxgate magnetometer, special attention was paid to the stability of the setup in time.

A scheme of the setup is shown in figure 5.4. The counter produces two synchronous signals: a test signal (31.25Hz) and a reference signal (4kHz) which externally synchronizes the data acquisition card (DAQ). The DAQ samples the data in four input channels with a sampling frequency of 1kHz in each channel. By application of this synchronization scheme, the time scale of the data acquired by the DAQ is synchronized with the test signal such, that each period of the signal acquired consists of 32 data samples exactly. The characterization coil set is connected to the current source via a 100Ohm resistor. The resistor has a temperature coefficient of $0.01ppm/C^o$. The three-channel fluxgate magnetometer (MAG03, Bargtington) measures the three orthogonal components of magnetic field. DC offsets due to magnetic field of the earth at the outputs of the fluxgate magnetometer are compensated using three DC voltage sources. No analog filtering is applied in the signal lines between the

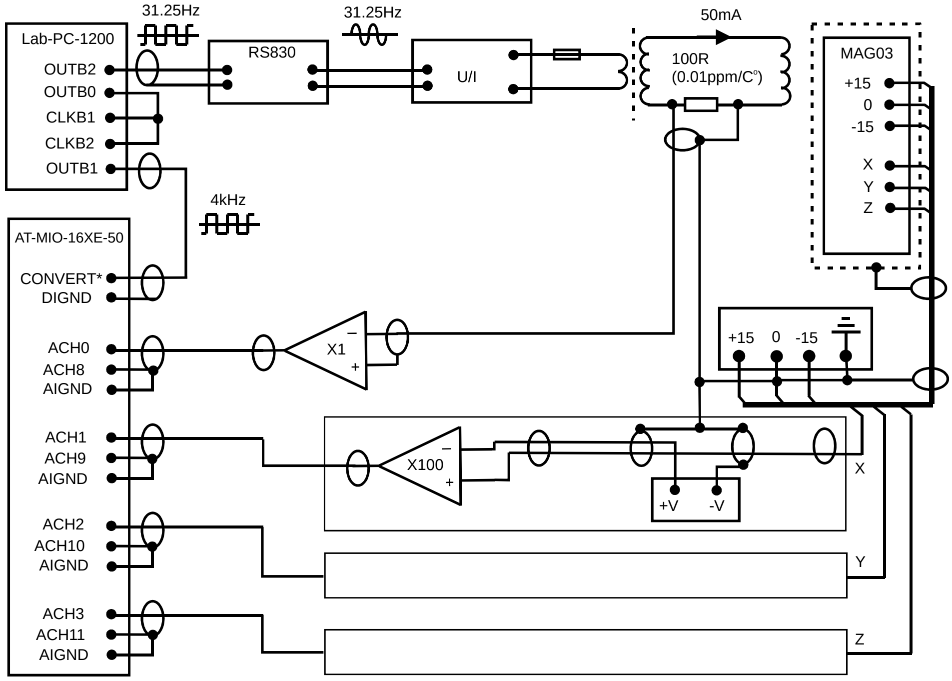

Figure 5.4. A schematic drawing of the setup for evaluation of homogeneity of the magnetic fields produced by the coil set. The instability of the current flowing through the coil set is compensated by measuring the voltage across a resistor with a temperature coefficient of $0.01ppm/^oC$. The sampling frequency of the data acquisition card (DAQ) is synchronous with the current in the coil set.

fluxgate magnetometer and the DAQ to avoid random variations of the signals due to relatively large temperature coefficients of capacitors. Variations of the recorded signals due to instability of the current source were compensated by employing voltage measured on the 100Ohm resister. Subsequently, the compensated signals were truncated to an integer number of periods and averaged.

Two series of two hundreds successive measurements of the magnetic field were acquired in order to assess the stability of the measuring setup in time. During these measurements, the fluxgate magnetometer was fixed at the center of the coil set. The changes of the recorded signals with respect to the first signal of a series are shown in figure 5.5. The first series of the measurements shows an exponent-like instability which is most likely associated with heating-up of the measurement setup. The second series of the measurements shows that the setup reaches stability of $10-20ppm$ after a few hours of operation.

5.3.2 Homogeneity of uniform magnetic fields

The three orthogonal components of the magnetic fields produced by the three uniform magnetic field coils were measured by employing the fluxgate magnetometer based setup described in the previous section. In order to exclude the influence of possible

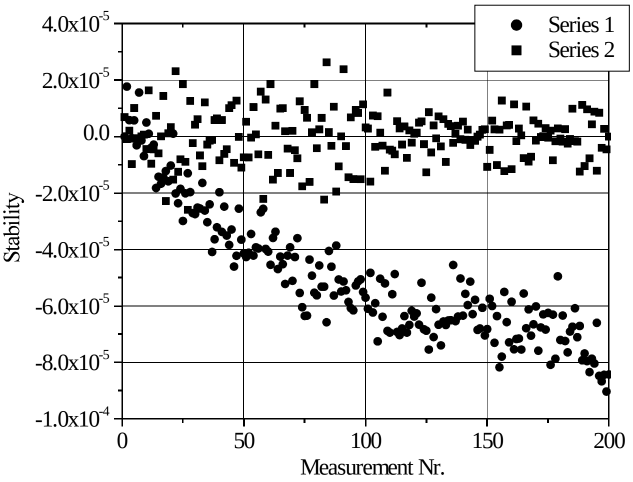

Figure 5.5. Two successive series of magnetic field measurements made by using the setup of figure 5.4. The fluxgate magnetometer was fixed in one point in space. The first series of measurements was made just after the setup was switched on. The second series of measurement was made thirteen hours later. The experiment shows that the setup reaches stability of order of $10 - 20ppm$ after thirteen hours of operation.

rotation and tilt of the fluxgate magnetometer, the magnitudes of the magnetic fields $R = \sqrt{B_x^2 + B_y^2 + B_z^2}$ were considered rather than magnetic field components. The inhomogeneities of the magnetic fields produced by the three uniform magnetic field coils were estimated as

$$H = \left| \frac{R_i - R_0}{R_0} \right| \tag{5.1}$$

where R_i is the magnitude of the magnetic field measured at the $i-th$ point and R_0 is the magnitude of the magnetic field measured at the center of the coil set. However, the vertical coordinate of the center of the coil set is known only approximately. In order to specify this center more accurately the measured magnetic fields were fitted into the simulated magnetic fields within a segment (centered approximately $0.3m$ above the center) where magnetic fields are defined by higher order gradients. During balancing, the center of the gradiometer is located in the center of the characterization coil set. The length of the gradiometer of the FHARMON demonstrator system is

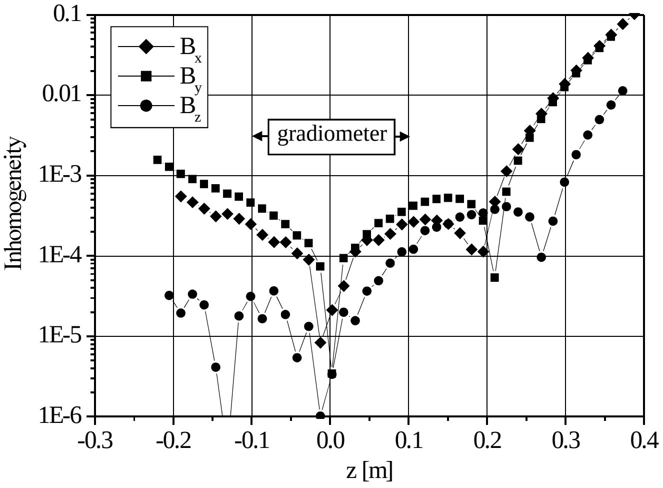

Figure 5.6. Measured inhomogeneity of three uniform magnetic fields produced by the characterization coil set.

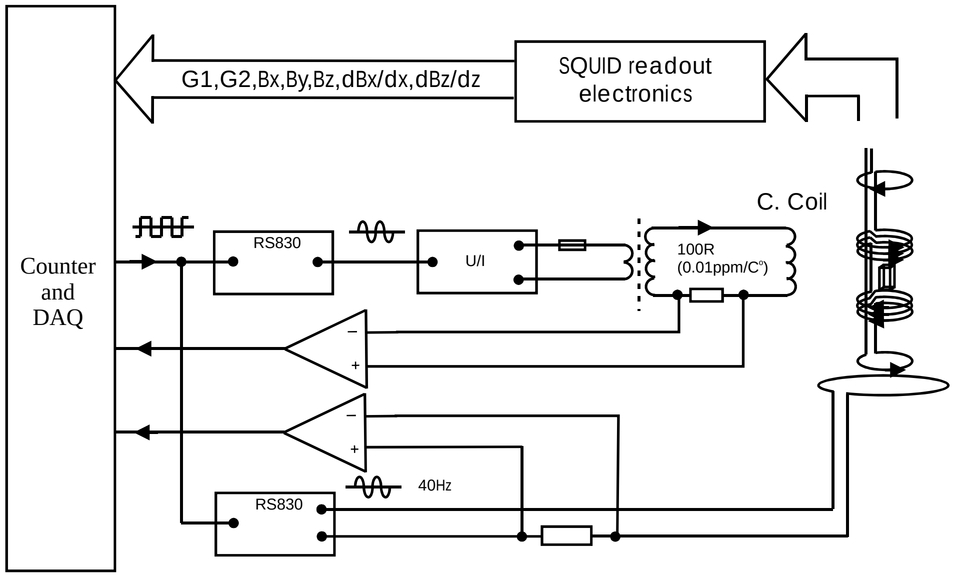

Figure 5.7. A schematic drawing of the setup for gradiometer balancing. All signals are synchronized with the sampling rate of the data acquisition card (DAQ).

0.225m. Thus, the maximal inhomogeneity of the magnetic fields is measured at coordinates $z = \pm 0.1125m$ (see figure 5.6). From figure 5.6 the maximal inhomogeneities of the uniform magnetic fields follow as: $H_x = 3 \cdot 10^{-4}$, $H_y = 4 \cdot 10^{-4}$, $H_z = 10^{-4}$. These values of inhomogeneity are approximately ten times higher (worse) than required (see (4.3)). The most likely reason for the excessive inhomogeneity is the precision of the assembling of the characterization coil set. Comparing these results with the results of the Monte Carlo simulations presented in figure 4.7, a conclusion can be made that the coil set is assembled with a precision of $0.5 - 1mm$. From figure 5.6 it also follows that the B_z-magnetic field coils establish field uniformity better than $2 \cdot 10^{-5}$ in the region between $z = -0.2m$ and $z = 0.05m$. The measurements in this region are limited by stability of the measuring setup (see figure 5.5). This result implies that it is feasible to reach inhomogeneity of order of 10^{-5} by employing a characterization coils designed following the chosen approach.

5.4 Gradiometer balancing

5.4.1 Setup for gradiometer balancing

A scheme of the setup that was used in the gradiometer balancing experiments is shown in figure 5.7. The "counter and DAQ" block consists of two data acquisition cards configured as shown in figure 5.4. All test signals generated by the setup are synchronized with the sampling rate of the data acquisition card such, that all recorded test signals have an integer number of samples per period. This synchronization scheme allows an accurate signal detection.

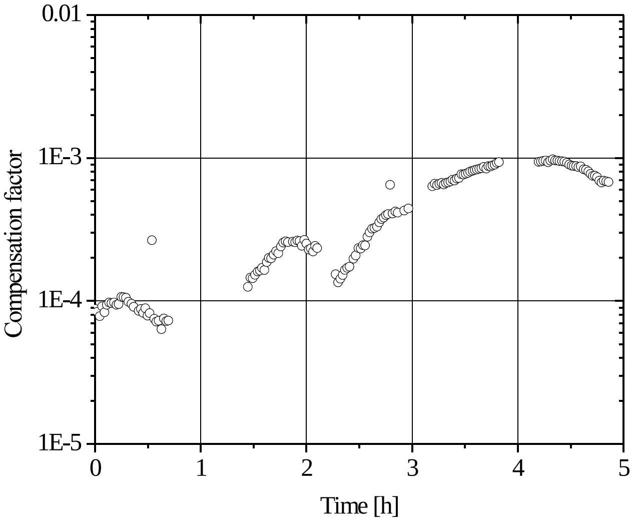

Figure 5.8. Compensation factor as a function of time. The test signal recorded by the gradiometer is compensated by the test signal recorded by the Bz reference at time $t = 0$. As time progresses, field-to-voltage transfers of the gradiometer and reference channels change resulting in a compensation factor deterioration.

Drift of the transfer of the SQUID- and data-acquisition systems is one of the limiting factors of the gradiometer balancing. In order to assess the stability of the setup in time a system of source coils was introduced into the gradiometer. These coils were distributed along the length of the gradiometer such that the signals recorded in all channels had roughly the same order of magnitude. In figure 5.7 these source coils are denoted by a single coil below the gradiometer. A series of 155 successive measurements was made. In the first record of the series, the test signal recorded by the gradiometer was compensated by the test signal that was recorded in the Bz reference. The magnitude and phase of the test signal recorded in the B_z reference were adjusted to be equal to the magnitude and phase of the test signal recorded by the gradiometer. A compensation factor of $9 \cdot 10^{-5}$ was achieved. The magnitude and phase adjustments of the B_z reference channel were kept constant during the whole series of records. As time elapsed, field-to-voltage transfers of the channels changed resulting in a deterioration of the compensation factor. In figure 5.8 the compensation factor is shown as a function of time. Similar results were obtained when compensating the test signal in the gradiometer channel by Bx and By references. It was concluded that the setup can provide an accuracy of balancing of order of $1000ppm$. Comparing this value with the measured inhomogeneity of the rest magnetic fields (see figure 5.6) a conclusion can be made that the drift of the flux-to-voltage transfer is the main factor that limits the accuracy in the gradiometer balancing.

5.4.2 Initial imbalance coefficients

The initial imbalance coefficients of the second order gradiometers of the FHARMON system were measured at a frequency of $31.25Hz$. In this experiment, the characterization coil set was equipped with coils designed for generating uniform magnetic fields in $x-$, $y-$, $z-$ directions and two first-order longitudinal gradients (see (4.8)). The coils that produce transversal gradients were omitted from the setup. Instead, the

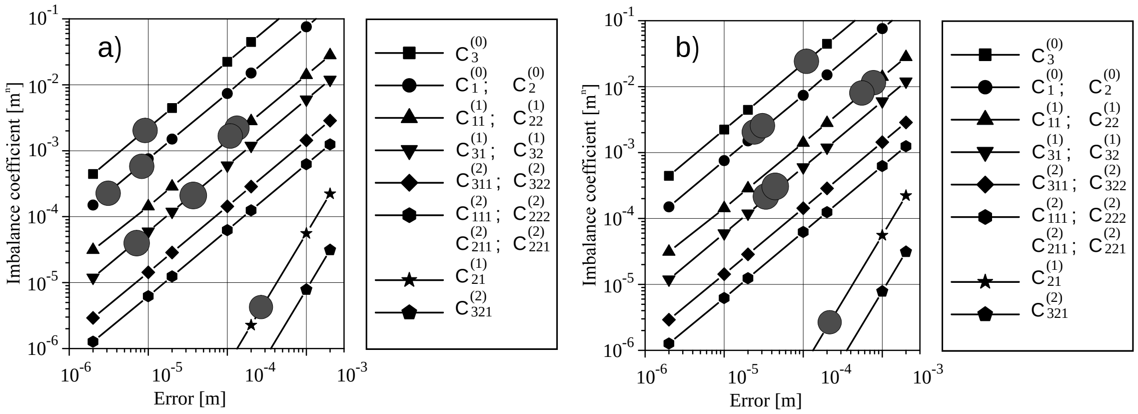

Figure 5.9. Measured and simulated imbalance coefficients. Black circles represent the imbalance coefficients measured at $31.5Hz$. The rest of the data are simulated imbalance coefficients (see chapter 3). a) Imbalance coefficients of the upper second-order gradiometer (G1). b) Imbalance coefficients of the lower second-order gradiometer (G2). The error is defined in section 3.2.3.

PCB coils designed for generating transversal uniform magnetic fields were interconnected such that they generated transversal gradients. In this case, the homogeneity of the transversal gradients is worse than that of the dedicated coil set but is sufficient for imbalance measurements. As discussed in chapter 4, the homogeneity of the test magnetic fields defines the relative accuracy of the imbalance measurements. For this reason, a coil producing transversal first order gradients with an inhomegeneity as high as 0.1 can be used to measure imbalance coefficients with an adequate accuracy (however, this accuracy may be not adequate for balancing). Moreover, the current density with a symmetry suitable for generating the transversal gradients induces zero net magnetic flux in an ideal second order gradiometer. For this reason, the ISR parameter (see chapter 4) is expected to be adequate as well. A confirmation of a low ISR can be made by observing that the imbalance $C_{21}^{(1)}$ was measured at the level of $2.7 \cdot 10^{-6}$ (see table 5.1). The measured imbalance coefficients are shown in figure 5.9 together with the imbalance coefficients simulated in chapter 3. In the caption of the figure and throughout the text the upper and the lower second-order gradiometers are denoted as $G1$ and $G2$, respectively. The imbalance coefficients $C_3^{(0)}$, $C_{11}^{(1)}$ and $C_{22}^{(1)}$ are higher in the gradiometer $G2$. The frequency responses of the corresponding balancing filters show a relatively weak dependence on frequency (as will be shown in section 5.4.3), implying that the excessive imbalance coefficients are due to mechanical imperfections of the gradiometer $G2$.

In both gradiometers, the difference between longitudinal imbalance coefficients $C_{11}^{(1)}$ and $C_{22}^{(1)}$ is of order of $10^{-4}m$, implying that the first order longitudinal imbalance can be reduced to $10^{-4}m$ by employing only one reference dBz/dz. The imbalance coefficient $C_{21}^{(1)}$ is negligible in both gradiometers for the reasons discussed in chapter 3. The required imbalance coefficients, measured imbalance coefficients and required improvements of the imbalance coefficients are summarized in table 5.1.

Table 5.1. Required imbalance coefficients, initial imbalance coefficients and required improvement of the imbalance coefficients.

	required	initial G1 (31.5Hz)	required improvement G1	initial G2 (31.5Hz)	required improvement G2
$C_1^{(0)}$	$5 \cdot 10^{-7}$	$1.7 \cdot 10^{-4}$	340	$1.9 \cdot 10^{-3}$	3800
$C_2^{(0)}$	$5 \cdot 10^{-7}$	$6.3 \cdot 10^{-4}$	1260	$1.1 \cdot 10^{-3}$	2200
$C_3^{(0)}$	$5 \cdot 10^{-7}$	$2.3 \cdot 10^{-3}$	4600	$3.4 \cdot 10^{-2}$	68000
$C_{11}^{(1)}$	$6 \cdot 10^{-6}$	$1.6 \cdot 10^{-3} m$	267	$9.7 \cdot 10^{-3} m$	1617
$C_{22}^{(1)}$	$6 \cdot 10^{-6}$	$1.7 \cdot 10^{-3} m$	283	$9.9 \cdot 10^{-3} m$	1650
$C_{31}^{(1)}$	$6 \cdot 10^{-6}$	$5.7 \cdot 10^{-5} m$	10	$3.5 \cdot 10^{-4} m$	58
$C_{32}^{(1)}$	$6 \cdot 10^{-6}$	$1.8 \cdot 10^{-4} m$	30	$2.6 \cdot 10^{-4} m$	43
$C_{21}^{(1)}$	$6 \cdot 10^{-6}$	$4.9 \cdot 10^{-6} m$	-	$2.7 \cdot 10^{-6} m$	-

If the requirements for the first order imbalance are relaxed by approximately a factor of ten, only longitudinal imbalances will require balancing. In this case, all the first-order gradient references except of dBz/dz can be omitted from the setup.

From table 5.1 it follows that the imbalance $C_3^{(0)}$ of the gradiometer $G2$ requires improvement by a factor of 68000. This implies that the required inhomogeneity of the corresponding characterization coil needs to be at least $1/68000 = 1.5 \cdot 10^{-5}$, implying that, in general, an inhomogeneity of order of 10^{-5} can indeed be required in the gradiometer balancing experiments.

In the previous section it was shown that the drift of field-to-voltage transfer of the setup limits the accuracy of balancing to 1000 times. For this reason, the maximal improvement of imbalance that can be achieved equals 1000. From table 5.1 it follows that the factor of 1000 is not sufficient for half of imbalance coefficients.

5.4.3 Compensation of the imbalance coefficients

A scheme of the setup that was used in this experiment is shown in figure 5.7. Five test magnetic fields were applied to the gradiometer: $B_0\widehat{x}$, $B_0\widehat{y}$, $B_0\widehat{z}$, $B_0\left(x\hat{x} - y\hat{y}\right)$, $B_0\left(x\hat{x} + y\hat{y} - 2z\hat{z}\right)$. The frequency of the test magnetic fields was varied linearly on a logarithmic scale in a bandwidth of $1 - 125Hz$. The signals of two second-order gradiometers and five references ($G1$, $G2$, B_x, B_y, B_z, dB_x/dx, dB_z/dz) were recorded for each test magnetic field and each iteration of frequency yielding a set of 155 signals. The duration of each record was one minute. The recorded signals were corrected for the skew (time delay between the channels imposed by the data acquisition card, see www.ni.com for details) and downsampled to a sampling frequency of $250Hz$. Next, the magnitudes and phases of the signals were calculated by averaging. In three records, the synchronization of the DAQ with the test signals was lost. These signals were excluded from the computer routines responsible for signal detection. The gaps were filled by interpolation. However, the balancing filters (see the discussion below), were applied to the non-synchronously recorded signals to confirm that the quality of

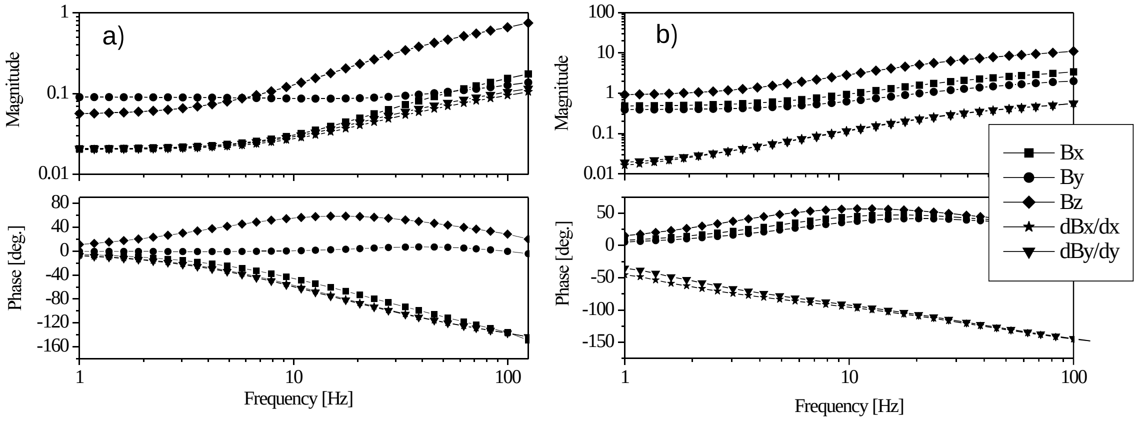

Figure 5.10. Frequency dependent balancing coefficients (balancing filters) calculated by employing equation (5.2). a) Balancing coefficients of the upper second-order gradiometer (G1). b) Balancing coefficients of the lower second-order gradiometer (G2).

the balancing is the same whether the recorded signal are synchronized with the time sale of DAQ or not.

An analysis of the recorded signals showed that the reference channels are not entirely orthogonal. For instance, the signals recorded by the B_x reference in presence of $g_1^{(0)}\widehat{x}$, $g_1^{(0)}\widehat{y}$ and $g_1^{(0)}\widehat{z}$ test magnetic fields are related as 1:0.63:0.36. Due to this nonorthogonality all reference channels need to be used in order to balance a response of one second order gradiometer to a single test magnetic field (or, in other words, the matrix $\mathbf{M}$ in (5.2) is not diagonal). The balancing coefficients were calculated as:

$$\vec{c} = \mathbf{M}^{-1}\vec{g} \tag{5.2}$$

where $\vec{c}$ is a column vector composed of balancing coefficients; entries of the matrix $\mathbf{M}$ are complex numbers that represent magnitudes and phases of the signals recorded in the reference channels; similarly, $\vec{g}$ is a column vector composed of magnitudes and phases of the signals of one of the second-order gradiometers. A single component of $\vec{c}$ is a complex value that represents a frequency response of the corresponding balancing filter at a particular frequency. Equation 5.2 was evaluated for each variation of the frequency of the test magnetic fields yielding frequency responses of the balancing filters. The frequency responses of the calculated balancing filters are shown in figure 5.10. The frequency responses were interpolated and approximated by FIR filters by employing the frequency sampling method of FIR filters design. In order to minimize the approximation error, phases of the target frequency responses were increased by $200 \cdot 2f/f_s \cdot \pi$; where $f_s = 250Hz$ is the sampling frequency.

As stated above, the goal of the balancing procedure is to find a set of balancing coefficients (filters) for all reference channels such, that the sum of the signals of the second-order gradiometer and that of the references equals zero for all applied test magnetic fields in the frequency bandwidth of $1 - 125Hz$. Accordingly. the designed balancing filters were applied to all recorded signals (155, see the beginning of this

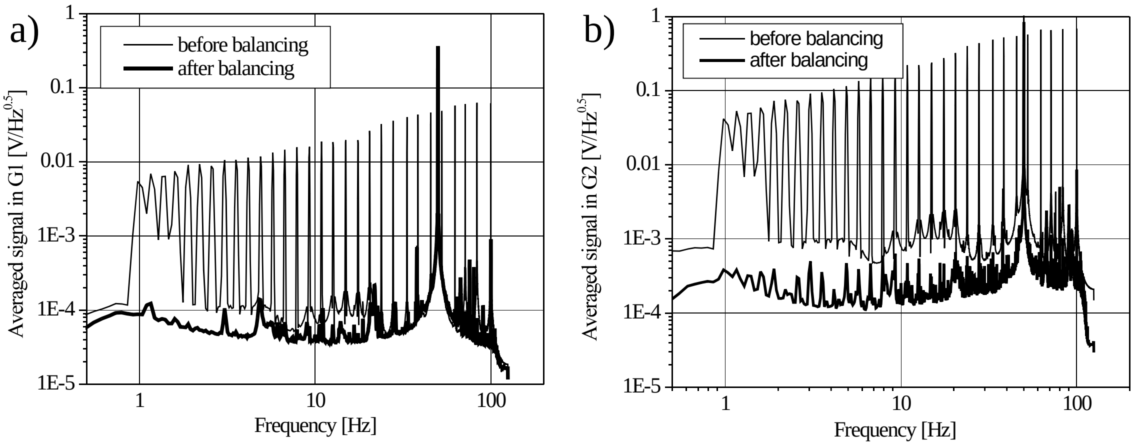

Figure 5.11. Averaged Power Spectral Densities (PSDs) of the signals of the second-order gradiometers recorded in presence of three orthogonal uniform magnetic fields and two longitudinal first-order gradients. The thin lines represent averaged PSDs of unbalanced gradiometers. The thick lines represent averaged PSDs of balanced gradiometers. a) Averaged PSDs of the upper second-order gradiometer (G1). b) Averaged PSDs of the lower second-order gradiometer (G2).

section) resulting in a data set that corresponds to signals of balanced gradiometers. Power Spectral Densities (PSDs) of all balanced second-order gradiometer signals were calculated and averaged. Similarly, the averaged PSD of unbalanced second-order gradiometer signals was calculated as well. The results are presented in figure 5.11. The results suggest that the sensitivity of the gradiometer to the test magnetic fields was suppressed to the level of the system noise, though some residuals of the test signals can be observed in the balanced signal of the gradiometer G2.

5.5 Conclusion

The construction of the characterization coils is described. The high required accuracy ($< 0.1mm$) of the relative positioning of the individual PCB coils was the main challenge during the construction of the characterization coil set. The measured relative displacements of the PCB coils in the vertical direction were within $0.15mm$. However, the inhomogeneity of the uniform magnetic fields was measured to be of the order of $4 \cdot 10^{-4}$. This level of inhomogeneity implies an accuracy of the construction of the order of $0.5 - 1mm$. From this, it was concluded that the characterization coil set requires more advanced control over the displacements of individual layers of the PCB coils in relation to each other and over displacements of individual PCB coils within the layers.

The drift of the flux-to-voltage transfer of the FHARMON gradiometer system was measured to be of the order of $1000ppm$. This relatively high drift of the system is the main limiting factor of the accuracy of the gradiometer balancing.

The analysis of the measured initial (before balancing) imbalance coefficients suggests that the longitudinal first-order imbalance coefficients are the major contributors to the first-order imbalance. If the requirements for the first-order imbalance are relaxed by a factor of ten, the gradiometer would require only four reference channels: B_x, B_y, B_z, dBz/dz. The maximal measured imbalance coefficient equals $3.4 \cdot 10^{-2}$. Balancing this imbalance coefficient to the required level of $5 \cdot 10^{-7}$ would require test magnetic field with inhomogeneity of order of $1.5 \cdot 10^{-5}$.

The balancing filters were implemented for the two second-order gradiometers of the FHARMON system. The implemented balancing filters are capable of suppressing the gradiometer signals that are induced by the test magnetic fields to the level of the system noise. After these experiments, the gradiometer was placed into a cryocooler-cooled measuring head. A larger research effort appeared to be required to get this system cryogenically operating (Rijpma *et al.*, 2008). For this reason, at the moment of this writing no data were available with the gradiometer setup operating in a magnetically noisy environment.

Chapter 6

Eddy currents and thermal noise in metallic discs

6.1 Introduction

Typically, a SQUID-based gradiometer is enclosed by a radio-frequency-interference (RFI) shield as well as by a thermal shield made of aluminum-coated Mylar film (superinsulation). Both, the RFI and thermal shields are conductive. The eddy-currents induced in these shields disturb the environmental magnetic field causing frequency dependent imbalance of the gradiometer. The thermal magnetic noise generated within the conducting shields couples to the gradiometer decreasing the resolution of the measuring system. Methods of estimating the eddy-current and thermal noise effects on the measuring system are required. Such methods were developed in (Rijpma, 2002). In this chapter, these methods are reviewed and confirmed experimentally. As discussed in chapter 3, a shield (ether RFI or thermal shield) can be considered as a combination of disk- and cylindrically- shaped conductors electrically isolated from each other. For simplicity reason, only magnetic disturbances caused by the presence of a conducting disk are considered.

A time varying magnetic field induces eddy currents in the conducting disk. At the lower frequencies the induced eddy currents are distributed almost uniformly over the thickness of the disk. The magnetic flux due to eddy currents through a concentric coil can be calculated as discussed in (Rijpma, 2002). In opposite, at the higher frequencies the eddy currents are confined to a thin layer on the surface of the disk and magnetic field is expelled from the disk. In the high-frequency limit, the total magnetic field is the same as in the case of a superconducting disk as discussed in (Overweg and Walter-Peters, 1978). Empirically, it was found that in the frequency range between the low- and- high frequency limits a conducting disk acts as a high-pass filter. As a consequence, an expression for the magnetic flux due to eddy currents that is valid in the entire frequency range was obtained.

Thermal noise is present in all objects that are electrically conducting. Each

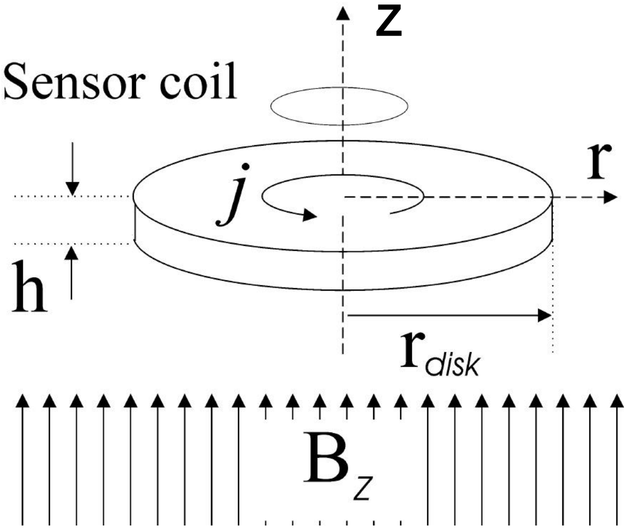

Figure 6.1. The circular conducting disk in an applied uniform magnetic field. Adapted from (Rijpma, 2002).

volume element generates a short-circuit noise current that generates, in turn, a fluctuating magnetic flux. The average value of the current in a volume element is zero. The root-mean-square value (time-averaged power) of these noise sources is defined by Nyquists theorem. The frequency distribution of thermal noise power is uniform (i.e.,white noise). Expressions for magnetic field fluctuations arising from thermal motion in an infinite conducting slab have been derived by (Varpula and Poutanen, 1984). (Kasai *et al.*, 1993) extended these calculations and obtained the magnetic field fluctuations at the axis of disks of finite extent. (Rijpma, 2002) has derived expressions for the magnetic flux noise in a circular loop due to thermal noise in metallic disks. In this chapter these results will be compared with the experimental data.

6.2 Theory

6.2.1 Eddy currents

First, eddy currents in a circular disk with radius r_{disk} and height h in the presence of a uniform magnetic field are considered. The disk is depicted in figure 6.1.

Low-frequency-limited case

The following assumptions are made:

- The electric conductivity of the disk is homogeneous and isotropic.
- The permeability everywhere (i.e. both in the conductor and outside the conductor) is that of free space (i.e. μ_0).
- The frequency of the applied magnetic field is below $1000 Hz$, which is the highest frequency of interest in Biomagnetism (Plonsey and Heppner, 1967).

- The disks used have a permittivity of free space and a conductivity higher than $10^6 S/m$; hence $\omega\varepsilon/\sigma << 1$ and as a consequence capacitive effects can be neglected for frequencies up to $1000Hz$.

The disk is located in the $z = 0$ plain and has a specific resistance ρ. A changing uniform magnetic field is applied in the direction perpendicular to the disk (see figure 6.1). As the assumed frequency of the applied magnetic field is below $1000Hz$, the skin depth $\delta = 1/\sqrt{\pi f \mu \sigma}$ is much larger than the thickness of the disk (centimeters compared to millimeters). Consequently, the currents induced in the disk by the applied magnetic field are distributed uniformly in the z direction. The disk is divided into a set of concentric rings with radius r and width dr. From

$$\oint \overrightarrow{E} \cdot \overrightarrow{dl} = -\frac{d\Phi}{dt} \tag{6.1}$$

and

$$\overrightarrow{j} = \sigma \overrightarrow{E} = \frac{\overrightarrow{E}}{\rho} \tag{6.2}$$

where $\overrightarrow{j}$ is the current density and σ is the conductivity, it follows that the current in each ring-shaped segment equals

$$j = -\frac{r}{2\rho}\frac{dB_z}{dt} \tag{6.3}$$

The ring-shaped segments of the disk form coplanar circuits. Consequently, the flux in the sensor coil of the magnetometer due to eddy currents is

$$\Phi_{\omega \to 0} = \int_0^{r_{disk}} M(r) j(r) h dr \tag{6.4}$$

where M(r) is the mutual inductance between a ring-shaped segment of the disk and the coil. The mutual inductance can be calculated by employing complete elliptic integrals of the first and second kinds (ter Brake, 1986), (Rijpma, 2002), (Uzunbajakau *et al.*, 2003). The elliptic integrals, in turn, are well tabulated functions and can be found in most of the simulation-dedicated software packages such as Matlab.

High-frequency-limited case

At very high frequencies, the currents and magnetic field are confined to the surface of the disk. As the magnetic field cannot penetrate the disk, the normal component of the magnetic field must vanish on the surface of the disk. The magnetic field outside the disk can be calculated by solving Laplace equations. This problem has been solved in (Overweg and Walter-Peters, 1978) for a thin disk resulting in the following equation for the net magnetic flux through a sensor coil with radius r_{sensor}:

$$\Phi_{\omega \to \infty} = 2 r_{sensor}^2 B_{appl} \left(\frac{\nu}{\nu^2 + 1} - arccot(\nu) \right) \tag{6.5}$$

where

$$\nu^2 = \frac{1}{2r_{disk}^2}\left(z^2 + r_{sensor}^2 - r_{disk}^2 + \left[\left(z^2 + r_{sensor}^2 - r_{disk}^2\right)^2 + 4r_{disk}^2 z^2\right]^{1/2}\right) \tag{6.6}$$

where z is the distance between disk and sensor coil.

Frequency range between the low- and high-frequency limited cases

At lower frequencies, the conducting disk behaves as a capacitor with respect to the frequency of the applied magnetic field. In opposite, the magnetic field produced by the eddy-currents is frequency independent at higher frequencies what can be regarded as a resistor-like behavior. For these reasons, one can presume that the magnetic flux due to eddy currents as a function of frequency resembles a high-pass filter. Thus, the following should hold on the entire frequency range:

$$\frac{\Phi_{eddy}}{\Phi_{appl}} = c \times \frac{-i\frac{\omega}{\omega_0}}{1 + i\frac{\omega}{\omega_0}} \tag{6.7}$$

In the low-frequency limit, this expression reads

$$\lim_{\omega\to 0} \frac{\Phi_{eddy}}{\Phi_{appl}} = \frac{\Phi_{\omega\to 0}}{\Phi_{appl}} = -ic\frac{\omega}{\omega_0} \tag{6.8}$$

and in the high-frequency limit

$$\lim_{\omega\to\infty} \frac{\Phi_{eddy}}{\Phi_{appl}} = \frac{\Phi_{\omega\to\infty}}{\Phi_{appl}} = -c \tag{6.9}$$

Thus, constant c can be calculated using (6.5) and, subsequently, the constant ω_0 can be calculated using (6.4). Obviously, at very low frequencies, the flux ratio is zero.

6.2.2 Thermal noise

The disk depicted in figure 6.1 can be viewed as a collection of infinitesimal volume elements. Each volume element generates a noise current dipole (Varpula and Poutanen, 1984). Each current dipole (and its accompanying volume current) creates a magnetic field. The current dipoles are not correlated, so at any location the resulting magnetic field noise from the whole disk is obtained by summing the power of the field noise resulting from the separate elements. As the elements are continuously distributed they can be integrated. The contribution to the magnetic field in the z direction caused by current dipoles in the radial direction is zero. The contribution of current dipoles in the z direction is also zero. So the only contributing elements are the current dipoles that have a tangential direction. These current dipoles are the primary sources. However, a magnetic field is the superposition of the fields due to primary sources and volume currents. The volume currents can be described by means of imaginary sources, so-called secondary sources (Sarvas, 1987). The secondary sources are current elements that are perpendicular to interfaces between regions of different conductivity. Consequently, the secondary sources in the circular disk displayed in figure 6.1 will be in the z direction and in the radial direction. Hence, the volume elements do not contribute to the z component of the magnetic field on the axis. So the only contributing elements to the z component of the magnetic field on the axis are the tangential components of the primary sources. Next, a subset of the infinitesimal volume elements is considered. This subset is chosen such that its elements establish a ring-shaped segment with radius r, width dr, and height dh. It is assumed that their combined contribution to the noise field can be obtained by considering the ring as a resistance and calculating the short-circuited electrical current noise according to Nyquist's theorem

$$\overline{i_{ring}^2} = \frac{4k_B T \triangle f}{\triangle R} \tag{6.10}$$

where k_B is the constant of Boltzmann and $\triangle R$ the resistance of the ring, that reads

$$\triangle R = \frac{2\pi r}{\sigma dr dh} \tag{6.11}$$

leading to

$$\overline{i_{ring}^2} = 4k_B T \sigma \triangle f \frac{dr dh}{2\pi r} \tag{6.12}$$

The mean square value of the flux through a coil parallel to the disk, assuming that the disk is thin (i.e. $h << d$, where d is the distance between disk and sensor coil), is

$$\overline{\Phi^2} = \frac{4k_B T \sigma h \triangle f}{2\pi} \int_0^{r_{disk}} \frac{M^2(r)}{r} dr \tag{6.13}$$

where M is the mutual inductance between concentric ring-shaped segments of the disk and the sensing coil. As discussed above, the mutual inductance can be calculated by means of complete elliptic integrals of the first and second kinds.

6.3 Description of the experiments

Measurements were carried out on nine disks that varied in conductivity and dimensions. Their parameters are given in table 6.1. All disks were cut from metal sheets. Strips were made from the same sheets to measure the conductivity by means of the four-point method.

6.3.1 Eddy Currents

The influence of eddy currents was measured as the ratio of the flux in a sensor coil due to eddy currents and the flux due to the applied magnetic field. The experimental setup is sketched in figure 6.2a. A low-T_c SQUID was used as a sensor. The SQUID

Table 6.1. Parameters describing the metallic disks used in the experiments

Material	Conductivity (S/m)	Skin depth at 1000Hz (mm)	Thickness (mm)	Diameter (mm)
Copper	5.37×10^7	2.2	0.1	83
Copper	4.44×10^7	2.4	0.5	83
Copper	4.79×10^7	2.3	1.0	83
Copper	4.62×10^7	2.3	3.0	83
Copper	4.44×10^7	2.4	0.5	40
Lead	0.445×10^7	7.5	0.5	83
Brass	1.45×10^7	4.2	0.5	83
Steel	0.143×10^7	13	0.5	83

is a magnetic flux-to-voltage converter with a nonlinear inputoutput characteristic. In order to linearize this characteristic, the SQUID was operated as a zero-detector in a flux-locked loop (FLL in figure 6.2). A more detailed description of the SQUID and FLL that were used can be found in (ter Brake *et al.*, 1991c), (Flokstra *et al.*, 1991). The effective area of a bare SQUID is relatively small yielding a relatively low sensitivity to the magnetic field. In order to increase the sensitivity, a superconductive flux transformer was used consisting of a sensing coil and an input coil that was inductively coupled to the SQUID. The intrinsic noise of the measurement setup was white in the frequency region above $1Hz$. The level of the white noise was $5fT/\sqrt{Hz}$. The bandwidth of the measurement setup (SQUID plus FLL) was $2kHz$. The sensor coil with a diameter of $30mm$ was positioned at a point midway between a set of Helmholtz coils. In order to measure the flux due to eddy currents as accurately as possible, a compensation circuit was used consisting of an adjustable amplifier and an adjustable phase shifter. For each frequency, the measurements were performed in two steps. During the first step, a magnetic field was applied without any disk present. By simultaneous adjustment of the amplifier and phase shifter, the signal due to the applied field was compensated (balanced), nullifying as much as possible the output voltage of the flux-locked loop (FLL). The applied current I_{appl} and the remaining output voltage U_{out} were recorded defining the initial imbalance. This was done to verify that the amplitude of U_{out} due to the initial imbalance is well below that due to eddy currents. The output voltage of the SR830 lock-in amplifier U_{out} is a complex quantity. Its magnitude is equal to the output voltage of the FLL and its phase is equal to the phase difference between the applied current I_{appl} and the output voltage of the FLL. During the second step, a disk was placed in the appropriate position underneath the cryostat and the output voltage U_{out} was recorded again. As the flux applied by the Helmholtz coils was compensated in the first step of the measurement, the output voltage is proportional to the flux due to eddy currents. From figure 6.2, one can deduce an expression for the influence of eddy currents in terms of imbalance

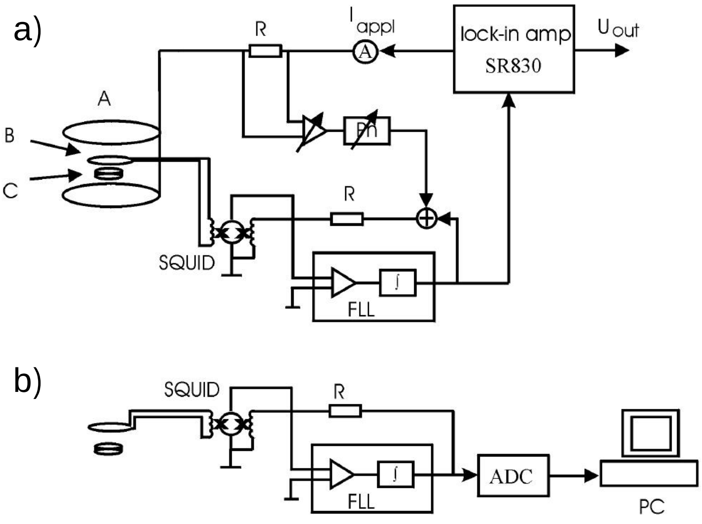

Figure 6.2. a) Experimental setup for the measurement of the flux due to eddy currents in a conducting disk. The Helmholtz coil is indicated by A, the sensor coil by B, the disk by C, and the adjustable phase shifter by Ph. b) Experimental setup for the measurement of the flux due to thermal noise in a conducting disk.

as

$$\frac{\Phi_{eddy}}{\Phi_{appl}} = \frac{U_{out}}{I_{appl} H(i\omega)} \tag{6.14}$$

where Φ_{eddy} is the flux in the sensor coil due to eddy currents and $\Phi_{appl} = B_{appl} \times \pi r_{sensor}^2$. The transfer function $H(i\omega)$, which relates the applied current and the output voltage, was measured separately (compensation circuit was open). For six disks, the ratio in magnitudes and difference in phase between the eddy current flux and the applied flux were measured as a function of the frequency of the applied field and as a function of the distance between disk and sensor coil of the magnetometer. Theoretical values of the ratio of the amplitudes of Φ_{eddy} and Φ_{appl} were calculated using (6.4) and (6.7).

6.3.2 Thermal noise

The thermal noise measurements were carried out in the bandwidth from $1Hz$ to $1kHz$. The measurement setup is depicted in figure 6.2b. The thermal noise was recorded of eight disks and a power spectral density was calculated using Welch's method and a Hanning window (Oppenheim and Schafer, 1975). Subsequently, the white noise levels were estimated from the power spectral densities by averaging the spectra in frequency regions where no other spectral components ($1/f$ noise at low frequencies, noise due to vibrations, power line interference and its harmonics) were present. From the resultant white noise levels, the intrinsic noise of the measurement system was subtracted. The level of the intrinsic system white noise was measured without any conducting disk present.

The flux due to thermal noise was measured as a function of the distance between the disk and the sensor coil, the thickness of the disk, and the conductivity of the disk. Two different sensor coils were used of $30mm$ and $50mm$ diameter, respectively.

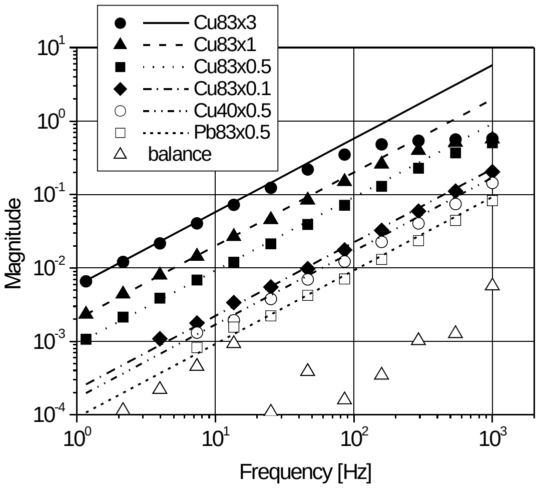

Figure 6.3. Ratio of the amplitude of the eddy current flux and that of the applied flux as a function of the frequency for the various disks. The lines represent the theoretical values in the low-frequency limit calculated using (6.4). The markers indicate the measurements. The open triangles depict the balance of the applied flux, i.e., the residual signal after compensation of the applied flux. The balance defines the minimum value that can be measured using the experimental setup.

The thermal flux noise was calculated for all eight disks using (6.13). The results are expressed in terms of field noise, i.e., the measured flux divided by the area of the sensor coil.

As mentioned previously, the flux noise generated by a disk is only due to the presence of primary sources. However, if the disk is cut into pie-shaped pieces that are electrically insulated from each other, secondary sources are present at the sides of the wedges. These secondary sources are tangentially orientated. Consequently, these secondary sources will contribute to the magnetic field in the z direction. This contribution counteracts the contribution of the primary sources. Hence, the combination of the pie-shaped pieces should generate a lower level of field noise in the sensor coil than the original intact disk. However, if the disk is cut so that it forms a smaller disk and a concentric ring, the secondary sources at the interface have a radial orientation and, hence, they will not contribute to the magnetic flux in the sensor coil. In order to validate these assumptions, two copper disks with a thickness of $0.5mm$ and diameter $83mm$ were cut in pieces. One was cut so that it formed a disk with a diameter of $40mm$ that fitted in a ring with an inner diameter of $40mm$ and an outer diameter of $83mm$. The two pieces were insulated from each other during measurements. The second disk was divided in pieces shaped like wedges of pie. The number of wedges was varied from 2 to 16. All wedges were electrically insulated from each other.

6.4 Results

6.4.1 Eddy currents

Typical results for the flux due to eddy currents are shown in figures 6.3, 6.4 and 6.5. In figure 6.3 the magnetic flux in the sensor coil divided by the applied flux is shown as a function of the frequency. The lines represent theoretical values derived for the

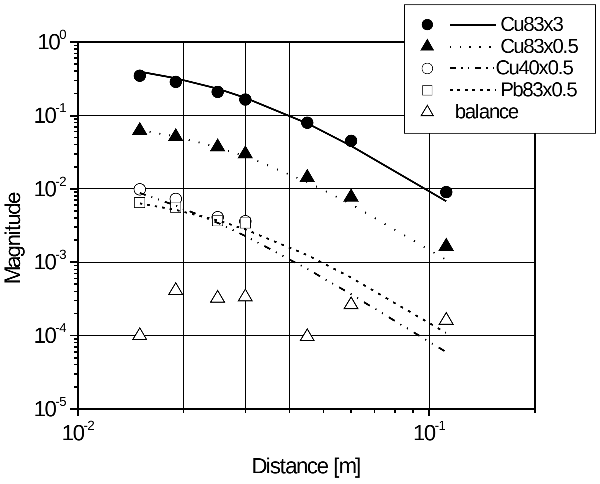

Figure 6.4. Ratio of the amplitude of the eddy current flux and that of the applied flux as a function of the distance between the disk and the sensor coil. The frequency of the applied field was $85Hz$, where the low-frequency approximation given by (6.4) is valid. The lines represent the theoretical values, the markers the measured ones. The open triangles depict the balance of the applied flux, i.e., the residual signal after compensation of the applied flux. The balance defines the minimum value that can be measured using the experimental setup.

low-frequency limited case, and the markers are the measured values. Deviation of the measured values from the calculated ones for thicker disks at higher frequencies marks the transition between the low- and high- frequency limiting cases. Figure 6.4 shows the flux in the sensor coil as a function of the distance. The lines correspond to the theoretical values derived for the low-frequency-limited case.

To emphasize the validity of (6.7), the measured and theoretical data that are presented in figures 6.3 and 6.4 are depicted in a single graph in the following way. Rearranging the terms in (6.7) yields

$$G(x) = \frac{\Phi_{eddy}}{\Phi_{appl}} \frac{1}{c} = \frac{-i\frac{\omega}{\omega_0}}{1 + i\frac{\omega}{\omega_0}} = -\frac{ix}{1 + ix}. \tag{6.15}$$

The function $G(x)$ does not depend on parameters describing the disks or the applied field. For this reason, all experimental data presented in figures 6.3 and 6.4 are expected to collapse into two curves (amplitude and phase) described by $G(x)$. Both the theoretical and experimental values obtained for the magnitude and the phase of $G(x)$ are shown in figure 6.5.

6.4.2 Thermal noise

The results of the thermal noise flux measurements are shown in figures 6.6 and 6.7. Again, the line shows the theoretical value and the markers the measured ones. The intrinsic system noise of $25fT^2/Hz$ is subtracted from the measured values. The results show a fair agreement between theoretical and experimental results.

Commonly, the mean square value of the flux in the sensor coil is approximated

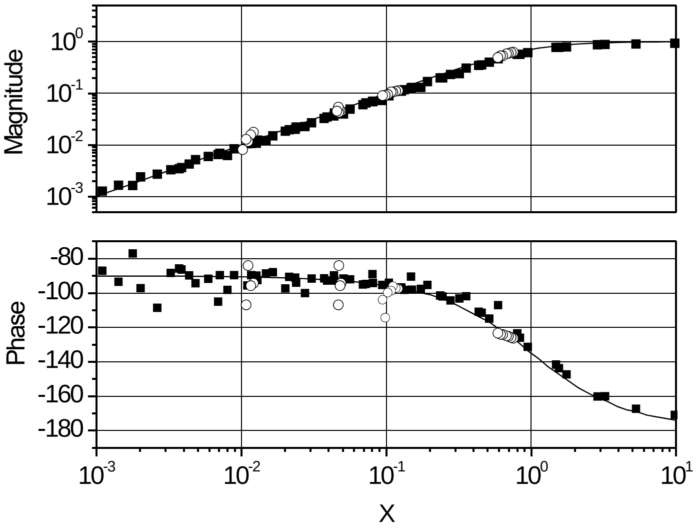

Figure 6.5. Amplitude and phase of $G(x)$ (see 6.15) describing the relationship between the flux in the sensor due to eddy currents and the flux due to the applied magnetic field. The solid curves represent amplitude and phase of $G(x)$. Experimental data presented in figures 6.3 and 6.4 are described by black squares and open circles, respectively.

by

$$\overline{\Phi^2} = \overline{B^2_{z,disk}} \times \pi r^2_{sensor} \tag{6.16}$$

using an expression for $\overline{B^2_{z,disk}}$ derived in (Kasai *et al.*, 1993). The dotted lines in figure 6.7a show this approximation. Measurements of thermal noise versus distance were performed using two types of sensor coils with diameters of 30mm and 50mm. In figure 6.7a, the results are shown for the sensor coil of 50mm. Comparison of the results obtained with the two sensor coils shows that (6.13) approximates the

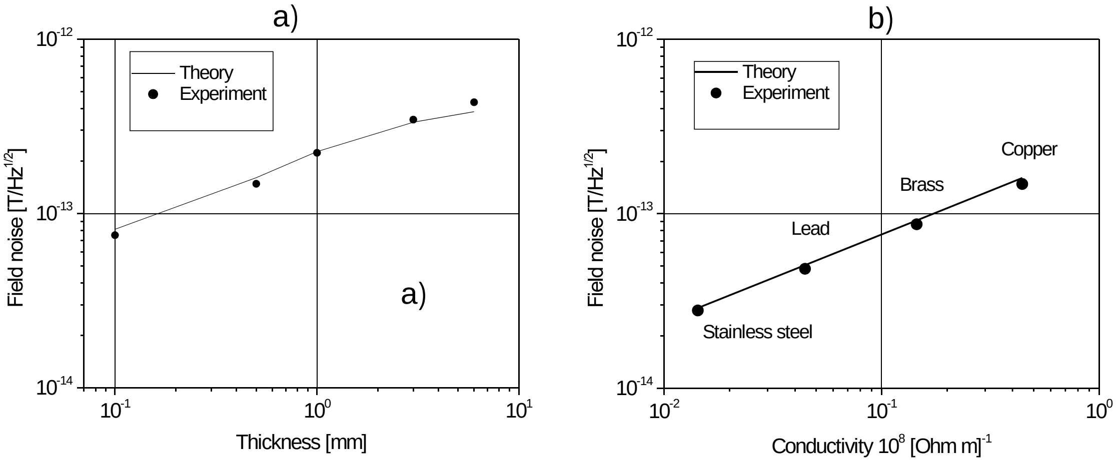

Figure 6.6. a) Thermal flux noise in copper disks as a function of the thickness of the disks. The diameter of the sensor coil was 30mm and the distance between disks and sensor coil was 10mm. b) Thermal flux noise due to disks of 83mm diameter and 0.5mm thickness as a function of conductivity. The diameter of the sensor coil was 30mm and the distance between disks and sensor coil was 10mm.

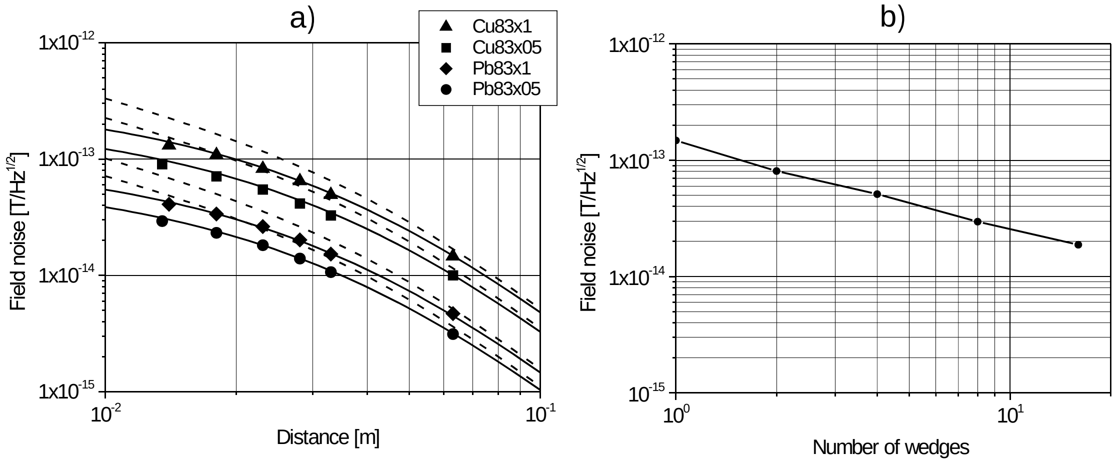

Figure 6.7. a) Thermal flux noise as a function of the distance between the disks and a sensor coil with a diameter of $50mm$. The intrinsic SQUID noise was subtracted from the measurements. The solid lines indicate the theoretical values given by (6.13). The dashed lines show the approximation $\left(\overline{B_z^2}\pi r_{sensor}^2\right)^{1/2}$. Pb 83x1 stands for two disks Pb 83x0.5 placed one on top of the other. b) Thermal flux noise as a function of the number of wedges in a circular disk at a distance of $10mm$ from a sensor coil with a diameter of $30mm$.

experimental data better than (6.16). This is especially true in practical cases where the distance between the sensor coil and the conducting disk is small and the diameter of the sensor coil is about the same as that of the conducting disk.

The flux noise level resulting from the two concentric parts cut from one disk was $95fT/\sqrt{Hz}$ and $117fT/\sqrt{Hz}$ for the disk-shaped part and the ring, respectively. When the two pieces were combined to one disk but keeping the two pieces insulated from each other, a noise level of $146fT/\sqrt{Hz}$ was recorded, whereas the noise level from the original disk was $151fT/\sqrt{Hz}$. So, the noise level from the two combined parts is equal to $\sqrt{95^2 + 117^2} \approx 151fT/\sqrt{Hz}$ being the same as that from the original disk. This is in accordance with expectation, because the secondary sources have a radial direction on the interface. The primary sources are the same for the combination of the two pieces and the original disk. This validates assumptions that were made in deriving (6.13). However, due to the presence of the tangential secondary sources at the interface, the flux noise of the disk cut in wedge-shaped pieces is decreased when the noise level from the combined pieces are compared with that from the original intact disk. The noise level decreases with the number of wedges as shown in figure 6.7b, as the number of interfaces increases.

6.5 Discussion

Theoretical values for the flux due to eddy currents were derived for low frequency and high frequencies. Empirically an expression was found for the entire frequency range. Measured and theoretical values are in agreement for different parameters, i.e., the conductivity, diameter and thickness of the disk, the separation between the disk and sensor coil, and the frequency of the applied magnetic field. Consequently, the conclusion that (6.7) describes the flux in the entire frequency range seems to be justified.

Also, the correspondence between theory and experiment for thermal noise is good. The correspondence is much better using (6.13) than using (6.16). Cutting the disk in wedge-shaped pieces helps to reduce the thermal noise. In this case, the volume currents contribute to the thermal flux noise as the secondary sources are in the tangential direction. The volume currents always counteract the magnetic field generated by the primary sources; hence, the thermal flux noise is reduced. Cutting the disk in a disk plus ring will not affect the thermal noise because the primary and secondary sources present in the original disk will not change.

References

Adelerhof D J, Nijstad H, Flokstra J, and Rogalla H, “(Double) relaxation oscillation SQUIDs with high flux-to-voltage transfer: Simulations and experiments”, *Journal of Applied Physics*, **76**(6), 3875–3886. 1994.

Anderson W A, “Electrical current shims for correcting magnetic fields”, *The Review of Scientific Instruments*, **32**(3), 241–250. 1961.

Bangert V, and Mansfield P, “Magnetic field gradient coils for NMR imaging”, *Journal of physics E: Scientific instruments*, **15**, 235–239. 1982.

Barbanera S, Carelli P, Leoni R, Romani G L, Bordoni F, Modena I, Fenici R, and Zeppili P, *Biomagnetism.* De Gruyter, Berlin, Chap. Biomagnetic measurements in unshielded normally noisy environments, pp. 139–149. 1981.

Bergveld P, Kolling A J, and Peuscher H J, “Real-Time Fetal ECG Recording”, *IEEE Transactions on Biomedical Engineering*, **BME-33**(5), 505–509. 1986.

Bork J, Hahlbohm H D, Klein R, and Schnabel A, “The 8-layered magnetically shielded room of the PTB: design and construction”, pp. 302–305 In: *BIOMAG 2000: Proceedings of the 12th International Conference on Biomagnetism.* 2000 (Aug. 13–17,).

ter Brake H J M, *SQUID magnetometers*, Ph.D. thesis, University of Twente, The Netherlands. 1986.

ter Brake H J M, Dunajski Z, van der Mheen W A G, and Flokstra J, “Electronic balancing of multichannel SQUID magnetometers”, *Journal of Physics E: Scientific Instruments*, **22**, 560–564. 1989.

ter Brake H J M, Wieringa H J, and Rogalla H, “Improvement of the performance of a mu - metal magnetically shielded room by means of active compensation”, *Measurement Science and Technology*, **2**, 596–601. 1991^a.

ter Brake H J M, Flokstra J, Houwman E P, Veldhuis D, Jaszczuk W, Stammis R, van Ancum G K, and Rogalla H, “On the SQUID-modules for the UT multichannel neuromagnetometer”, pp. 521–524 In: *SQUID 'Proc. 91 Superconducting Devices and Their Application.* 1991^b.

ter Brake H J M, Flokstra J, Jasszczuk W, Stammis R, van Ancum G K, Martinez A, and Rogalla H, “The UT 19-channel DC SQUID based neuromagnetometer”, *Clinical Physics and Physiological Measurement*, **12**, 45–50. 1991^c.

ter Brake H J M, Huonker R, and Rogalla H, “New results in active noise compensation for magnetically shielded rooms”, *Measurement Science and Technology*, **4**, 1370–1375. 1993.

ter Brake H J M, Rijpma A P, Stinstra J G, Borgmann J, Holland H J, Krooshoop H J G, Peters M J, Flokstra J, and Quartero H W P, “Fetal magnetocardiography: clinical relevance and feasibility”, *Physica C*, **368**, 10–17. 2002.

Brambati B, and Pardi G, “The intraventricular conduction, time of fetal heart in uncomplicated pregnancies”, *British Journal of Obstetrics and Gynaecology*, **87**, 941–948. 1980.

Broussov P P, Romans E J, Carr C, Donaldson G B, and Pegrum C M, “A high-Tc second-order gradiometer for use in an unshielded environment”, *IEEE Transactions on Applied Superconductivity*, **13**(2), 837–840. 2003.

Cantor R, *SQUID Sensors: Fundamentals, Fabrication and Applications.* NATO ASI Series E: Applied Sciences, vol. 329, Kluwer Academic Publishers, Chap. DC SQUIDS: Design, optimization and practical applications, pp. 179–233. 1996.

Cohen D, Schlpfer U, Ahlfors S, Hmlinen M, and Halgren E, “New Six-Layer Magnetically-Shielded Room for MEG”, pp. 919–921 In: *BIOMAG 2002: Proceedings of the 13th International Conference on Biomagnetism.* 2002 (Aug. 10–14,).

Ditterich J, and Eggert T, “Improving the homogeneity of the magnetic field in the magnetic search coil technique”, *IEEE Transactions On Biomedical Engineering*, **48**(10), 1178–1185. 2001.

Fisher B J, Dillon N, Carpenter T A, and Hall L D, “Design of a biplanar gradient coil using a genetic algorithm”, *Magnetic Resonance Imaging*, **15**(3), 369–376. 1997.

Flokstra J, Adelerhof D J, Houwman E P, Veldhuis D, and Rogalla H, “Josephson junctions and DC SQUIDS based on Nb/Al technology”, *Clinical Physics and Physiological Measurement*, **12**, 5966. 1991.

Hesterman V W, *Gradient wound trim coil for trimming a primary pickup coil.* US Patent 3965411. 1976^a.

Hesterman V W, *Superconducting magnetic sensor with improved balancing system.* US Patent 3976938. 1976^b.

Hosono T, Kawamata K, Chiba Y, Kandori A, and Tsukada K, “Prenatal diagnosis of long QT syndrome using magnetocardiography: a case report and review of the literature”, *Prenatal Diagnosis*, **22**(3), 198–200. 2002.

Jaworski F B, and Crum D B, *SQUID applications to geophysics: Workshop proceedings 2-4 June 1980 Soc. Explor. Geophysicists.* Scientific Laboratory Los Alamos, New Mexico, Chap. Sources of gradiometer imbalance and useful balancing techniques, pp. 19–24. 1980.

Kandori A, Miyashita T, Tsukada K, Horigome H, Asaka M, Shigemitsu S, Takahashi M I, Terada Y, and Mitsui T, “Sensitivity of foetal cardiograms versus gestation week”, *Medical and Biological Engineering and Computings*, 545–548. 1999.

Kandori A, Hosono T, Chiba Y, Shinto M, Miyashita S, Murakami M, Miyashita T, Ogata K, and Tsukada K, “Classifying cases of fetal wolff-parkinson-white syndrome by estimating the accessory pathway from fetal magnetocardiograms”, *Medical and Biological Engineering and Computings*, **41**(1), 33–39. 2003.

Kasai N, Sasaki K, Kiryu S, and Susuki Y, “Thermal magnetic noise of dewars for biomagnetic measurements”, *Cryogenics*, **33**, 175179. 1993.

Kato K, Yamazaki K, Sato T, Haga A, Ueda T, Kobayashi K, and Yoshizawa M, “Study on a new shielding method composed of magnetic shielding panels”, In: *BIOMAG 2002: Proceedings of the 13th International Conference on Biomagnetism.* 2002 (Aug. 10–14,).

Kato K, Yamazaki K, Sato T, Haga A, Okitsu T, Muramatsu K, Ueda T, Kobayashi K, and Yoshizawa M, “Active Magnetic Compensation Composed of Shielding Panels”, *Neurology and Clinical Neurophysiology*, **68**, 1–4. 2004.

Kochin N E, Kibel I A, and Roze N V, *Theoretical hydromechanics.* New York: John Wiley and Sons, inc. 1964.

van Leeuwen P, Lange S, Klein A, Geue D, Zhang Y, Krause H-J, and Gronemeyer D, “Reproducibility and reliability of fetal cardiac time intervals using magnetocardiography”, *Physiological Measurement*, **25**, 539–552. 2004.

Malmivuo J, and Plonsey R, *Bioelectromagnetism - Principles and Applications of Bioelectric and Biomagnetic Fields.* Oxford University Press. 1995.

Marieb E N, and Hoehn K, *Human Anatomy and Physiology.* Pearson Education. 2007.

Menendez T, Achenbach S, Beinder E, Hofbeck M, Klinghammer L, Singer H, Moshage W, and Daniel W G, “Usefulness of Magnetocardiography for the Investigation of Fetal Arrhythmias”, *The American Journal of Cardiology*, **88**, 334–336. 2001.

Merritt R, Purcell C, , and Stroink G, “Uniform magnetic field produced by three, four, and five square coils”, *Review of Scientific Instruments*, **11**, 903–920. 1993.

Morrone T, *Optimized gradient coils and shim coils for magnetic resonance scanning systems.* US Patent 5760582. 1998.

Oostendorp T F, and van Oosterom A, “Modelling the fetal magnetocardiogram”, *Clinical Physics and Physiological Measurement*, **12**, 15–18. 1991.

Oppenheim A V, and Schafer R W, *Digital signal processing.* NJ, Englewood Cliffs: Prentice Hall. 1975.

Overweg J A, and Walter-Peters M J, “The design of a system of adjustable superconducting plates for balancing a gradiometer”, *Cryogenics*, 529–534. 1978.

Peters M J, Stinstra J G, van den Broek S P, Huirne J A F, Quartero H W F, ter Brake H J M, and Rogalla H, “On the fetal magnetocardiogtam”, *Bioelectrochemistry and Bioenergetics*, **47**, 273–281. 1998.

Peters M J, Stinstra J G, Uzunbajakau S, and Srinivasan N, *Advances in electromagnetic fields in living systems.* Vol. 4, Springer US, Chap. Fetal Magnetocardiography, pp. 1–40. 2005.

Pissanetzky S, and Xiang Y, “Analytical expressions for the magnetic field of practical coils”, *Compel: The International Journal For Computation And Mathematics In Electrical and Electronic Engineering*, **9**(2), 117–121. 1990.

Plonsey R, and Heppner D B, “Considerations of quasistationarity in electrophysiological systems”, *Bulletin of Mathematical Biophysics*, **29**, 657–664. 1967.

Podt M, van Duuren M J, Hamster A W, Flokstra J, and Rogalla H, “Two-stage amplifier based on a double relaxation oscillation superconducting quantum interference device”, *Applied Physics Letters*, **75**(15), 2316–2318. 1999.

Primin M, Nedayvoda I, Vassylyev V, Sosnitskyy V, Steinberg F, Sutkovoy P, and Minov Y, “Algorithm of axial gradiometers additional balancing in the not uniform magnetic field”, pp. 952–954 In: *BIOMAG 2002: Proceedings of the 13th International Conference on Biomagnetism.* 2002 (Aug. 10–14,).

Rijpma A P, *Fetal heart monitor: development of a cryocooler-cooled high-Tc SQUID system for fetal magnetocardiography in unshielded environment*, Ph.D. thesis, University of Twente, The Netherlands. 2002.

Rijpma A P, Krooshoop H J G, Lefevere M W, van Leeuwen E P, Holland H J, ten Haken B, and ter Brake H J M, “Construction and test of a cryocooler-cooled low-Tc SQUID gradiometer system”, *Cryogenics*, **48**, 61–67. 2008.

Robinson S E, Burbank M B, Fife A A, Haid G, Kubik P R, Seachev I, Taylor B, Tillitoson, Vrba J, Wong G, Lowery C L, Eswaran H, Wilson J D, Murphy P, and Preissl H A, “A Biomagnetic Instrument for Human Reproductive Assessment”, pp. 919–922 In: Nenonen J (ed), *Biomag 2000, 12th International Conference on Biomagnetism.* 2001.

Rorden L H, *Trimmed superconductive magnetic pickup coil circuits.* US Patent 3956690. 1976.

Rubens S M, “Cube-surface coil for producing a uniform magnetic field”, *The Review of Scientific Instruments*, **16**(9), 243–245. 1945.

Sarvas J., “Basic mathematical and electromagnetic concepts of the biomagnetic inverse problem”, *Physics in Medicine and Biology*, **32**, 1122. 1987.

Stinstra J G, *The reliability of the fetal magnetocardiogram*, Ph.D. thesis, University of Twente, The Netherlands. 2001.

Turner R, “A target field approach to optimal coil design”, *Journal of physics D: Applied Physics*, **19**, L147–L151. 1986.

Turner R, “Gradient coil design: a review of methods”, *Magnetic Resonance Imaging*, **11**, 903–920. 1993.

Uzunbajakau S, Rijpma A P, Dolfsma J, Krooshoop H J G, ter Brake H J M, Peters M J, and Rogalla H, “Magnetic Flux Fluctuations Due to Eddy Currents and Thermal Noise in Metallic Disks”, *IEEE transactions on magnetics*, **39**(4), 2018–2023. 2003.

Uzunbajakau S, Rijpma A P, ter Brake H J M, and Peters M J, “On Gradiometer Imbalance”, *IEEE transactions on applied superconductivity*, **16**(3), 1898–1907. 2006.

Varpula T, and Poutanen T, “Magnetic field fluctuations arising from thermal motion of electric charge in conductors”, *Journal of Applied Physics*, **55**, 4015–4021. 1984.

Vrba J, *SQUID Sensors: Fundamentals, Fabrication and Applications.* NATO ASI Series E: Applied Sciences, vol. 329, Kluwer Academic Publishers, Chap. SQUID gradiometers in real environments, pp. 117–178. 1996.

Vrba J, *Method and systems for obtaning higher order gradiometer measurements with lower order gradiometers.* US Patent 5657756. 1997.

Vrba J, Fife A A, Burbank M B, Weinberg H, and Brickett P A, “Spatial discrimination in SQUID gradiometers and 3rd order gradiometer performance”, *Canadian Journal of Physics*, **60**, 1060–1073. 1982.

Vrba J, and McCubbin J, “First-Gradient Balancing of higher-order gradiometers”, *IL Nuovo Cimento D*, **2**, 142–152. 1983.

Vrba J, and Mckay J, “Character and acquisition of multichannel biomagnetic data”, *Applied Superconductivity*, **5**, 431–439. 1998.

Vrba J, and Robinson S E, “SQUID sensor array configurations for magnetoencephalography applications”, *Superconductor Science and Technology*, **15**, R51–R89. 2002.

Wltgens P J M, and Koch R H, “Magnetic background noise cancellation in real-world environments”, *Review of scientific instruments*, **71**(3), 1529–1533. 2000.

Zeng X H, Soltner H, Selbig D, Bode M, Bick M, Rders F, Schubert J, Zander W, Banzet M, Zhang Y, Bousack H, and Braginski A I, “A high-temperature rf SQUID system for magnetocardiography”, *Measurement Science and Technology*, **9**, 1600–1608. 1998.

Glossary of Abbreviations

Abbreviation	**description**
ECG	electrocardiogram
MCG	magnetocardiogram
fECG	fetal electrocardiogram
fMCG	fetal magnetocardiogram
fECG	fetal encefalogram
PJRT	persistent junctional reciprocating tachycardia
FHARMON	foetale hart monitor (Dutch)
SNR	signal-to-noise ratio
RFI	radio frequency interference
PCB	printed circuit board
SQUID	superconducting quantum interference device
FLL	flux locked loop
FEM	finite element method
ISR	interference signal ratio
DAQ	data acquisition card
DROS	double relaxation oscillation SQUID

Summary

Activation of the cardiac muscle is associated with the ion transport through the membrane of the cardiac cell. This ion transport gives rise to the strongest electrophysiological signals in human body: the cardiograms. Segments of the cardiogram are related to the contraction of the hearts chambers. Information useful for an accurate medical diagnosis can be obtained by examining the cardiogram.

In fetal magnetocardiography, the magnetic field of a fetal heart is recorded in the vicinity of the maternal abdomen. The magnetic field produced by the fetal heart, however, is extremely weak and can only be recorded by means of *S*uperconducting *QU*antum *I*nterference *D*evices (SQUIDs). To reach the superconducting state the SQUIDs are cooled to cryogenic temperatures (about -270^oC). Typically, the fetal magnetocardiograms are recorded inside magnetically shielded rooms in order to reduce the influence of the environmental magnetic interference.

Currently, fetal magnetocardiograms are recorded in a few research centers in the world equipped with shielded rooms. The necessity of the magnetically shielded room and the necessity of the constant supply of liquid helium for cooling hinder the daily use of fetal magnetocardiography in hospitals. The FHARMON (stands in Dutch for Foetale HARt MONitor) project aims at the realization of a cryocooler-cooled low critical temperature fetal magnetocardiograph that can be operated outside the magnetically shielded room. The objective of the work presented in this thesis is to design a highly balanced gradiometer for the FHARMON system that enables measurements of fetal magnetocardiograms in unshielded environment.

The FHARMON system utilizes a highly balanced third-order gradiometer as an alterative to the magnetically shielded room. This gradiometer has a number of geometrical parameters that can be optimized for the maximal signal-to-noise ratio of the recorded fetal magnetocardiograms. The gradiometer optimization is described **Chapter 2**.

Ideally, a third-order gradiometer is insensitive to the lower-order gradients of the magnetic field. In practice, however, it is difficult to manufacture a gradiometer such that its sensitivity to these lower-order gradients is eliminated completely. The residual sensitivity of a gradiometer to the lower order gradients is referred to as imbalance. Imbalance reduces the ability of a gradiometer to suppress the environmental interference. In **Chapter 3** a method for evaluating the imbalance of an arbitrary gradiometer by means of simulations is proposed. This method is applied to the imbalance evaluation of the gradiometer of the FHARMON system.

Imbalance of the gradiometer of the FHARMON system needs to be reduced in order to achieve the necessary level of suppression of the environmental magnetic interference. This is done by means of electronic balancing. A system of reference sensors that are sensitive to the lower-order gradients of the magnetic field are introduced into the gradiometer. During the balancing, the gradiometer with the system of references is placed inside a characterization coil set. This characterization coil set produces high-uniformity magnetic fields that correspond to the lower-order gradients of the magnetic field. The signals of the reference channels are mixed with the signal of the third-order gradiometer such that the resultant signal equals zero for all applied test magnetic fields. The design of the characterization coil set is described in **Chapter 4**. The mechanical construction of the coil set as well as the gradiometer balancing experiments are presented in **Chapter 5**.

The gradiometer is enclosed by a conducting radio frequency interference shield as well as by metallic sheets for thermal isolation. The thermal magnetic noise and the eddy current effect caused by these shields decrease the sensitivity of the system. Equations that allow quantitative evaluation of these effects are available in literature. **Chapter 6** describes experiments that confirm these equations.

Samenvatting

Activiteit van cellen in het hart gaat gepaard met ionentransport door de wand van de cellen. Deze ionenverplaatsing veroorzaakt het sterkste elektrophysiologisch signaal in het menselijk lichaam: het cardiogram. De verschillende segmenten van het cardiogram zijn gerelateerd aan de samentrekking van de verschillende delen van het hart. Uit een cardiogram is zeer bruikbare informatie te halen ten behoeve van een medische diagnose.

In foetale magnetocardiografie wordt het magnetisch veld van het foetale hart gemeten vlak boven de moederbuik. Het magnetisch veld geproduceerd door het foetale hart is echter extreem zwak en kan alleen gemeten worden met supergeleidende magnetometers, zogenaamde SQUIDs (Superconducting QUantum Interference Devices). Om in de supergeleidende toestand te geraken moeten deze magnetometers afgekoeld worden tot cryogene temperaturen (ca. -270^oC). Om bovendien de invloed van storende velden uit de omgeving tegen te gaan, worden foetale magnetocardiogrammen gewoonlijk gemeten in magnetisch afgeschermde kamers.

Tegenwoordig worden foetale magnetocardiogrammen gemeten in slechts een paar onderzoekscentra in de wereld, alle uitgerust met een magnetisch afgeschermde kamer. De noodzaak van zon afgeschermde kamer en de noodzaak om geregeld vloeibaar helium te vullen voor de koeling, verhinderen het dagelijks gebruik van foetale magnetocardiografie in ziekenhuizen. Het Foetale HArt MONitor (FHARMON) project is gericht op de realisatie van een koelmachine-gekoelde lage-temperatuur foetale magnetocardiograaf die kan worden gebruikt buiten de magnetisch afgeschermde kamer. Het doel van het onderzoek dat in dit proefschrift is beschreven, is het ontwerp van een zeer goed gebalanceerde gradiometer voor het FHARMON systeem, die metingen van foetale magnetocardiogrammen mogelijk maakt in een onafgeschermde omgeving.

Het FHARMON systeem maakt gebruik van een zeer goed gebalanceerde derde-orde gradiometer als alternatief voor de magnetisch afgeschermde kamer. Deze gradiometer heeft een aantal geometrische parameters die geoptimaliseerd kunnen worden met betrekking tot de gerealiseerde signaal-ruis-verhoudeng van de foetale magnetocardiogrammen. De gradiometeroptimalisatie is beschreven in **Hoofdstuk 2**.

Idealiter is een derde-orde gradiometer ongevoeling voor lagere-orde gradinten van het magnetisch veld. In de praktijk is het echter heel moeilijk om een gradiometer zo nauwkeurig te maken dat de gevoeligheid voor deze lagere-orde gradinten compleet verdwijnt. De resterende gevoeligheid van een gradiometer voor lagere-orde gradinten wordt onbalans genoemd. Onbalans beperkt het vermogen van een gradiometer om de storing uit de omgeving te onderdrukken. In **Hoofdstuk 3** van dit proefschrift is een methode voorgesteld om de onbalans van een willekeurige gradiometer te evalueren met behulp van simulaties. Deze methode is toegepast op de onbalans van de gradiometer voor het FHARMON systeem.

De onbalans van de FHARMON-gradiometer moet verbeterd worden om de vereiste onderdrukking van omgevingsstoring te kunnen realiseren. Dit wordt gedaan door elektronische balancering. Een systeem van referentiesensoren die gevoelig zijn voor de lagere-orde gradinten van het magnetisch veld worden geplaatst in de gradiometer. Gedurende de balancering bevindt de gradiometer zich met de referentiesensoren in een speciale karakterisatiespoelenset. Deze spoelenset genereert magnetische velden die corresponderen met de lagere-orde gradinten, en wel met zeer hoge uniformiteit. De signalen van de referenties worden gemengd met het signaal van de gradiometer op zon manier dat het resulterende uitgangssignaal nul is voor alle aangelegde veldconfiguraties. Het ontwerp van de karakterisatiespoelenset is beschreven in **Hoofdstuk 4**. De mechanische constructie van de spoelenset en de experimenten met betrekking tot de gradiometerbalans zijn beschouwd in **Hoofdstuk 5**.

Om radiofrequente storing af te schermen is een elektrisch geleidend scherm om de gradiometer geplaatst. Ook worden metaalfolies gebruikt rond de gradiometer om de warmtebelasting door straling te verminderen. De thermische magnetische storing en de wervelstroomeffecten ten gevolge van deze metaallagen beperken de resolutie van het systeem. Uitdrukkingen voor deze effecten zijn beschikbaar in de literatuur. **Hoofdstuk 6** beschrijft experimetne die deze uitdrukkingen bevestigen.

Acknowledgements

I would like to express my deepest gratitude to all colleagues from the Low Temperature Division of the University of Twente who supported my research during all these years.

First of all, I would like to thank Prof. dr. ir. Marcel ter Brake for supervising my Ph.D. research, reviewing the papers and the thesis, and for translating the summary of the thesis into Dutch. Your insightful remarks and suggestions helped me in my daily work. I will never forget our discussions related to my thesis in a cosy cafe in the city center of Eindhoven.

The results described in this thesis would not be possible without help of my daily supervisor Dr. ir. Albert Rijpma. Bert, I think your remarkable ability to solve complex technical problems always helped us to move forward in our research. I was especially glad to cooperate with you as a co-author as no mistake or a weak spot in an article can escape your attention.

All the ideas would never be implemented without technical support of Ir. Erik Krooshoop. Erik, I would like to thank you for implementing all these intricate mechanisms, constructions, and electronic devices we used in the laboratory. Your experience and practical technical knowledge will always be a good example for me.

I am also indebted to Dr. ir. Bennie ten Haken for his help and critical remarks. Bennie, I very mush appreciate the comments you made reviewing the articles and the thesis.

Finally, I would like to thank all members of Applied Physics Department and especially Prof. M.J. Peters for creating a friendly cosy atmosphere ever stimulating for great scientific achievements.

Publications

Papers

S. Uzunbajakau, A.P. Rijpma, J. Dolfsma, H.J.G. Krooshoop, H.J.M ter Brake, M.J. Peters, and H.Rogalla "Magnetic flux fluctuations due to eddy currents and thermal noise in metallic disks", *IEEE Transactions on Magnetics* ISSN 0018-9464, 2003, 39(4), pp.2018-2023.

S. Uzunbajakau, A.P. Rijpma, H.J.M ter Brake, M.J. Peters "Optimization of a third-order gradiometer for operation in unshielded environments", *Transactions on Applied Superconductivity* ISSN 1051-8223, 2005, 15(3), pp.3879-3885.

S. Uzunbajakau, A.P. Rijpma, H.J.M ter Brake, M.J. Peters "On gradiometer imbalance", *Transactions on Applied Superconductivity* ISSN 1051-8223, 2006, 16(3), pp.1898-1907.

S. Uzunbajakau, H.J.G. Krooshoop , A.P. Rijpma, B. ten Haken, H.J.M ter Brake, M.J. Peters "Magnetic field coils for gradiometer balancing", *Transactions on Applied Superconductivity* ISSN 1051-8223, 2007, 17(1), pp.52-59.

Conference proceedings

S. Uzunbajakau, H.J.G. Krooshoop, M.J. Peters "A sensitive magnetocardiograph for fetal surveillance", *Engineering in Medicine and Biology Society, 2001. Proceedings of the 23rd Annual International Conference of the IEEE*, 2001, Vol. 1, pp.378-380.

S. Uzunbajakau, H.J.G. Krooshoop, M.J. Peters "Magnetic flux fluctuations due to eddy currents and thermal noise in metallic disks", *Proceedings of the Dutch Annual Conference on Biomedical Engineering*, ISBN 903651807-5, 2002, pp.130-132.

S. Uzunbajakau, A.P. Rijpma, H.J.G. Krooshoop, H.J.M ter Brake, M.J. Peters "A magnetic field generator for gradiometer calibration", *Proceedings of the Dutch Annual Conference on Biomedical Engineering* ISBN 90-365-1973-X, 2003, pp.180-182.

S. Uzunbajakau, A.P. Rijpma, H.J.G. Krooshoop, H.J.M ter Brake, M.J. Peters "Calibration of the measuring head for the FHARMON project", *Proceedings of the Dutch Annual Conference on Biomedical Engineering* ISBN90-365-2102-5, 2004, pp.174-175.